

ISBN: 978-94-6108-946-5

SnS nanoparticles to boost CuInS₂ solar cells

(met een samenvatting in het Nederlands)

Proefschrift

ter verkrijging van de graad van doctor aan de Universiteit Utrecht
op gezag van de rector magnificus, prof. dr. G. J. van der Zwaan,
ingevolge het besluit van het college voor promoties
in het openbaar te verdedigen op
maandag 30 maart 2015 des middags te 12.45 uur

door

Caterina Prastani

geboren op 10 maart 1982 te Catania, Italië

Promotor: Prof. dr. R. E. I. Schropp
Co-promotor: Dr. J. K. Rath

The work described in this thesis is carried out with subsidy from the Netherlands Agency for Energy and the Environment (Agentschap NL) of the Ministry of Economic Affairs of The Netherlands: program EOS (Energie Onderzoek Subsidie).

Contents

1	Introduction	9
1.1	Renewable energy	10
1.2	Photovoltaic energy	11
1.3	CI(G)S solar cells	13
1.4	Concepts to enhance solar cell efficiency	16
1.4.1	Multi-junction solar cells	16
1.4.2	Up/down conversion	16
1.4.3	Hot Carrier Solar Cells	17
1.4.4	Multiple Exciton Generation (MEG)	17
1.4.5	Intermediate Band Solar Cells (IBSC)	17
1.5	Intermediate Band Solar Cells	17
1.5.1	What is a Quantum Dot?	19
1.5.2	Quantum Dots IB Solar Cells	19
1.6	Outline of this thesis	21
2	Experimental techniques	23
2.1	Deposition techniques	24
2.1.1	Spray Pyrolysis	24
2.1.2	Chemical Bath Deposition	24
2.2	Material Characterization	25
2.2.1	TEM-HRTEM	25
2.2.2	SAED-EDX	26
2.2.3	Optical absorption	27
2.2.3.1	Dual-beam UV-VIS spectroscopy	27
2.2.3.2	R/T measurements	27
2.2.3.3	Photothermal Deflection Spectroscopy	28
2.2.4	XRD	29
2.2.5	Conductivity and activation energy	30
2.2.6	Scanning Tunneling Spectroscopy	30
2.2.7	Atomic Force Microscopy	31

2.2.8	ESR	32
2.3	Devices Characterization	33
2.3.1	Solar simulator	33
2.3.2	Quantum efficiency	35
3	Synthesis and Characterization of SnS nanoparticles	37
3.1	Introduction	38
3.2	Synthesis	40
3.3	Final synthesis and characterization	41
3.4	Doping in Quantum Dots	44
3.5	Thin Film of Quantum Dot	49
3.6	Conclusion	52
4	Synthesis and characterization of SnS/In₂S₃ core-shell nanoparticles	55
4.1	Introduction	56
4.2	Synthesis and characterization	57
4.3	SnS/In ₂ S ₃ core-shell NPs thin film	59
4.4	SnS QDs embedded in In ₂ S ₃ thin film	64
4.5	Conclusion	69
5	Electrical characterization of nanoparticles by means of Atomic Force Microscope	71
5.1	A brief introduction to AFM	72
5.2	AFM operation mode	73
5.3	AFM of Semiconductor Quantum Dots	76
5.3.1	TR-TUNA AFM	76
5.3.1.1	Working principles	76
5.3.1.2	Results	77
5.3.2	Peak Force AFM	81
5.3.2.1	Working principles	81
5.3.2.2	Results	81
5.4	Conclusion	85
6	CIS solar cell embedded nanoparticles	87
6.1	Introduction	88
6.2	Alternative buffer layers	90
6.3	New configuration of CIS solar cells	90
6.3.1	The effect of copper gradient	94
6.3.2	SnS QDs embedded in CIS solar cells	96
6.3.3	Light and temperature dependencies	97

6.3.4 SnS/In ₂ S ₃ core-shell nanoparticles embedded in CIS solar cells	102
6.4 SnS QDs embedded into CIGS solar cells	104
6.5 Conclusion	110
Bibliography	113
Summary	129
Samenvatting	133
List of publications	139
Acknowledgements	141
Curriculum Vitae	143

Chapter 1

Introduction

In the last years renewable energies have gained a lot of interest because of fossil fuel prices and the environmental problems due to these conventional fuels. In this chapter we give a short overview on renewable energy with a special focus on the photovoltaic energy, analyzing the advantages and the bottlenecks of this energy source. Among the different types of solar cells, CI(G)S solar cells will be discussed in depth in section 1.3.

One of the aims of the study is to decrease the price of solar cells while continuing to increase efficiency. Many ideas have already been developed to achieve this goal, and in this chapter we will present the most successful ones. One section will be dedicated entirely to the concept of Intermediate Band Solar Cells, a new idea which will allow us to enhance the efficiency in absorbing the photons with less energy than the band gap. For this type of solar cell quantum dots play an important role. For this reason, a short introduction about quantum dots is given.

The outlines summarizes the results of this thesis.

1.1 Renewable energy

Global energy demand is constantly increasing. Population and income growth are the key drivers for this. It is expected that the world population will reach 8.3 billion by 2030 and the world income will double as compared with 2011. World energy consumption increases by 1.6 % per annum, adding 36% to total consumption in 2030 [1]. This is due to the rapid industrialization, urbanization and motorization of emerging countries such as China, India, Brazil and countries in the Middle East. So far, fossil fuels—mainly coal, oil and natural gas—are the dominant energy consumption with obvious consequences for carbon emissions [2]. There are three main reasons why fossil fuels dominate the market. First of all, fossil fuels are traditional energy sources and their use involves a strong political interest. The second reason is their low price, because emerging countries need cheap energy to strengthen their economy. The third and the most problematic issue is the much-needed improvement in the technology for renewable energies that can compete and replace traditional energy sources. Nevertheless, it is urgently necessary to solve these problems because the fossil fuel sources are not unlimited and moreover, they cause climate change [3]. According to the World Energy Outlook projections of energy trends through to 2035, the International Energy Agency (IEA) estimates that the long-term average global temperature will rise more than 5.3°C with the current energy policies, much more than the accepted 2°C [4]. In the last few years government policies have been focused on the development of new alternative energies to be able to overcome these problems. Renewable energies are the best possible solution: they are clean, they have no or lower emission of carbon dioxide and local pollutants, and they are a sustainable and inexhaustible source. Many countries are investing in renewable energies, and the United Nations wishes to double the share of renewable energy by 2030 [4].

Among the different types of renewable energies solar energy is the most promising candidate. Solar energy generation is normally divided into two types of technologies: solar thermal and photovoltaic. In solar thermal applications solar radiation is converted into heat, mainly for domestic uses, such as heating swimming pools, heating water and space heating of buildings. However, there are also large commercial solar thermal plants in operation. Photovoltaic technology, in contrast, converts the solar radiation directly into electrical current.

It is true that the solar energy reaching earth is enough to satisfy the annual world energy needs. However there are still many challenges to make photovoltaics the major energy supply. The causes are the cost, conversion efficiency and storage [5]. Researchers are dealing with it to try to find a solution to go beyond the present state. The research is focused on developing new cheap deposition techniques to decrease the price and, at the same time, investigate

new concepts of solar cells to increase efficiency. However, there is another important bottleneck: it is still not possible to store the generated current efficiently. The energy must be stored and dispatched on demand to the users. This is a hot topic for researchers, and different proposals have been made to address this issue. One possible solution could be storing the energy in form of chemical bonds in a fuel cell [6].

1.2 Photovoltaic energy

The photovoltaic effect was discovered by Alexandre-Edmond Becquerel in 1839 [7]. He realized that by illuminating a platinum electrode, immersed in acid solution, with different types of light, current was generated. Another important step forward to the development of solar cells was made by Fritts in 1883. He made the first thin film device placing molten selenium on a metal substrate and pressing a gold leaf to the exposed surface, creating a thin film of selenium. That device had an area of 30 cm^2 [8]. He was the first to understand the enormous potential of this device. Indeed, replacing gold with cheaper materials it was possible to manufacture this type of devices at a low cost, he realized that the current could be stored or transmitted [9]. However, the theoretical knowledge was not sufficient at that time to completely understand the behavior of these devices. Further development had to wait for the “quantum mechanics revolution”; the new concepts of photons, electrons and holes helped to describe and investigate the physical phenomenon. For this reason, it wasn’t until 1954 that the first ‘modern’ solar cell was made at Bell Laboratories. It was a simple silicon pn junction which reached 6% efficiency [10]. Since then, solar cells have gained a great deal of interest. Year after year many types of solar cells have been produced using different materials, and technologies, achieving higher efficiencies. The fundamental physical principles of solar cells have been investigated studying the relation between band gap, incident light spectrum, temperature, thermodynamics and efficiency. One important contribution was given by Shockley and Queisser in 1960 [11]. They demonstrated that, for a single junction solar cell, the efficiency never crosses the limit of 30% in terms of efficiency for a band gap of 1.1 eV (i.e. c-Si). For a more clear understanding it is better to mention how the current is generated in a solar cell. The light is an electromagnetic wave composed of elementary particles called photons. When one photon hits a semiconductor, it can be absorbed by the material. The absorbed photon gives its energy to an electron, which can jump from the valence band (VB) to the conduction band (CB), creating an electron-hole pair. The difference between the valence and the conduction bands is called *band gap* (E_g). Hence, the efficiency of a solar cell largely depends on the size

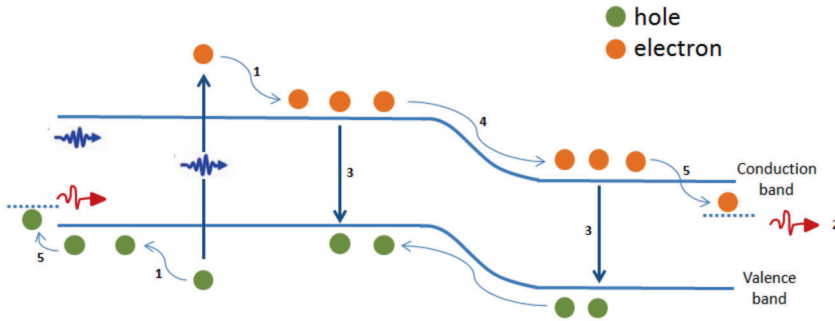


Figure 1.1: Losses in single junction solar cells. With (1) and (2) the thermalization and transmission losses are represented. The others are: contact losses (3), recombination losses (4) and junction losses (5).

of the band gap of the semiconductor used. It has been calculated that the maximum achievable value of efficiency is 34% corresponding to an optimum band gap of 1.4 eV [11].

Around 70% of the total energy loss is due to the spectral mismatch and can be divided into two categories: the optical “*transmission losses*” due to the impossibility to absorb photons with energy less than the band gap, and the “*thermalization losses*” where photons with energy higher than the band gap are absorbed to create “hot” electron-hole pairs [12] which relax to the conduction and valence band edge in a thermalization process, losing the excess energy in the form of heat. Other loss mechanisms are the radiative recombination, contact loss and pn junction loss leading to voltage losses. All these mechanisms are schematically depicted in Fig. 1.1. However, it is important to stress that the maximum efficiency can never reach the value of 1 because of the thermodynamic limit. The limiting efficiency, or Carnot efficiency, is about 95% and is due to the difference between the temperature of the source and the sink.

The main target to make photovoltaic a competitive energy source is to reduce the module price and obtain higher energy conversion efficiency. Solar cells can be categorized into three different “generations”, as shown in Fig. 1.2. First (I) and second (II) generation solar cells are subject to the Shockley-Queisser efficiency limit. Belonging to generation I crystalline silicon (c-Si) based single junction solar cells are based on silicon wafers with a typical thickness of few hundred nanometers. They suffer from by high production cost and limited efficiency. The record efficiency for a single junction c-Si solar cell is held by the UNSW lab with an efficiency of 25% [13], which is already very near to S-Q limit for the band gap 1.1 eV.

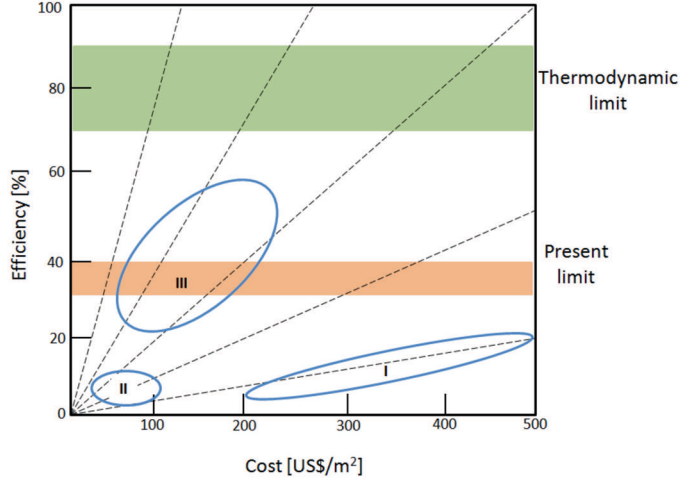


Figure 1.2: Solar cells efficiency versus cost for first, second- and third generation solar cells. The thermodynamic and Shockley-Queisser limits are reported.

The generation II of solar cells was developed with the aim to decrease the price using less material. These solar cells are based on thin film technology where a thin film is used as an absorber layer instead of bulk material. The thin film technology still remains very popular due to its many advantages, though c-Si (I gen. cells) has more than 80% of the PV market share [14]. It is possible to use large glass substrates because the deposition is from gas phase, which allows also low temperature processing. Furthermore, substrates other than glass, as plastics and metal foil flexible substrates suitable for the roll-roll process, can be used.

The most commonly used semiconductor thin films for the second generation are these three: Thin Film Silicon (TF-Si) [15–18], CdTe [19, 20] and Copper Indium (Gallium) Selenide/Sulfide (CIS/CIGS).

The work of this thesis is centered on CIS and CI(G)S solar cells and the next section will give an overview on the benefits and issues of this type of solar cell.

1.3 CI(G)S solar cells

CIS is an alloy composed of copper, indium and selenium or sulfur with a chalcopyrite structure, as shown in Fig. 1.3. In this thesis, to avoid any confusion, CIS will be used for copper Indium disulfide, whereas copper Indium diselenide will be referred to as CISE.

The research on CISE and CIS solar cells started at Bell Laboratories in

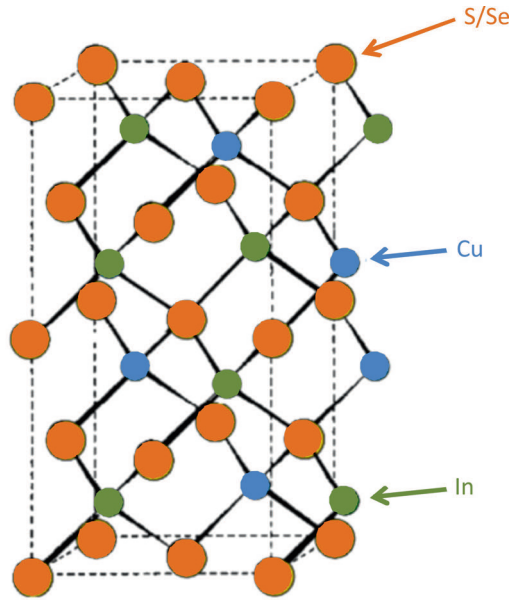


Figure 1.3: Crystal structure of CIS alloy.

the early 1970s where a wide selection of ternary chalcopyrite crystals were grown and characterized [21]. Copper indium diselenide (CISe) is a p-type ternary semiconductor with a direct band gap of 1 eV, whereas CIS has a band gap of 1.53 eV, and a high absorption coefficient ($3.6 \times 10^{-5} \text{ cm}^{-1}$), the highest reported in literature. Because of its high absorption coefficient, CIS is a suitable material for photovoltaic applications. However, they contain native defects of copper vacancies and copper on indium anti-site defects which are acceptor defects. Other possible native defects are indium on copper anti-site defects and selenium vacancies which are donor defects. In 1974 Shay et al. developed the first working CISe solar cell [22] depositing a CdS n-type layer on a single crystal of CuInSe_2 , and one year later they gained 12% in efficiency [23].

It is possible to make CISe more conductive (heavily p-type) incorporating more copper than indium, but this can degrade the quality of the devices. This happens because copper selenide is highly conductive, and this can cause a short circuit. On the other hand, adding more indium than copper causes more copper vacancies and, thus, indium on copper antisite defects are created. Hence, to get a good quality material the ratio between copper and indium has to be close to 1:1. However, because of the low formation energy of copper vacancies the material is p-type.

One of the disadvantages of the CISe solar cells is the low open circuit voltage. This is due to the low band gap. Nevertheless, it is possible to overcome

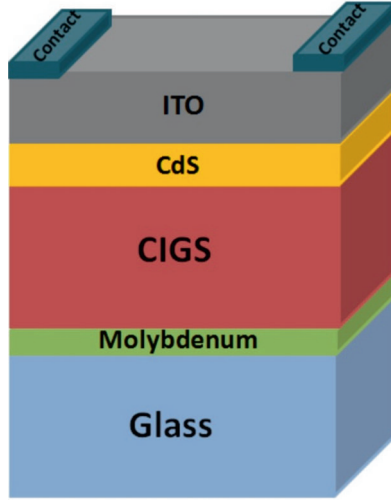


Figure 1.4: CIGS solar cell configuration.

this issue by adding gallium in the ternary alloy, forming CIGS alloy. The Ga atoms substitute some amount of indium. This incorporation allows the band gap to increase from 1.02 eV to 1.7 eV. The band gap value for $\text{CuIn}_{(1-x)}\text{Ga}_x\text{Se}_2$ changes according to the percentage of Gallium with the following formula [24]:

$$E_g = 1.011 + 0.664x - 0.249x(1 - x) \quad (1.1)$$

The typical structure of a CIGS solar cell is shown in Fig. 1.4. Soda-lime glass is used as substrate and molybdenum is sputter deposited on it as back contact. Afterwards, CIGS absorber layer is grown. Several methods are available to deposit the CIGS layer. A thin n-type CdS layer is deposited on top of the absorber layer, acting as the emitter partner to the p-type CIGS film. After that, a layer of aluminum-doped ZnO (ZnO:Al) is deposited; it is a transparent conductive oxide and it allows the collection of the carriers. Often ZnO:Al is deposited by sputtering, but this method can damage the cell. For this reason an intrinsic ZnO layer is deposited as a buffer between CdS and ZnO:Al to protect the absorber layer, preventing any damage.

The record of efficiency for CIGS solar cell is 21.7%, obtained by ZSW for a 0.5 cm^2 sized cell. A similar high efficiency of 20.4% was achieved by EMPA even on flexible substrate [25]. To improve further the efficiency, the next step is to find new concepts of solar cells to break the S-Q limit. This is the aim of the third generation of solar cells.

1.4 Concepts to enhance solar cell efficiency

As mentioned in section 1.2, Shockley-Queisser limit is valid for a single junction solar cell. One of the ways to go beyond this limit is by minimizing the spectral mismatch losses, a possible solution for which is a multiple threshold approach which allows shifting the limit to 67% or 86.8%, depending on the sun concentration, unconcentrated light or highest concentration respectively [26]. Different approaches have been proposed and devices made by some of them are already commercially available [27].

1.4.1 Multi-junction solar cells

The principal idea of this concept is absorbing photons with different energies by using multiple energy levels. The configuration of this type of solar cells is the simplest among the 3rd generation concepts: it consists of multiple pn or p-i-n junctions made by different absorber materials, with increasing band gaps, placed on top of each other. The wider band gap solar cell, absorbing and collecting the higher energy photons, gives higher voltage, thus the thermalization losses decrease. The particle balance efficiency limit for an infinite number of sub-cells is 68.2% [26]. However, a calculation using detailed balance theory, considering an infinite amount of sub-cells, predicts that the efficiency can reach 86% [28]. Among these type of solar cells, tandem and triple junctions are the most used. They can theoretically reach an efficiency of 42.5% and 48.6% respectively under unconcentrated and concentrated light. Experimentally efficiency above 40% under concentrated light for a triple junction is already reached. [29]. Tandem and triple junction solar cells using III-V compounds are quite expensive and for this reason they are used mostly for space applications because the efficiency is more important than cost. The research is focused on finding a solution to the high costs.

1.4.2 Up/down conversion

A limit for the efficiency is due to the polychromatic nature of the solar spectrum. Up and down conversions are two possible approaches to overcome this limit. Up conversion is a process by which two photons with energy lower than the band gap are converted in one photon, with energy higher than the band gap, that can be absorbed [30]. The down conversion is the reverse process; a single photon with energy much higher than the band gap is converted into two infrared photons which can still be absorbed [31]. Both of these processes can break the S-Q limit and it is possible to achieve an efficiency of 50% for up conversion and 40% for down conversion [32].

1.4.3 Hot Carrier Solar Cells

The hot carrier solar cell concept is a new approach to reduce the thermalization losses. In this type of cell, the carriers are kept in a thermal disequilibrium with the lattice due to a reduction of electron-phonon interaction [33]. In these cells, selective energy contacts are used because they only allow carriers with a specific energy to be collected. With this approach the cell can reach high voltages. This concept of solar cell is interesting because it allows efficiencies to be reached closer to the thermodynamic limit, around 65% for unconcentrated illumination [34].

1.4.4 Multiple Exciton Generation (MEG)

Another possibility for preventing thermalization losses is producing an enhanced photocurrent. Multiple Exciton Generation is a phenomenon which takes place in quantum dots where hot carriers produce two or more electron-hole pairs before relaxation. Theoretically, MEG could also take place in bulk semiconductors but it is difficult to observe it. Many studies have reported observation of MEG in quantum dots [35–38], but implementing MEG in solar cells is still an ongoing challenge [39]. It has been calculated that it is possible to achieve an efficiency of more than 40% [40].

1.4.5 Intermediate Band Solar Cells (IBSC)

The idea of enhancing solar cells using an intermediate band within the band gap of the absorber material of a cell was carried out by Antonio Luque and Antonio Martí [41], refining an idea from Wolf [42]. They proposed a new solar cell concept by which it will be able to capture and use photons with energy less than the band gap. Introducing a material within the cell, a new intermediate band is created between the conduction and valence band of the absorber. This configuration increases the photocurrent thanks to a two-step process where the below-band gap-energy photons can be absorbed. In fact, an electron can be excited from the valence band to the intermediate conduction band and from the intermediate valence band to the conduction band. The next paragraph will be dedicated to the description of the theory of Intermediate Band Solar Cell (IBSC) in order to give more details on the theory which describes this phenomenon.

1.5 Intermediate Band Solar Cells

IBSC is a type of solar cell which allows the S-Q limit to be overcome to reach an efficiency of 63.2% at maximum light concentration [43]. In IBSC

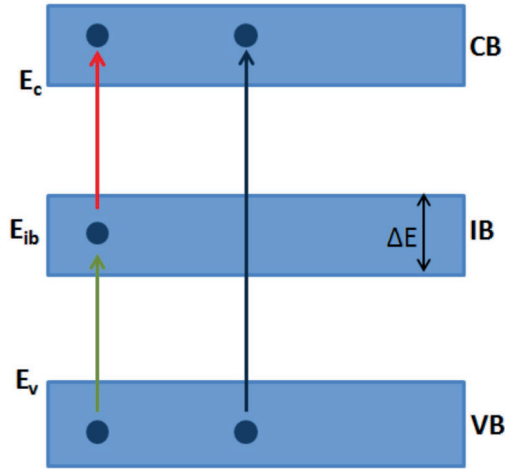


Figure 1.5: Schematic representation of IBSC

an intermediate band of electron states is placed within the main band gap as shown in Fig. 1.5. From Fig. 1.5, one can clearly see how the efficiency is increased: the intermediate band allows electrons to jump from the VB to the CB through a two-step process. Under this configuration it is possible to absorb “three-color photons”. Moreover, in this case, the main band gap can be larger than in conventional solar cells, improving the utilization of the high energy photons. In order for this process to take place, the intermediate band must be half-filled with electrons to supply electrons to the CB and to provide empty space to receive electrons from VB.

It is important to note that in IBSC there are three quasi-Fermi levels. It has been demonstrated that the output voltage of the cell, which is connected with the quasi-Fermi level split $E_{FC} - E_{FV}$, is limited to the band gap of the absorber layer in the solar cell and not to the sub-band gaps [41]. Another consideration is that an energy level within the semiconductor band gap does not behave as a recombination center. Martí and Luque have given arguments to prevent non-radiative recombination [44, 45]. It is important to highlight that the most important characteristic for the intermediate band to avoid recombination is the delocalization of the wave-functions of the electrons. During a recombination process between CB and IB, if the wave-functions of electrons are delocalized, the electron density charge is distributed through different atoms in the initial and in the final states. This means that the transition does not need any interaction of the electron with the impurities due to the presence of the intermediate levels. Since this interaction cannot take place, the possibility that an electron gives its energy to the impurity is forbidden and

thus the non-radiative recombination is avoided [46]. Increasing the density of the intermediate levels beyond the Mott transition is a solution to achieve this result [47]. This may seem illogical considering that the non-radiative recombination is reduced by increasing the intermediate levels which are the cause of recombination. However, it has been proven by experiments that, for example, adding a large quantity of titanium in silicon the non-radiative recombination is reduced [48]. Quantum dots (QDs) have all the properties for use as intermediate materials. Before explaining why quantum dots are useful for intermediate band solar cells and how they can be implemented in the solar cells, a short introduction on the concept of quantum dot will be given in the next section.

1.5.1 What is a Quantum Dot?

Three types of spatial confinements of electron wave function in semiconductor nanostructures are known: *quantum well*, if the confinement is in one direction, *quantum wire*, in two directions and *quantum dot*, in all three dimensions. This confinement of electrons and holes in such a small volume drastically changes the optical and electrical properties of the material. These properties can be fine-tuned by changing the size and the shape of the QDs. A consequence of this confinement is that discrete energy levels are created. This is called the “quantum confinement effect” and it occurs only when the radius of the QD becomes smaller than the Bohr radius, which is defined as the most probable distance between the electron and the hole within an exciton. The Bohr radius is described by the following formula:

$$a_b = \frac{4\pi\epsilon_0\epsilon\hbar^2}{\mu_{eh}e^2} \quad (1.2)$$

where μ_{eh} is the reduced mass of the electron and hole pair (exciton). The Bohr radius varies between 2 and 100 nm, depending on the material.

QDs can be interpreted as a material with characteristics between semiconductor bulk and molecules (Fig. 1.6). Two different approaches are commonly used to explain and describe the energy levels and the properties of QDs. The first approach is called “*Top-Down*”, it starts from the bulk level and considers the effect of the size reduction on the energy levels of the nanocrystal. The second one is called “*Bottom-up*” and it considers the QDs as large molecules describing the energy levels from the orbitals.

1.5.2 Quantum Dots IB Solar Cells

The properties of QDs are suitable to be applied to create Intermediate Band in solar cells. By means of an array of QDs embedded in a high band gap matrix

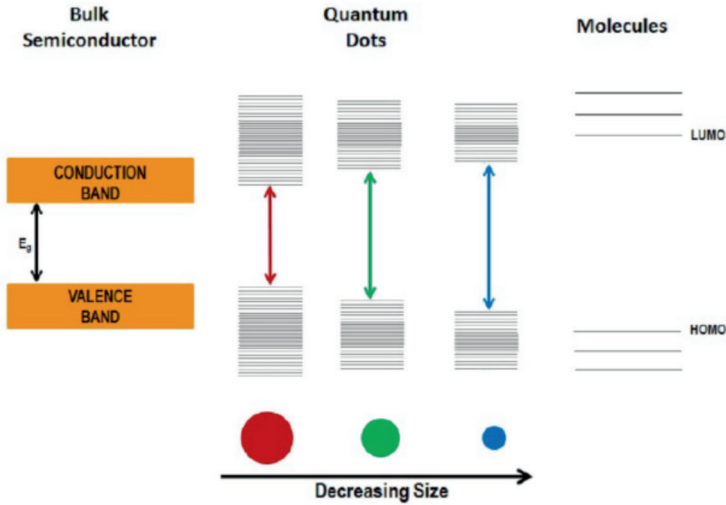


Figure 1.6: Splitting of energy levels in quantum dots due to the quantum confinement effect, semiconductor band gap increases with decrease in size of the nanocrystal. Comparison with bulk semiconductor and molecules.

it is possible to engineer the band structure and the properties, to optimize the performance of the IBSC. It is important to follow some design constraints in order to keep the fundamental properties of the intermediate band. These design constraints can be divided into following points:

Dot size

As mentioned previously, the position of the energy levels changes with the size and shape of the dots. When QDs are placed close to each other, they form an array. It is extremely important that the energy levels are located in the same position to create a band. For this reason it is necessary that the sizes of QDs are mono-dispersive. It has been calculated that this happens when the standard deviation of size distribution is less than 5% [49].

Dot spacing

The dots must be placed as close as possible in order to ensure an overlap of the electron wave-functions. Thus the electron wave function is delocalized, forming a band. Moreover, this ensures a higher absorption without any stimulated emission effect [50]. It has been calculated that 10 nm is the minimum distance for QDs to stay close without generating stimulated emission [51].

Dot density

The dot density is another important parameter to guarantee the formation of delocalized band. The density of the dots can be kept one order of magnitude lower than the conduction and valence bands density of states [52].

Doping

Since the IB must be half-filled with electrons, an important role is played by the doping. However, doping of QDs is still a not clear phenomenon and many studies are still focusing on it.

The first IBSC with QDs was developed in 2004 by Luque et al. [53]. This type of IBSC was made embedding InAs QDs in GaAs matrix by MBE method using the Stranski-Krastanov growth mode [54]. In this work Luque et al. [53] showed an evidence of the splitting between the conduction and the IB quasi-Fermi levels, proving one of the most important working principles for IBSC. However, QDs are very small and do not absorb much light, therefore it is necessary to use many layers of QDs. However, when the number of QDs layers is increased, the cell is prone to getting damaged because of strain effects. Many ideas have been proposed to reduce this problem. Hubber et al. used the same type of solar cell made with InAs QDs in GaAs but adding GaP layers in between InAs layers. In this way the sub-band current was increased using only five QD layers [55]. Oshima et al. [56,57] proposed using a GaNAs spacer layer (strain compensation) between InAs QDs for a cell deposited on GaAs. This method was able to increase the current, but the voltage is limited to GaNAs band gap because this material has a smaller band gap than GaAs.

Despite the fact that physical principles are quite well known and many studies have already understood and described the theory of IBSC, many challenges still remain on how to realize these devices.

1.6 Outline of this thesis

The main objective of this thesis is to employ the characterization of physical and chemical processes to gain know-how on incorporating QD's into thin film CIS solar cells. The QD photovoltaic solar cells will be able to utilize sub-bandgap photons, due to intermediate energy band within the band gap by the incorporation of QDs.

First, in the CIS solar cells used in this work, the CdS buffer layer is substituted with In_2S_3 layer, a non-toxic material. In_2S_3 is a semiconductor material with orthorhombic structure and a band gap of 2.0 - 3.2eV. Tin Sulfide (SnS) QDs have been chosen as intermediate band material because they have suitable band gap (1.0 - 1.5eV) to be embedded in In_2S_3 .

A new synthesis process of SnS QDs has been developed (chapter 3). The optical properties of these QDs have been studied in order to verify whether this type of material has the required characteristics.

Afterwards, to improve the passivation of SnS QDs' surfaces, In_2S_3 material is grown as a shell capping the SnS QDs core (chapter 4).

For electronic device applications it is important to study the conductivity of materials. In chapter 5 two different AFM techniques have been used to investigate the local conductivity of SnS and SnS/In₂S₃ nanoparticles.

In the end, these two types of nanoparticles have been embedded in CI(G)S solar cells (chapter 6). Different configurations have been investigated in order to understand the mechanism and to optimize all the parameters, such as current, voltage and efficiency.

Chapter 2

Experimental techniques

In this thesis different types of materials have been investigated. This chapter is divided into three sections.

The first section is dedicated to the description of the deposition technique used for the deposition of thin films, spray pyrolysis and the method used to grow the shell in the core-shell nanoparticle structure, chemical bath deposition. In the second chapter the techniques used to characterize the optical and electrical properties of materials, both nanoparticles and thin films, are discussed. The second section of this chapter is dedicated to the techniques used to study the properties of materials. At the end, in the third section, an explanation is given of the setups used for the characterization of the complete solar cell devices.

2.1 Deposition techniques

2.1.1 Spray Pyrolysis

Spray Pyrolysis is a simple and low-cost process for the deposition of thin films. The film is made by spraying a solution on a heated substrate. It is simple because it does not require high-quality substrates, and low-cost because it does not need any complex equipment or vacuum component. For these characteristics spray pyrolysis has been used to manufacture low-cost solar cells [58, 59]. According to Viguire and Spitz [60] there are different types of reactions involved in a spray pyrolysis process. From the droplet residing on the surface, the solvent evaporates, leaving behind a solid which can react, reaching a dry state. The solvent can also evaporate before the droplet reaches the surface, in which case the dry solid impinges on the surface and decomposes by chemical reaction. Another possible reaction is that the solvent vaporizes while the droplet approaches the substrate, the solid vaporizes, then the vapor diffuses to the substrate. In the last type of reaction the entire reaction occurs in the vapor state. For all these reactions, the most important parameter is the temperature of the substrate which controls the growth of the film. If the substrate temperature is increased the film can change from having cracked to porous morphology [61]. Changing the deposition temperature, the optical and electrical properties can be controlled [62].

2.1.2 Chemical Bath Deposition

Chemical Bath Deposition (CBD) is a simple method for depositing large-area thin films. Thin chalcogenide semiconductor films are deposited on substrates that are immersed in alkaline solutions containing metal ions, a chalcogenide source ions and added base. There are two possible reactions: one is within the bulk and the other at the surface. The second reaction is used for thin film formation.

The CBD technique was used for the first time to make PbS and PbSe films for photodetectors [63]. In the 1960s CdS films were deposited using CBD to make screen-printed and sintered layers [64]. Only between the 1970s and the 1980s were the chemically deposited thin films used for solar energy applications [65–68]. The main advantage of the CBD method is that it is an easy and cheap deposition method because it needs only a solution container and a substrate mounting device (Fig. 2.1) and a low process temperature.

One of the disadvantages is that the solution has to be discarded after every deposition. Nevertheless, CBD is a suitable method to make high-quality thin films in a simple manner. Furthermore, the films deposited by CBD are stable, adherent and uniform.

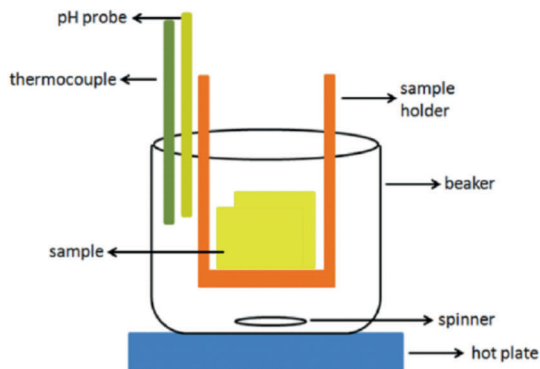


Figure 2.1: Schematic illustration of Chemical Bath Deposition

2.2 Material Characterization

2.2.1 TEM-HRTEM

When high energetic electrons interact with matter they can be (back)scattered, and the interaction can also be a source of X-rays, Auger electrons and photons. Some of these electrons are even able to travel across the material and thus be transmitted. The transmitted electrons are used for Transmission Electron Microscopy (TEM). A conventional TEM consists of condenser lenses, usually two, which are used to focus the beam of electrons on the sample; one objective lens which stops the undesired e-beams; some intermediate lenses implemented for transmitting and magnifying the first enlarged image or diffraction pattern to the projector lens and finally there is the projector lens that projects the image or diffraction pattern to the screen. A schematic drawing of TEM is shown in Fig. 2.2. TEM allows one to resolve images of a few nanometers, with atomic scale resolution. It is important that the thickness of sample is thin, with a maximum thickness of 100 nm, otherwise it would be impossible for the electron beam to pass through the sample. On the other hand, if the sample is too thin, the image has a low contrast. To solve this problem an objective diaphragm is added to select the transmitted beam. The diaphragm is placed in the back focal plane of the objective lens to allow only the direct transmitted beam to pass through, and in the resulting image the crystalline parts appear dark and while amorphous parts appears bright. This mode is called bright field mode. Moreover, TEM can also work in dark mode, which is commonly used to study the diffraction pattern. The diffraction spectrum consists of different phases: each phase can be selected with the objective diaphragm. The beam is tilted and the diffracted beam is focused on the objective lens in order to avoid

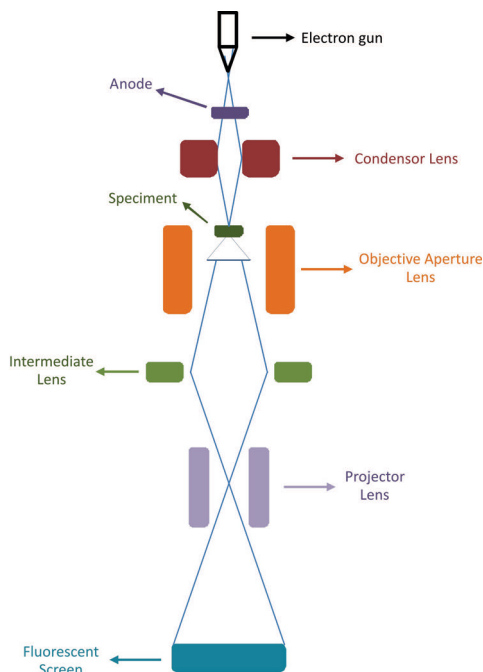


Figure 2.2: Schematic illustration of Transmission Electron Microscope.

aberrations. TEM measurements commonly use only transmitted beams or scattered beams to get a diffraction contrast image, however, it is also possible to use both the beams simultaneously to create an interference image. This is used in High Resolution Transmission Electron Microscopy (HRTEM). HRTEM measurements increase the resolution of the image and allow one to even detect the lattice fringes, giving information about the crystalline structure of the material.

2.2.2 SAED-EDX

The analysis of the structure of materials can be carried out by selecting a small area in the TEM image of the sample and using the selected area diaphragm. This mode is called Selected Area Electron Diffraction (SAED). If the material is crystalline, the diffraction pattern shows concentric rings, each ring corresponding to different plane orientations. SAED permits one to obtain the symmetry of a lattice and to calculate its interplanar distances using Bragg's law.

For the chemical characterization, Energy-dispersive X-ray spectroscopy (EDX or EDS) is used. This technique is based on the interaction between an X-ray beam and the material. Since each element has a unique atomic

structure, by studying this interaction it is possible to identify the component elements of the sample. A beam of X-ray is focused on the sample and it interacts with the electrons of the material. It is known that the electrons in an atom are placed in discrete energy levels. This beam can excite an electron of an inner shell of the atom, creating a hole. Afterward, another electron from an outer energy level fills the hole, and an X-ray is emitted to balance the energy difference between the two electrons' states. This X-ray energy is characteristic of each element from which it is emitted.

2.2.3 Optical absorption

To study the optical absorption three setups have been used: a dual-beam spectrometer (Perkin Elmer Lambda 2S) to investigate the absorption of quantum dots in solution; an UV-VIS spectrometer, Perkin Elmer lambda 2S, to explore the reflection and transmission behavior in thin films; Photothermal Deflection Spectroscopy (PDS) to investigate both, quantum dots and thin films.

2.2.3.1 Dual-beam UV-VIS spectroscopy

UV-VIS spectroscopy is used to investigate how the material responds to light. When a beam of light passes through the material and part of the light is absorbed, the rest is transmitted. If I_0 is the intensity of the incident light, after the interaction with the sample the intensity of transmitted (I_T) is less than I_0 . The ratio between I_0 and I_T , at a particular wavelength, is called transmittance T , and it often is expressed in percentages. From the transmittance, the absorbance can be calculated; indeed, the absorbance is defined as the negative logarithm of the transmittance (neglecting reflectance).

To investigate the absorbance of quantum dots in the UV-VIS region, a dual-beam spectrophotometer has been used. In Fig. 2.3 a schematic design of the tool is shown.

The beam is split, by means of a half-mirror, to pass through the sample (e.g., cuvette filled with a solvent in which the sample is dissolved) and the reference (e.g., cuvette with pure solvent). Each beam has its own detector. The main advantage of this setup is the possibility to measure simultaneously I_T and I_0 .

2.2.3.2 R/T measurements

To investigate the reflection and transmission spectra of thin films a UV-VIS (Perkin Elmer 2S) spectrometer has been used. This setup is equipped with an integrating sphere which allows one to take into account of all the contributions. Furthermore, specular, total and diffuse reflection and transmission

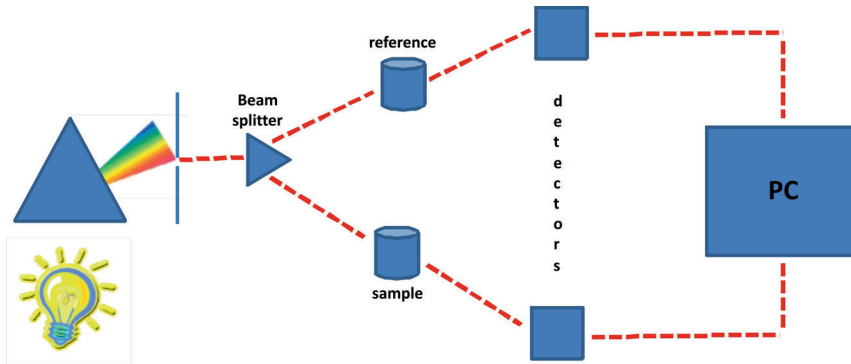


Figure 2.3: Dual-beam spectrophotometer design.

can be investigated separately. The only disadvantage is that reflection and transmission measurements cannot be carried out simultaneously since these measurements need two different configurations of the setup. When the reflection (R) and the transmission (T) are known, it is possible to determine the absorption using the following formula:

$$\alpha = -\frac{1}{d} \ln \frac{T}{1-R} \quad (2.1)$$

where d is the thickness of the film.

2.2.3.3 Photothermal Deflection Spectroscopy

Photothermal Deflection Spectroscopy (PDS), called also “Mirage Effect”, is a sensitive spectroscopic technique to measure directly the optical absorption and the thermal properties of the materials. It is known that when the light hits a material, a portion of the energy is absorbed, a part (non-radiative recombination) of which will be converted into heat. The physical principle of this technique is simple. It is based on the detection of the heat produced within the material, due to de-excitation mechanism caused by the absorption of the light. The sample is placed in a cuvette containing a special liquid, called F40. The refraction index of this liquid depends heavily on the temperature changes. When the modulated beam of the electromagnetic radiation hits the medium, heating will arise. With the change in the temperature in the medium, there is a corresponding change in the refraction index, with the consequence that the beam will be deflected with a different angle. This angle is proportional to the absorption. A schematic drawing of this setup is given in Fig. 2.4. PDS technique is useful for studying ultra-low absorption. In fact, it has been demonstrated that it is possible to measure absorption on the order of 10^{-7}cm^{-1} . More information can be found in the reference [69].

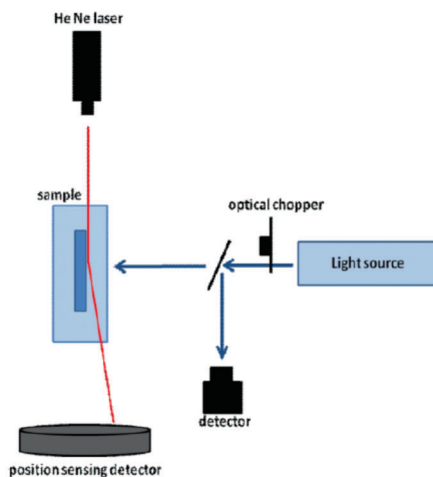


Figure 2.4: Schematic illustration of Photothermal Deflection Spectroscopy setup.

2.2.4 XRD

X-ray diffraction (XRD) is a technique for measuring the structure of materials, giving information on the grain sizes and structural orientation of different thin films. X-rays with a wavelength of 0.15428 nm, coming from K_{α} radiation of a copper anode, are diffracted by the material according to the Bragg's law:

$$\lambda = 2d\sin\theta \quad (2.2)$$

where d is the distance between the parallel crystal planes and θ the angle between the scattering plane and the X-ray beam.

XRD measurements are carried out by varying the angle between the X-ray beam and the detector in order to determine the diffraction angles. The measurements are performed in θ - 2θ configuration, i.e., the position of the detector is 2θ respect to the incident beam. The positions of the peaks caused by the diffraction are unique for each crystal structure of the material, they act as “finger-print” for materials. The software used for these measurements also contains a database, called ICDD, which contains all the peaks for different types of materials. From the comparison between the diffraction peaks of the acquired spectrum and those in the database it is possible to determine the type and the phase of the material. It is also possible to determine the crystal orientations using the lattice constants and the interplanar crystal distance, but the first method is the easiest.

The average grain size can be calculated by the Scherrer formula:

$$\gamma = \frac{0.9\lambda}{FWHM(2\theta)\sin\theta} \quad (2.3)$$

where FWHM is the Full-Width at Half Maximum of the XRD peaks.

2.2.5 Conductivity and activation energy

Electrical properties were investigated by studying the photo and the dark conductivity. For these measurements the samples were prepared by depositing thin films on corning glass and depositing two coplanar Ag contacts by thermal evaporation. The conductivity has been measured applying a voltage between the two metal contacts and measuring the current. The value of the conductivity has been determined using the following formula:

$$\sigma = \frac{I\omega}{Vld} \quad (2.4)$$

where I is the measured current, V is the applied voltage, ω is the width between the two metal contacts, l is the length of the contacts and d is the thickness of the thin films.

The activation energy has been determined by studying the temperature-dependent dark conductivity. The relationship between the temperature-dependent dark conductivity and the activation energy is given in formula 2.5:

$$\sigma_d(T) = \sigma_0 \exp\left(-\frac{E_a}{kT}\right) \quad (2.5)$$

using the logarithmic it is possible to see, in formula 2.6, that the activation energy is determined by the slope of this Arrhenius plot:

$$\ln[\sigma_d(T)] = \ln(\sigma_0) - \frac{E_a}{kT} \quad (2.6)$$

where σ_0 is the conductivity prefactor, k is the Boltzmann's constant and T is the absolute temperature.

2.2.6 Scanning Tunneling Spectroscopy

In 1981 Gerd Binnig and Heinrich Rohrer developed a new type of microscope that allows the morphology of surfaces to be observed at the atomic level. This new microscope is called Scanning Tunneling Microscope (STM) and for this discovery Binnig and Rohrer were awarded the Nobel Prize in 1986 [70].

The working principle of STM is based on the quantum tunneling effect. A conductive tip, usually made of W or Pt-Ir, is brought close to the surface of the sample and a bias is applied between the tip and the sample. This bias allows

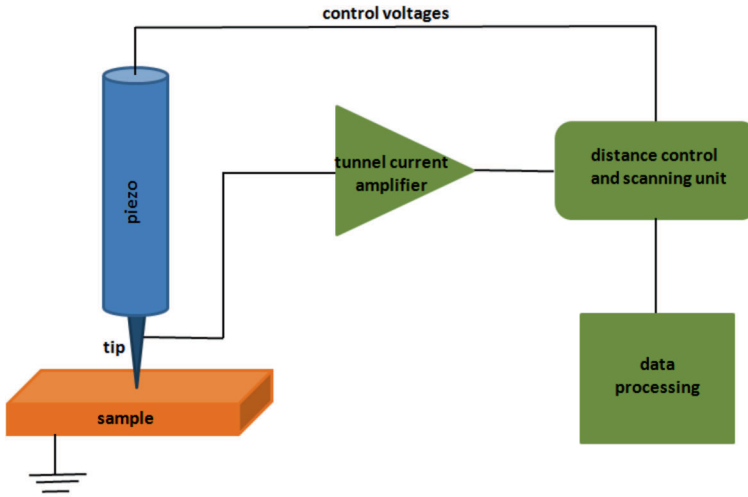


Figure 2.5: Diagram of a scanning tunneling microscope

the tunneling of electrons, thus allowing the tunnel current to be detected. STM measurements can be carried out under high vacuum conditions. Two modes can be used to study the topography. The first is by scanning the samples while the tunnel current is kept constant and feedback is used to adjust the distance between tip and sample. The other mode is to scan keeping the height constant. In this mode the tunnel current as a function of the tip position is measured. A schematic diagram of an STM set up is shown in Fig. 2.5.

STM can also be used to investigate the local density of electronic states of the material under study. In this case it refers to Scanning Tunneling Spectroscopy (STS) [71]. By means of STS it is possible to obtain information about the band gap of materials or surfaces. The simplest spectrum that can be acquired by STS is obtained by placing the tip on the sample. Then, the tunnel current is measured as a function of the applied voltage. An I-V curve is recorded. The slope of this curve at each voltage is proportional to the electron density of states at that energy (eV) position. For this reason, usually the derivative $dI/dV-V$ is investigated for studying the density of states and the band gap.

2.2.7 Atomic Force Microscopy

Atomic Force Microscopy (AFM) belongs to the Scanning Probe Microscopy (SPM) family. AFM allows one to study the 2D and 3D profile of the sample surface at nano-scale, by measuring the forces between the probe and the sur-

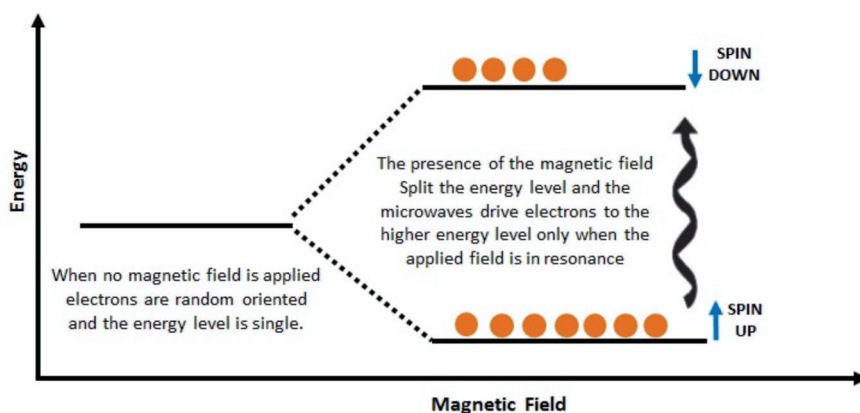


Figure 2.6: Description of the splitting of the energy level due to the magnetic field and changing in the orientation of the spins.

face of the sample at a short distance. Usually these forces are used as feedback, and thus they are kept constant during the measurements. The probe has a very sharp tip, on the order of 0.2 - 10 nm, and it is supported by a flexible cantilever. The cantilever can be thought of as a spring. Hence, the force can be described using the Hooke's Law, $F = -kx$, where x is the distance between the tip and the sample and k is the spring constant. Then, the cantilever bends, following the morphology of the surface, and the deflection is monitored. Thus, it is possible to reconstruct the surface morphology.

This is a short introduction to this technique, in chapter 5 AFM will be described in details.

2.2.8 ESR

Electron Spin Resonance (ESR) is a spectroscopic technique that is used to detect the chemical species that have unpaired electrons. A large number of materials can be studied by ESR, such as free radicals [72] and, transition metal ions [73]. Moreover, ESR allows the defects (paramagnetic) in the material to be investigated [74]. The working principle is based on the fact that paramagnetic molecules have unpaired electron spins.

It is known that the electron spin is responsible for the magnetic properties, called the magnetic moment. Hence, the electron behaves as a small magnet. When a magnetic field is applied, the paramagnetic electrons (spins) can orient themselves in parallel or anti-parallel directions compared with the direction of the magnetic field (Fig. 2.6) with a splitting of energy levels of $+1/2$ and $-1/2$ spins..

This splitting is due to the Zeeman effect. When the material under a static

magnetic field is swept with microwave frequency radiation, a proper frequency can cause a transition (spin flip) from one spin state to the other. However, in practice, ESR uses a fixed frequency (normally X at 8-10 GHz or Q band at 34 GHz) of microwave irradiation and the magnetic field is swept to excite electrons from the lower to the upper energy level. The energy associated with these transitions can be express as:

$$\Delta E = \mu_B \cdot g \cdot B_0 \quad (2.7)$$

where B is the magnetic field, g is the Lande g-factor, and μ_B the Bohr magneton. Usually the Lande g-factor is equal to 2.0023 for free electrons. The g-values of paramagnetic species shift from the free electron value due to spin orbit coupling, which depends heavily on the delocalization of electrons' wave function. Normally a g-marker, such as DPPH with a g-value of 2.0036, is used to calibrate the g-values.

The absorption of the electromagnetic radiation induces transition at resonance frequency from the low energy level to the higher one. The occupation of the lower and upper energy levels is governed by Boltzmann statistics due to spin-lattice relation.

The setup used for this experiment is made of a computer that allows one to control the spectrometer, a cavity or resonator where the sample is placed in, the microwave bridge that provides the microwave and the detection circuitry, a water-cooled iron electromagnet for the external magnetic field, a console to control the magnet, the microwave bridge and the EPR signal [75].

2.3 Devices Characterization

2.3.1 Solar simulator

The most important parameters of solar cells are, open circuit voltage (V_{OC}), short circuit current (I_{SC}), fill factor (FF) and efficiency (η). The V_{OC} is the voltage when the current does not flow in the circuit, (when the external resistance is (ideally) infinite). The I_{SC} is the current corresponding to when the contacts are connected, (when the external resistance is (ideally) zero). Since the I_{SC} is proportional to the area of the solar cell, usually the current density, J_{SC} , is used to compare solar cells. A solar cell is schematically represented as a diode. For this, without illumination, the dark current density is given by:

$$J_{dark} = J_0 \left(e^{qV/nkT} - 1 \right) \quad (2.8)$$

where J_0 is a constant, q the electron charge, V the voltage between the contacts and n the diode quality factor. The diode quality factor gives an indication of

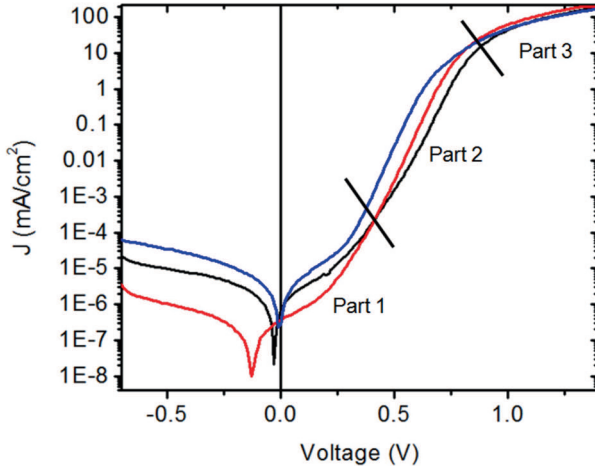


Figure 2.7: An illustration of a dark J-V curve of a solar cell.

carrier transport in the cell that is a composite of diffusion and drift currents.

Under illumination the current density becomes:

$$J(V) = J_{SC} - J_0(e^{qV/kT} - 1) \quad (2.9)$$

Combining the previous formulas, the expression of the open circuit voltage can be found:

$$V_{OC} = \frac{KT}{q} \ln\left(\frac{J_{SC}}{J_0} + 1\right) \quad (2.10)$$

The power density from a power source is

$$P_s = JV \quad (2.11)$$

The maximum power density occurs between $V=0$ (short circuit), and $V=V_{OC}$ at voltage V_M . There is a current density called J_M that corresponds to this voltage V_M . These two parameters play an important role in determining the Fill Factor (FF) which is defined as:

$$FF = \frac{J_M V_M}{J_{SC} V_{OC}} \quad (2.12)$$

FF gives a measure of how much of open circuit voltage and short circuit current is “utilized” at maximum power. Now it is possible to write the expression for the efficiency, which is defined as:

$$\eta = \frac{J_{SC} V_{OC} FF}{P_S} \quad (2.13)$$

In this description the parameters have been described as for an ideal diode, but in reality the resistances must also be considered. A typical dark J-V measurement is reported in Fig. 2.7 where it is possible to clearly distinguish three parts. In the 1st part it is possible to get information about the parallel resistance (R_P), higher current density means smaller R_P . The 2nd part gives information about the diode quality factor, an abrupt slope means a smaller n value. In the end, analyzing the 3rd part, the series resistance (R_S) can be studied; when the current density is higher the R_S improves. This is indicative for analyzing the contact structure. In this case the current density is:

$$J = J_{SC} - J_0(e^{q(V+JAR_S)/kT} - 1) - \frac{V + JAR_S}{R_P} \quad (2.14)$$

The series resistance is due to the fact that a solar cell is not an ideal conductor. The parallel resistance is caused by some leakage of current between the contacts. For an ideal solar cell the R_S should be zero and the R_P infinite.

2.3.2 Quantum efficiency

The quantum efficiency is the number of electrons extracted from the solar cell compared with the number of the incident photons. This basically describes the sensitivity of the solar cell to the radiation of different wavelengths. The Quantum Efficiency (QE) is defined as:

$$QE = \frac{J_{ph}(\lambda)}{q\Phi_{ph}(\lambda)} \quad (2.15)$$

in which $\Phi_{ph}(\lambda)$ is the incident number of the photons with wavelength per unit area per second. From the collected current at different wavelengths, external collection efficiency (EQE) is obtained. From EQE the J_{SC} can be calculated using the formula below:

$$J_{SC}^{SR} = e \int QE(\lambda)\Phi(\lambda) d(\lambda) \quad (2.16)$$

In this work a home-made EQ setup has been used. The cell is illuminated with a modulated light beam; an optical chopper, a monochromator and a lock-in amplifier has been used to measure the photocurrent. The solar cell can be measured under white bias light and bias voltage.

Chapter 3

Synthesis and Characterization of SnS nanoparticles

In the last years nanoparticles have attracted interest because of their optical and electrical properties, which are different from those of bulk semiconductors. Using nanomaterials it is possible to change the band gap which is size-dependent and making the optical properties tunable. So far, research has been focused on the study of IV-VI semiconductor nanoparticles such as CdS, CdSe, PbS, PbSe and SnTe because of their easy synthesis. However, Cd and Pb are toxic elements, and their applications for devices have thus been limited. Tin sulfide is a good material for overcoming these problems, because both tin and sulfur are non-toxic.

In this chapter a new way of synthesizing of SnS quantum dots is described. This synthesis is an easy colloidal route at room temperature that allows nanoparticles to be obtained with sizes between 2 and 4 nm. These nanoparticles have been studied using optical and electrical measurements. The absence of the exciton peak has lead us to think that the nanoparticles were doped. A complete section is dedicated to investigating the doping effect using STM and ESR techniques. This study made it possible to draw the energy band of SnS nanoparticles.

Finally, thin films of SnS QDs are characterized in order to verify if, even after the deposition, the QDs retain their properties.

3.1 Introduction

In the early 1980s Efros [76], Ekimov [77], Henglein [78] and Brus [79] started their pioneering work on semiconductor nanoparticles. Since then, semiconductor nanoparticles have received great interest because of their enormous potential in many different fields. As mentioned in the short introduction to the properties of nanomaterials in chapter 1, nanoparticles are in a transition phase between the bulk material and molecules, with a property of matter, called “quantum confinement effect” when the particles reach a critically small size. A popular academic demonstration of this special effect is the drastic change of color in nanoparticles in solution, as the particles decrease in size, attributed to a shift of the band gap. At the nanoscale other properties also change with respect to the bulk, such as the melting points and charging energies, which is the energy necessary to charge a tunnel junction with one elementary charge.

The most common synthesis used to make nanoparticles is the colloidal route, by which nanoparticles are made in a suitable solvent medium. This method is also referred to as “bottom-up”. On the other hand, the “top-down” method, such as methods based on lithographic techniques, is a comparatively difficult approach. For this reason the first method is preferred to the second one. Using a colloidal method, Murray et al. [80] synthesized mono-disperse cadmium chalcogenide nanoparticles by means of a rapid injection of precursors into a hot solvent, and they were able to vary the particle size between 2 and 12 nm. Nowadays, by means of the chemical approach, it is possible to control the particle size, the shape, the composition and the crystallinity. To achieve this result, it was extremely important to improve the surface chemistry because the surface of a nanoparticle plays a crucial role in the size dispersion. To keep the particles small it is necessary to arrest the precipitation, and by using stabilizing agents, called ligands, to passivate the particles and prevent them from clustering. Choosing the proper ligands is very important because they regulate the growth of the nanoparticles and their size. Moreover, ligands prevent oxidation and create a dielectric barrier at the surface, reducing the surface traps. The ligands consist of two parts: one is non-polar and is usually made of a long alkyl chain and the other part is a polar head [81]. The functionality of these ligands depends on both the parts. The tail, which is non-polar, affects the diffusion properties, while the polar head affects the binding efficiency.

In recent years much attention has been given to the IV-VI semiconductor nanoparticles such as CdS, CdSe, PbS, PbSe and SnTe. These nanoparticles can be easily synthesized due to their cubic structure and they can be used for solar cell applications because the band gap of these materials covers the entire near-infrared region [82–91]. However, the toxicity of Cd and Pb limits their

application for consumer devices.

Tin sulfide (SnS) can be a good alternative for overcoming this problem since both elements in this compound are non-toxic. Moreover, both these elements are highly abundant on Earth. SnS is a IV-VI semiconductor with a direct optical band gap of 1.3 eV and an indirect band gap of 1.09 eV [91]. Moreover, SnS has a high optical absorption strength (absorption coefficient higher than 10^4 in the visible wavelength range) and high photo-conductivity, necessary properties for photovoltaic applications [92–94]. Nevertheless, tin chalcogenides have not been intensively studied compared to the Pb compounds.

Various methods have been developed for the synthesis of SnS nanoparticles with different sizes and shapes, for example by a precipitation reaction between Tin(II)chloride (SnCl_2) and thioacetamide (TAA) [95] and using a solution dispersion method [96]. Gou et al. [97] synthesized SnS NPs through a precipitation reaction between $\text{SnCl}_2 \cdot 2\text{H}_2\text{O}$ and thioacetamide (TAA) in an acid aqueous solution at 60°C. These SnS NPs have an average diameter of 30 - 100 nm. Zhao et al. [98] developed a new route to prepare SnS NPs by dispersing molten tin in a sulfur-dissolved solvent. They were able to obtain crystalline nanoparticles with a size of around 200 nm.

Among these different methods to synthesize SnS nanoparticles one deserves to be highlighted. This method, developed by Koktysh et al. [95] allows one to synthesize SnS nanoparticles by solvothermal decomposition using a single source precursor, bis(diethylthiocarbamate) tin(II) in oleylamine. By controlling the reaction temperature and time and depending on the nature of the ligands, the size and the shape of the nanoparticles can be fine-tuned. Nevertheless, most of the studies using these methods have been unsuccessful in synthesizing SnS quantum dots (QDs), nanoparticles with size smaller than Bohr radius, which has been calculated for SnS nanoparticles to be 7 nm [99, 100].

So far, few publications have described methods to make mono-dispersive SnS QDs. Xu et al. [96], have succeeded in synthesizing SnS QDs in solution using SnBr_2 and Na_2S as precursors and thiethanolime (TEA) as a ligand. The QDs obtained with this recipe have a size of $3.2 \text{ nm} \pm 0.5 \text{ nm}$. The nanoparticles, size and monodispersity have been controlled changing the number of hydroxyl groups of the ligands. SnS with a size of 5 nm have been synthesized by Ning et al. [91] using the reaction of $(\text{Sn}_6\text{O}_4(\text{OH})_4)$ with thioacetamide. Liu et al. [101] succeeded in making 6 nm SnS nanoparticles using as precursor SnCl_2 and $[(\text{CH}_3)_3\text{Si}]_2\text{S}$ in oleylamine.

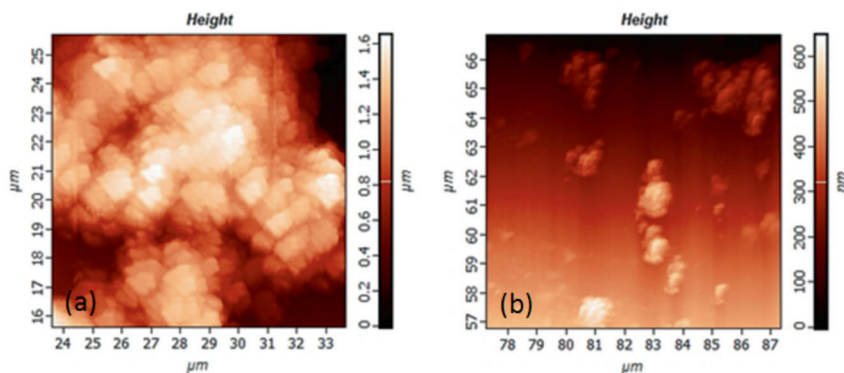


Figure 3.1: AFM topography images of a self-assembled layers of SnS nanoparticles synthesized using colloidal routes A (left) and B (right).

3.2 Synthesis

In the beginning of this research, two colloidal routes were investigated; one using a SnCl_2 solution with thioacetamide in ethanol (route A) and the other one using solutions of SnBr_2 and Na_2S in ethylene glycol as precursors and triethanolamine as a surfactant (route B). The synthesis reactions have been performed under Ar atmosphere, at 60°C for route A and at room temperature in route B. It was possible to synthesize SnS nanoparticles by means of both these routes. Nevertheless, the size of nanoparticles is quite large. Nanoparticles have a size between 80 and 300 nm for route A and in the range of between 50 and 100 nm for route B. By AFM it was verified that clustering of nanoparticles takes place as shown in Fig. 3.1. Moreover, the presence of SnO_2 was detected in the particles made by route A, which is speculated to be due to the ethanol medium. For this reason the synthesis route B was chosen for further studies and ethylene glycol was the preferred medium. X-ray diffraction (XRD) measurements have established that SnS nanoparticles crystallize as a zinc-blende structure, unlike most reports showing a orthorhombic structure, and no oxide presence was traceable (Fig. 3.2).

It is known that adding triethanolamine or other type of ethanolamine ligands increases one's control of the particle size. In our experiments we used triethanolamine (TEA), N-methyldiethanolamine (MDEA), and N,N-dimethylethanolamine (DMEA). With all of these surfactants the nanoparticles showed the same brownish color, and they were stable in ethylene glycol before washing. Nevertheless, the smallest NPs have been obtained using TEA, as described in the following paragraph. Moreover, it was found that traces of water present in the solution influence the chemical composition of the nanoparticles. To

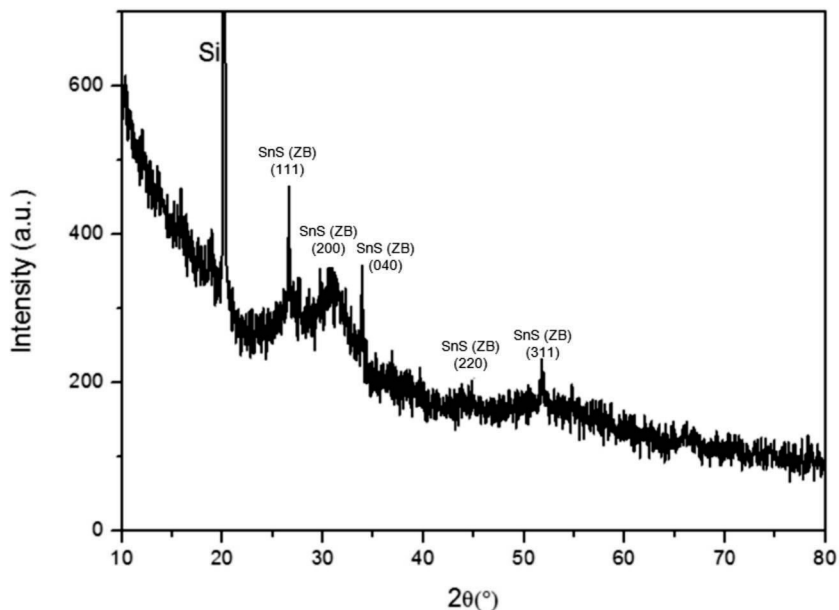


Figure 3.2: X-ray diffraction patterns of colloidal SnS nanoparticles.

avoid this issue the synthesis was carried out under inert atmosphere, under dry N_2 instead of Ar. With this change route A, using $SnCl_2$, also gave better results, showing no traces of oxides. This does not depend on the type of gas but mainly on the dryness of the gas used.

3.3 Final synthesis and characterization

After the above-described experiments we found a stable and reproducible synthesis. This is a facile, room temperature synthesis of SnS nanoparticles using the colloidal route. $SnCl_2$ (Sigma Aldrich) mixed with triethanolamine (TEA) (Acros) and Na_2S (Sigma Aldrich) were used as precursors; both solutions were in an ethylene glycol (Sigma Aldrich) medium. TEA is a stabilizing/complexing agent which enables ‘separation’ of individual Sn atoms during the reaction. It has been reported that TEA can create chelate with Sn^{2+} with general formula of $[SnS(TEA)_n]^{+2}$ [102].

To avoid clustering, trioctylphosphine oxide (TOPO) has been added to the first precursor. TOPO is a compound with the formula $OP(C_8H_{17})_3$ used to coat the QDs. It is used to control the growth and passivate the surface. Moreover, due to its hydrophobic tail, TOPO helps to keep the nanoparticles separated. The synthesis is performed at room temperature under dry nitrogen

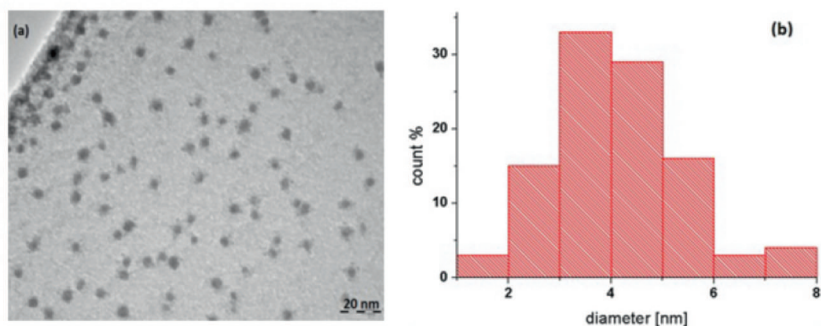


Figure 3.3: (a) Planar TEM image of SnS nanoparticles, (b) the histogram of the size distribution of SnS nanoparticles for this sample.

atmosphere. The sodium sulphide solution was added drop wise to SnCl_2 under vigorous stirring. The resulting nanoparticles have been separated by centrifugation and then washed four times in ethanol. Dispersions of TOPO-capped QDs in ethanol appeared to be the most stable. The nanoparticles were “soluble” in Ethanol. However, a certain degree of agglomeration was visible in concentrated dispersions, and this could be attributed to preferential orientation of the non-polar groups of TOPO to avoid exposure to the polar solvent (ethanol).

Characterization of these nanoparticles was carried out by means of various techniques for studying their optical and structural properties. The optical absorption was investigated using UV-VIS dual beam spectroscopy (Perkin-Elmer Lamda 2S) and photothermal deflection spectroscopy (PDS). The shape and the size of the nanoparticles were studied with planar transmission electron microscopy (TEM) using a TECNAI12 with a beam of 120 kV, but the energy of this electron beam did not allow the study of the crystalline structure. For this reason a high resolution transmission electron microscopy (HRTEM) imaging with a beam of 200 kV has been used, the higher energy beam allowed imaged to be obtained with a resolution high enough to visualize the lattice fringes. The samples for both TEM measurements were prepared by dispersing nanoparticles in ethanol and dropping this solution onto a lacey carbon coated copper grid.

The TEM image in bright field, shown in Fig. 3.3a shows a uniform distribution of SnS nanoparticles with spherical shape of around 4 ± 2 nm in size, smaller than Bohr radius (Fig. 3.3b). The size distribution was calculated considering one hundred nanoparticles. In the HRTEM image in Fig. 3.3a somewhat blurred atomic lattice fringes are visible, indicating the crystalline nature of the nanoparticles. Moreover, selective area diffraction pattern (SADP) (Fig. 3.4b) has been carried out in order to check the structure of the material:

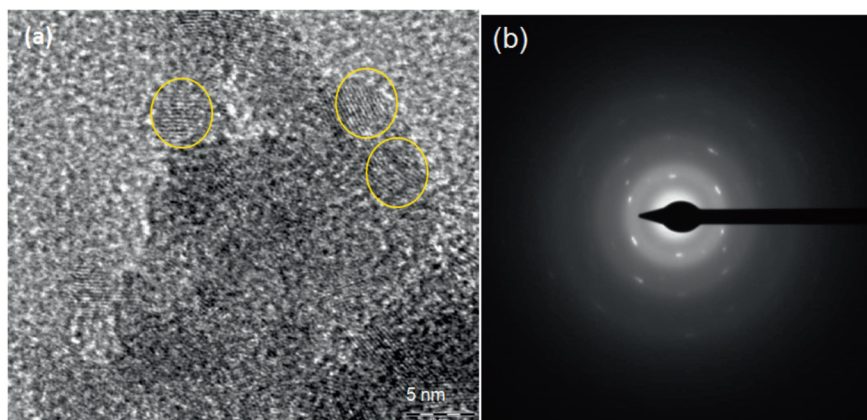


Figure 3.4: (a) High Resolution Transmission Electron Microscopy (HRTEM) image and (b) selective area diffraction pattern (SADP) image of SnS nanoparticles.

it shows clear diffraction rings with bright spots, confirming the crystalline nature of the nanoparticles.

The chemical composition of the SnS on TEM grid has been studied using energy dispersive X-ray spectroscopy (EDX), according to which (Fig. 3.5) the ratio S:Sn is 1:1, confirming that the semiconductor is SnS and not some other alloy.

Optical absorption measurements were carried out using a dual beam UV/VIS spectrometer (Fig. 3.6a) on nanoparticles dispersed in a solution in a quartz cuvette. The samples have been prepared in a glovebox under nitrogen flow to avoid any reaction with the air. The absorbance, in this case, has been obtained using transmission-reflection measurements. SnS nanoparticles show heavy absorption in the VIS/NIR range (Fig. 3.6a). The optical absorption has also been investigated using the Photothermal Deflection Spectroscopy (PDS) technique (Fig. 3.6b), because this technique is a direct measurement of optical absorption and allows one to study absorption with a high sensitivity; it is possible to observe the absorption coefficient up to 10^{-7} cm^{-1} . This high sensibility makes it possible to obtain more accurate information about the band gap. For this measurement SnS nanoparticles were deposited on a quartz substrate by drop casting, making a layer. In the PDS spectrum, (Fig. 3.6b), the absorbance is presented in logarithmic scale to identify the absorption edge. The PDS spectrum indicates that the band gap is around 1.6 eV, in accordance with the values reported in the literature [91,95].

What is surprising is the absence of the exciton peak expected for a QD, as well as the fact that the absorption spectrum (Fig. 3.6a) shows two sharp peaks in the infrared region at 0.62 eV and 0.84 eV. PDS measurements also

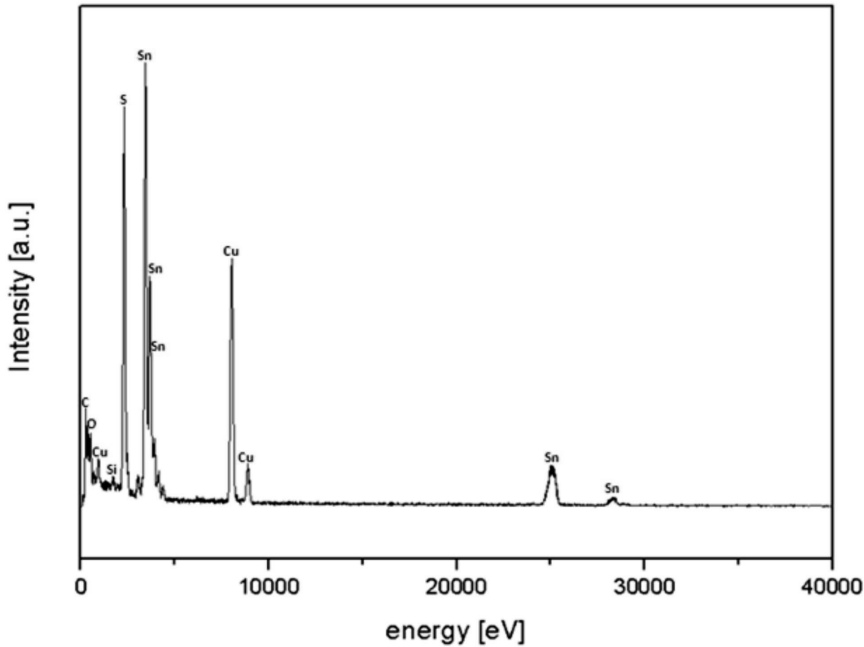


Figure 3.5: Energy dispersive X-ray spectroscopy (EDX) on SnS nanoparticles.

show peaks in the infrared region with the same energy values as seen in R/T measurements. Furthermore, the absorption spectrum acquired by PDS shows the presence of another peak at 0.4 eV as reported in Fig. 3.6c, which suggests the presence of additional electronic states of SnS.

These results suggest the presence of dopant electrons occupying electronic states of SnS, which can simultaneously explain the presence of an infrared peak at 0.4 eV (Fig. 3.6c) and the absence of excitonic peak (Fig. 3.6a) typically observed for a quantum dot. To understand this hypothesis it is necessary to explain the doping effect in quantum dots.

3.4 Doping in Quantum Dots

It is possible to modify the optical, electrical and magnetic properties of bulk semiconductors by controlling the charge carriers. This control usually is done by doping, introducing impurities which can add carriers in the crystal, or by charging using an electric field which manipulates the carrier density [103]. While for bulk semiconductor the doping is routine, for quantum dots it is still an unclear and complex phenomenon [104]. This is due to the nanometer size. For bulk crystal, adding one dopant atom for 10^{-5} atoms will be considered

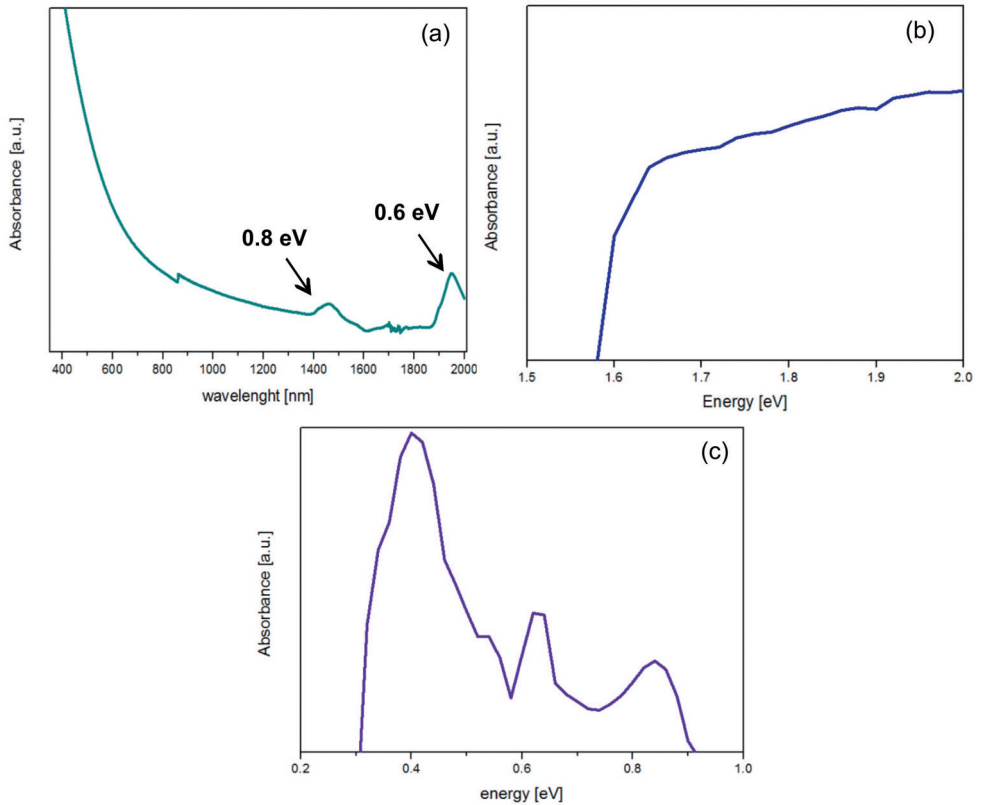


Figure 3.6: Absorption spectra for SnS nanoparticles using a dual beam spectrometer (a), which show a continuous absorption in the visible region and two peaks, at 0.6 and 0.8 eV, in the infrared region. PDS spectrum (b), plotted in logarithmic scale, in the visible range clearly shows the band gap at almost 1.6 eV. An absorption spectrum in the infrared region acquired by PDS (c), the absorbance in log scale, shows the presence of three peaks, at 0.6 and 0.8 eV, as seen for the dual beam spectrum, and another strong peak at 0.4 eV.

heavy doping, whereas for a 4 nm nanoparticle consisting of around 1,000 atoms, to introduce an impurity into the quantum dot, the dopant level is a whole 2 orders of magnitude higher [103]. There is another problem even if the dopant level is low: in quantum dots the impurities tend to outdiffuse to the surface. So far, the main challenge for doping is to develop a synthesis that is able to introduce impurities into the core and not just onto the surface. Over the last ten years many efforts have been made in n- and p-type doping of semiconductor QDs [105]. The first work reported on this effort is by Shim and Guyot-Sionnest in 2000 [106]. They did not use substitutional or interstitial impurity in the bulk host but instead made n-type doped quantum dot by injecting extra electrons. These extra electrons occupy the Lowest Unoccupied Quantum-Confined Orbital (LUQCO), called $1S_e$, making the quantum dot n-type. Optical spectroscopy allows one to study this phenomenon. A proof of the presence of an electron in the LUQCO is the bleaching of the exciton transition due to the occupation of the LUQCO and the appearance of a strong infrared peak corresponding to a transition from $1S_e$ to the next higher energy level, called $1P_e$ [106].

As was said in the previous paragraph our SnS nanoparticles do not show any exciton peak. However, there are three peaks in the infrared region. To explain the absorption transition an SnS band diagram is proposed Fig. 3.7.

The strong peak at 0.4 eV can be attributed to the transition due to the presence of a dopant electron placed at the $1S_e$ energy level, which can jump to the $1P_e$. It has been demonstrated [106] that when an electron is transferred to the LUCQO an infrared transition and bleaching of the exciton transition must be seen. An infrared transition peak is expected in the same range of energy.

To confirm our hypothesis it was necessary to ascertain the presence of a free electron. With this aim, conventional continuous wave ESR measurements were performed with a commercial X-band ($\nu=9.3$ GHz) Bruker ELEXSYS E500 spectrometer at room temperature and at 40 K in a cylindrical mode resonator (Bruker ER4103 TM). A He gas flow cryostat (Oxford ESR 900) was used for sample cooling. A calibrated sputtered amorphous silicon sample with a spin number of 2×10^{15} and g-value of 2.00565 was used as a secondary standard for magnetic field calibration and evaluation of g-values. For these measurements, the sample has been prepared dissolving the nanoparticles into acetone because it evaporates quickly. The measurement parameters are as follows; Microwave frequency is approximately 9.3 GHz, Microwave power is 0.2mW and Modulation frequency is 100 kHz. The result is shown in Fig. 3.8 where a peak it is clearly observed at $g=2.00336$ (g is the Landé g-factor). This value is very near to the g value of a free electron ($g=2.00233$). Hence, ESR

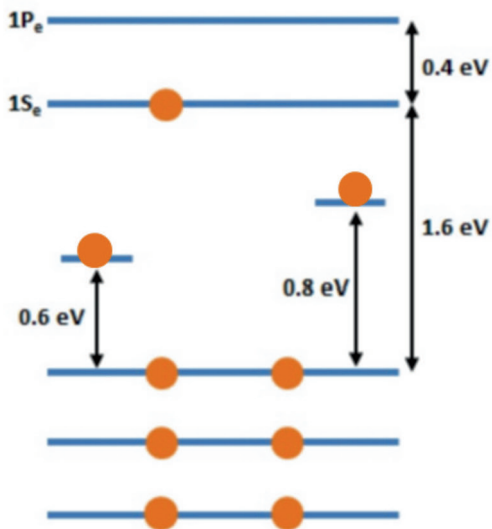


Figure 3.7: Band energy diagram of SnS nanoparticles. The transition at 1.6 eV corresponds to the band gap transition. The 0.4 eV is the range of energy of the transition which occurs between the level $1S_e$ and $1P_e$ due to the dopant electron. The two transitions at 0.6 and 0.8 eV correspond to the transition between the valence band of the nanoparticle and two trap states.

measurement confirms the presence of a free electron placed at the level $1S_e$.

Thus far, direct experimental identification of the dopant species or their location has been very hard. The doping can be due to different mechanisms. A possible doping mechanism involves the sodium sulfide (Na_2S) species used as precursor for S in the synthesis of the nanoparticles. A Na^+ ion can attach to the QD and induce a free electron at the Lowest Unoccupied Quantum-Confined Orbital (LUQCO). In this process the sulfur is thought to act as an anion or radical anion and delivers the electron [107]. The sodium in this scheme stays ionized and is never metallic. This mechanism does not contradict the “self-purification” nature of quantum dots. Transfer of an electron from sodium biphenyl to the (LUQCO) of colloidal semiconductors has earlier been reported [106]. The exact reaction is not yet known and the source of the free electron to facilitate this process needs to be explored. Also for this mechanism to exist, it is essential that the QD surface is properly passivated, in which the TOPO might have helped. Electron transfer is specifically considered here to explain the free electron nature as observed in ESR data, but free electrons can also be created in the SnS by vacancy doping. "Defect" doping, or “vacancies”, which are reported for bulk SnS, are among the possibilities, however, the thermodynamic viability of the formation of these defects in a quantum dot has to be answered. A further analysis by solid state defect chemistry could help to understand better this doping phenomenon.

The other two transitions at 0.6 and 0.8 eV can be due to deep trap states. The study of these two peaks is still under investigation.

Scanning tunneling spectroscopy (STS) was used to study the local electronic properties of single, isolated SnS nanocrystal as a function of their size. For that, scanning tunneling microscopy (STM), $I(V)$ and dI/dV tunneling conductance spectra (the latter being proportional to the density of states) were measured in an ultra-high-vacuum variable temperature STM Omicron system using a tungsten tip.

To obtain complete topography and electrical behavior information on the SnS nanoparticles, STM and STS in an ultra-high-vacuum was performed. Many nanoparticles with two different sizes were detected. Fig. 3.9 shows the STM image of a few SnS nanocrystals acquired at a bias voltage of 2V applied to the sample and a current set point of 15 pA. In STM measurements nanoparticles with size of 2 nm and 4 nm has been found. In Fig. 3.9 the STM image of two of these nanoparticles with size of 2 nm (a) and 4 nm(b) and their z-profile (c) are shown.

Many I-V measurements were carried out on nanoparticles with size of 2 nm and 4 nm and were averaged. The I-V spectra were found to be different for nanoparticles with different sizes. In figures 3.10a and 3.10c the I-V spectra for nanoparticles with 2 and 4 nm size are respectively shown and in Fig. 3.10b

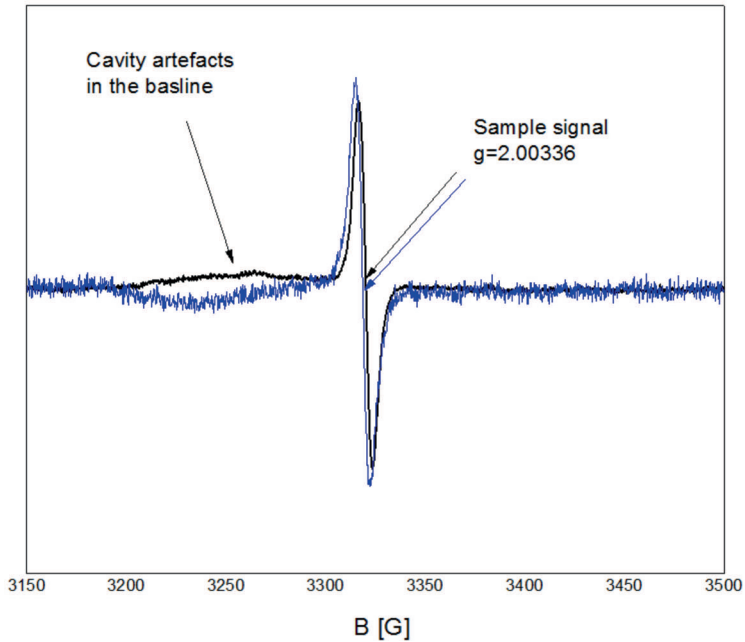


Figure 3.8: Electron Spin Resonance on SnS nanoparticles.

the dI/dV - V plot for the nanoparticle of 2 nm is reported. These data reveal that the 2 nm size SnS nanoparticles behave as a quantum dot, exhibiting a band gap, as well as revealing quantized energy levels. In contrast, I/V measurements carried out on the nanoparticles with size of 4 nm shows no band gap, a behavior similar to metals.

There are two possible reasons for the difference in doping behavior seen between the two particles. One possible reason can be that the 2 nm nanoparticles, having a smaller surface, expel the dopant atoms by self-purification more easily than the 4 nm nanoparticles. The STS measurements carried on the 4 nm nanoparticles seem to confirm the doping hypothesis. There is no band gap because a free electron is placed in the LUQCO and no transitions are possible; on the other hand the higher energy levels are very close each other. This could explain why the 4 nm nanoparticles behave similar to metals.

3.5 Thin Film of Quantum Dot

To make electronic devices, QDs have to be coated on a substrate as thin films. For this reason it is important to verify that during this process quantum dots do not lose their properties. It is also necessary to optimize the process by

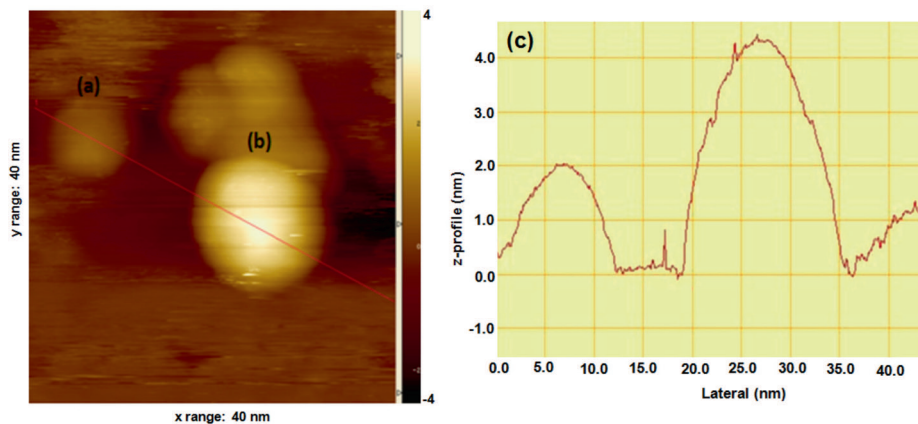


Figure 3.9: Images of SnS nanoparticles of (a) with 2 nm and (b) 4 nm size acquired by STM, (c) The sizes can more reliably be determined from the z-profile.

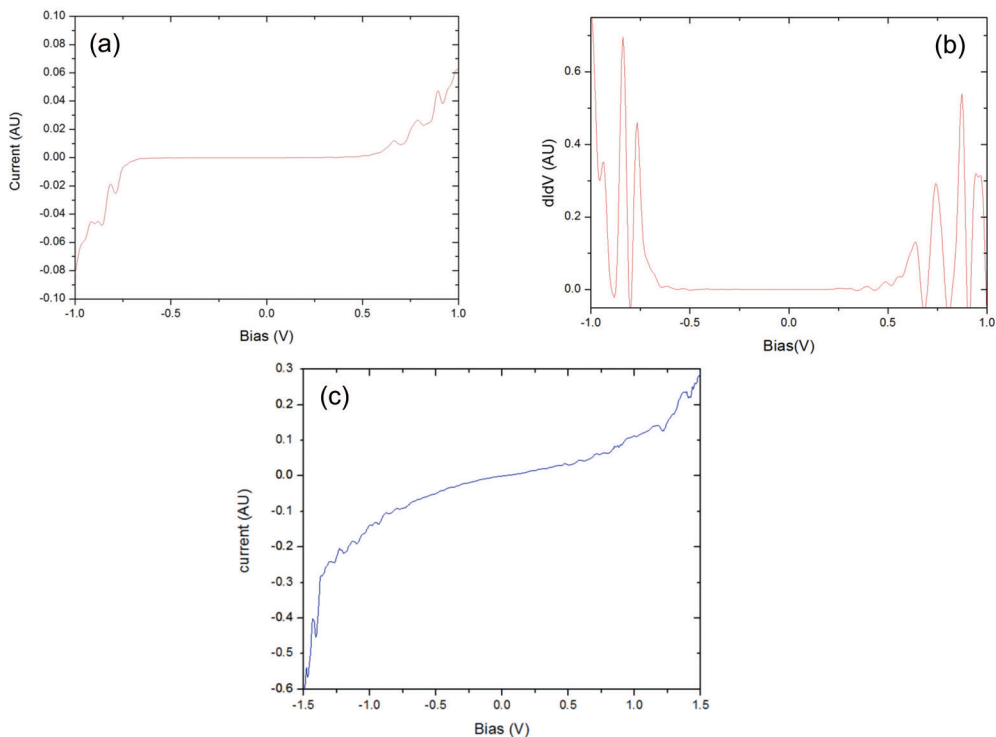


Figure 3.10: (a) I/V and (b) dI/dV measurements acquired by STS on SnS nanoparticles with 2 nm size and (c) I/V measurements on SnS nanoparticles with 4 nm size.

finding the deposition parameters that deliver the best device performance.

In this work thin film of QDs were deposited on glass by spray pyrolysis [58], the technique described in chapter 2. The morphology of the film was investigated by AFM (Fig. 3.11) and SEM (Fig. 3.12). For AFM and SEM measurements the film was sprayed on glass substrate. An image, $1\mu\text{m} \times 1\mu\text{m}$, of thin film made of SnS nanoparticles was acquired by AFM. AFM image of this material showed that the film made with SnS nanoparticles is rough and there is a wide range in the heights of the surface features (Fig. 3.11b) and it shows the presence of deep holes. The roughness analysis has been carried out with the WSxM software. The height of each point of the AFM image has been measured and reported in a histogram, shown in Fig. 3.11a, where in the x-axis is reported the value of the height, called topography, and in the y-axis the number of event, i.e., how many times that value of height has been counted. This roughness analysis gives a more complete information because it takes into account all the surfaces and not only a small part. The roughness analysis confirms the high roughness of the film. Indeed observing the width of the distribution one can see that the roughness values are in the range of 200 nm (data between 700 nm and 900 nm). This result is more explicit in the z-profile reported in Fig. 3.11c corresponding to the white line shown in Fig. 3.11b. This AFM measurement showed that the films made by spraying SnS nanoparticles have a roughness in the order of few hundred nanometers and contain deep trenches to the depth of even $1\mu\text{m}$.

The same result is confirmed by SEM measurement (Fig. 3.12) which shows a rough film with agglomeration and holes. AFM and SEM images showed that spray pyrolysis does not allow to form even uniform standard thin film because it is hard to have a good control of the deposition. The film made by spraying is not a monolayer of nanoparticles but it seems that the nanoparticles stick together. However, an advantage of the spray technique is that it is fast and cheap. It is nevertheless important to verify how the roughness influences the performance of the devices and if the quantum effect is still maintained. Other important parameters such as band gap, activation energy and conductivity will be investigated in the next chapter and compared with SnS/ In_2S_3 core-shell nanoparticles.

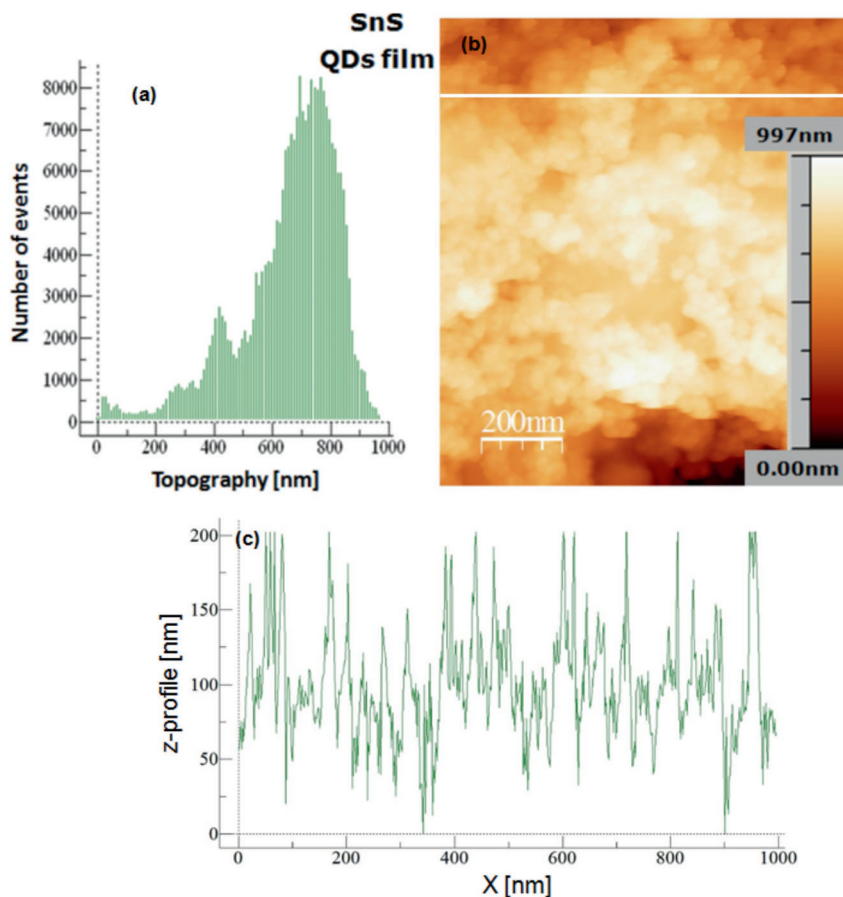


Figure 3.11: AFM roughness analysis and morphology of thin film of QDs. (a) For the roughness analysis the height of each point of AFM image has been measured: in the x-axis is reported the height value, in the y-axis the number of events. (b) morphology image and (c) z-profile correspondent to the white line.

3.6 Conclusion

In this chapter a new facile synthesis of SnS QDs, with a size of ~ 4 nm, which is less than the Bohr radius, has been described. This synthesis is carried out at room temperature and by colloidal route; this makes the processing fast and cheap for making the quantum dots. The structural investigations showed the presence of crystalline SnS quantum dots. The optical absorption, studied using UV/VIS spectroscopy and PDS, showed that the band gap of the QDs 1.6 eV, a value in accordance with theoretical expectations, confirmed the

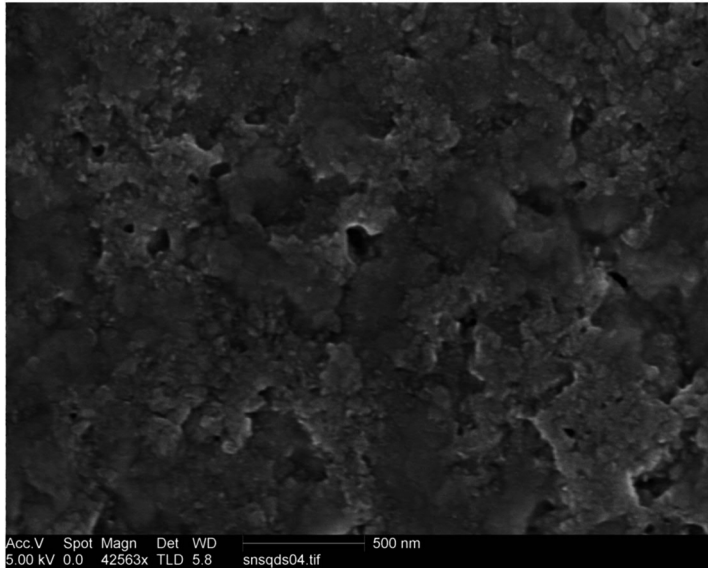


Figure 3.12: SEM morphology of thin film of SnS QDs.

quantum confinement. Furthermore, the absorption spectrum gave evidence of a high absorption in the VIS/NIR range. This can be useful for photovoltaic applications if we also consider the low toxicity of the materials. The absence of the exciton peak together with the presence of an infrared peak at 0.4 eV suggest that the nanoparticles are doped. This 0.4 eV peak was attributed to the $1S_e - 1P_e$ transition due to the presence of an extra electron in the conduction band. ESR measurements confirmed the presence of free electrons. More information about the electrical properties was obtained using STS, which showed the size dependence of doping behavior. This study has shown the possibility of doping SnS nanoparticles, paving the way for their use in optoelectronic applications, such as solar cells. Furthermore, thin film of SnS QDs has been studied in order to verify whether the properties of the quantum dots are still maintained within the deposited film. The morphology of the film surface acquired by AFM and SEM suggests that there is an agglomeration of particles.

Chapter 4

Synthesis and characterization of SnS/In₂S₃ core-shell nanoparticles

In this chapter a new type of core-shell nanoparticles is presented. The core is made of tin-sulfide (SnS) via the colloidal route. The shell, made of indium-sulfide (In₂S₃), is grown by chemical bath deposition. These nanoparticles have been characterized using transmission electron microscopy to study their size and shape. High resolution TEM allowed the structure to be determined of the core and the shell. The optical absorption was studied using UV/VIS spectroscopy, changing the deposition time and temperature. Moreover, the influence of these parameters on the band gap was investigated.

Afterwards, the properties of thin films of SnS/In₂S₃ core-shell nanoparticle were studied and compared with SnS and In₂S₃ thin films. The SnS/In₂S₃ core-shell nanoparticles were deposited by spraying on glass and the influence of the thickness on the band gap and on the surface morphology was studied.

For solar cell applications photosensitivity is very important. For this reason dark and photoconductivity measurements have been carried out. The core-shell nanoparticles have shown an excellent photosensitivity, confirming their great potential for photovoltaic applications.

4.1 Introduction

In the previous chapter we discussed the synthesis of semiconductor quantum dots and the important role that trioctylphosphine oxide (TOPO) plays in controlling the size of nanoparticles and passivating their surface. Nevertheless, incomplete passivation with ligands leads to trap states at the surface [108] which reduce the fluorescence quantum yield (Q.Y.), due to increased non-radiative electron-hole recombination. Thus, it is important to avoid this by maintaining the maximum sterically allowed surface coverage. A better approach is to replace the ligands with a shell, made of another semiconductor material, creating a core-shell structure. It has been shown that a core-shell structure exhibits good stability and less photo-degradation. Moreover, when the core is conformally coated by a shell the density of dangling bonds at the surface that usually acts as trap states is reduced. The first research reported in the literature was on CdSe/ZnS nanoparticles by Hines and Guyot-Sionnest [109]. They covered CdSe cores with 1-2 monolayers of ZnS. Moreover, they showed that addition of a ZnS shell improves the fluorescent quantum yield of the particles, achieving a Q.Y. of 50%. In the second half of the 1990s many articles were published on core-shell nanoparticles [110, 111]. The structure of core-shell nanoparticles can be divided in two groups depending on the band alignment [112], as summarized in Fig. 4.1.

The nanoparticles belonging to the **type I** system have the band gap of the shell larger than the band gap of the core (Fig. 4.1a), and both conduction and valence band offsets are positive. In this way both the electrons and the holes are confined within the core. There exists also another type called **reverse type I** where the band gap of the shell is smaller than that of the core (Fig. 4.1b).

In nanoparticles of **type II** the offsets at conduction and valence band have opposite signs (Fig. 4.1c and d). Electrons and holes are spatially separated between core and shell. The most studied nanoparticles are CdS/HgS [113], CdS/CdSe [114] and ZnSe/CdSe [115] of type I, CdTe/CdSe and CdSe/ZnTe of type II.

It is important to choose the right material to make the shell in order to get a stable structure with suitable optical and electronic properties. Of course, it is crucial to have the proper band alignment. It is desirable that the shell and the core materials have the same structure in order to have a small lattice mismatch.

Otherwise, the structure could be affected by strain or stress, which leads to the creation of defects that can act as trap states and thus can significantly reduce the quality of the core-shell nanoparticles.

Another critical parameter is the shell thickness: it is necessary to have a

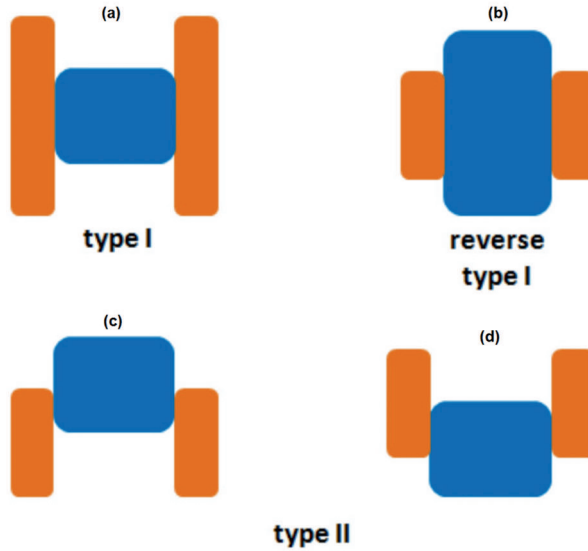


Figure 4.1: Representation of the energy level alignment in different types of core-shell configurations: (a) scheme of core-shell structure type I and (b) reverse type I. (c) and (d) core-shell structures type II. The upper edge of the rectangles represents the conduction band, the lowest edge the valence band. The rectangle in the center corresponds to the core, the two external rectangles correspond to the shell.

good control of the thickness because if the shell is too thin the nanoparticles are not well passivated, whereas if it is too thick the optical properties deteriorate because of mismatch, such as strain and stress, more defects are created with increasing shell thickness [116]. Usually the core-shell nanoparticles are synthesized in two steps: first the core is synthesized chemically, and then, after a purification step, the shell is coated onto the cores. In this chapter the synthesis and characterization of SnS/In₂S₃ core/shell nanoparticles are described.

4.2 Synthesis and characterization

Indium sulfide (In₂S₃) has been chosen as material for the shell of our SnS cores. In₂S₃ is a semiconductor belonging to III-VI group. In recent years, III-VI materials have received increasing attention, and they have already been used for many applications such as optoelectronic, photovoltaic [117] and photoelectrochemical solar cells [118]. These materials have gained interest for solar cells applications because of their stability [119], transparency, high photoconductivity [120], and their band gap, which is 2 - 2.3 eV [121] and 2.8 eV [122].

An important investigation has been carried out on the deposition and characterization of In₂S₃, mainly focused on the replacement of the toxic CdS layer, used as buffer layer in CuInS₂ solar cells [123]. Several groups report on the growth of In₂S₃ thin films by means of various techniques such as chemical bath deposition [124], spray pyrolysis [125], chemical vapor deposition [126], atomic layer epitaxy [127], atomic layer deposition [128], reactive evaporation [129], thermal evaporation [130,131] and modulated flux deposition [132]. In₂S₃ can exist in many different phases depending on the type of deposition technique and conditions [133].

In this work, SnS/In₂S₃ core/shell nanoparticles are synthesized using the Chemical Bath Deposition (CBD) technique, whereby an ethanol dispersion of previously synthesized TOPO capped SnS NPs is immersed in the CBD bath for deposition of the In₂S₃ layer. Afterwards, the coated nanoparticles are separated by centrifugation and washed in ethanol. The bath composition was made of InCl₃, thioacetamide and acetic acid in water.

At first, the size and the shape of the nanoparticles were checked using a Transmission Electron Microscopy (TEM). The TEM samples were prepared by depositing the nanoparticles on a carbon grid by drop casting. Fig. 4.2 shows the TEM image of SnS/In₂S₃ core-shell NPs.

It can be seen that there are nanoparticles with size in the range of 5-15 nm, and other bigger particles, around 20 nm, where two or more darker dots are visible within the particle structure. This leads us to think that these particles have two or more cores. However, from these TEM images it is not possible to discern clearly the core-shell structure.

To obtain the required resolution, the HRTEM Tecnai F20ST/STEM (200 kV) was used for imaging. For these measurements the samples have been prepared in a different way than for TEM. The nanoparticles were deposited on a glass substrate by spray pyrolysis and afterwards the samples were cut to study their cross section. TEM samples were prepared by gluing a Si crystal from a wafer on the film side of the material, then cutting a slice with a thickness of 0.5 - 1 mm with a diamond saw, grinding and polishing the slice down mechanically to a thickness of ~ 10 μm, then placing it on a Cu slot grid and thinning it to electron transparency using a Gatan PIPS 691 ion mill, using Ar. The HRTEM image is reported in Fig. 4.3. Now the core-shell structure of the nanoparticles is evident. It is possible to distinguish two different nanoparticle structures. On the left side of the picture a cluster of two nanoparticles is visible: a smaller and larger one. It is possible to distinguish two core particles surrounded by a shared shell. On the right side of the image a single nanoparticle is observed. The core of this nanoparticle is darker and shows clear lattice fringes, while the shell, which covers the core completely, appears to have an amorphous structure. The size of this nanoparticle including the

shell is slightly larger than 10 nm.

The chemical composition has been investigated by means of Energy-dispersive X-ray spectroscopy (EDX). The EDX spectrum is reported in Fig. 4.4. This measurement confirmed the presence of the three expected elements: indium, sulfur and tin. Small quantities of other elements have been detected: chlorine from the InCl₃ used in the bath, copper and carbon due to the lacey copper grid used for TEM-EDX measurements.

The structure was first characterized by XRD (Fig. 4.5), which confirmed the presence of ZB SnS peaks, but In₂S₃ peaks are not clear, this can be due to the amorphous structure of the shell.

The deposition time and temperature are two critical parameters for the deposition of the shell during the CBD synthesis. The process parameters play a crucial role in the thickness of the shell and thus also in the optical absorption of the core-shell structure. The effect of the deposition time and temperature were studied (Fig. 4.6). In the two graphs the red line corresponds to the absorption spectrum of ethanol used as a solvent to disperse the nanoparticles and acquired as background. This was necessary because, in this case, a single beam spectrometer was used and hence the background was not subtracted automatically. In Fig. 4.6b the influence of the deposition temperature is shown. Fig. 4.6a shows the effect of CBD duration for the deposition at 70°C, and the difference between the absorption of SnS and SnS/In₂S₃ nanoparticles is reported. From Fig. 4.6a the effect of the shell on the band gap is clearly visible. The band gap of a core-shell particle is larger than for the bare SnS quantum dots, as expected. The band gap is monitored by the shift of absorption edge in Fig. 4.6a. Even 5 minutes of CBD change the band gap drastically. Fig. 4.6a also clearly shows the possibility to fine-tuning the band gap by changing the thickness of the shell. The band gap increases monotonically with increasing deposition time.

4.3 SnS/In₂S₃ core-shell NPs thin film

Layer-by-layer self-assembly deposition using the spraying technique was employed to make thin films of SnS/In₂S₃ NPs. It is necessary to find the best solvent for the spray deposition of the nanoparticles on the substrate. The most common solvents were tested to find the most suitable one for this type of nanoparticles. The stability of nanoparticles at different solvent temperatures is reported in Table 4.1. For some of the nanoparticles there was a clear precipitation in the solution after few days. Precipitation was also identified when successive measurements of optical absorption of the solution in a cuvette

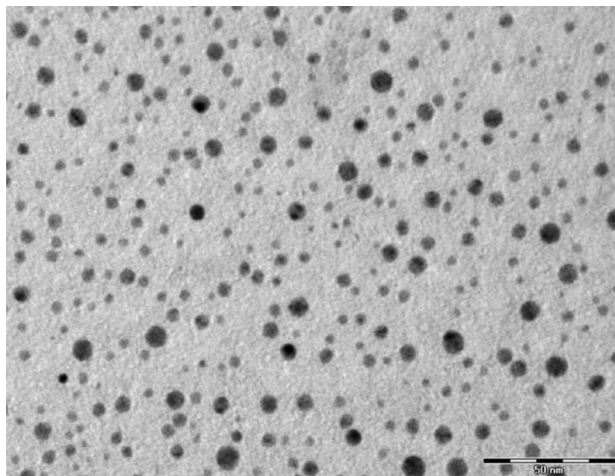


Figure 4.2: TEM images of SnS/In₂S₃ core-shell NPs with scale bar of 50 nm.

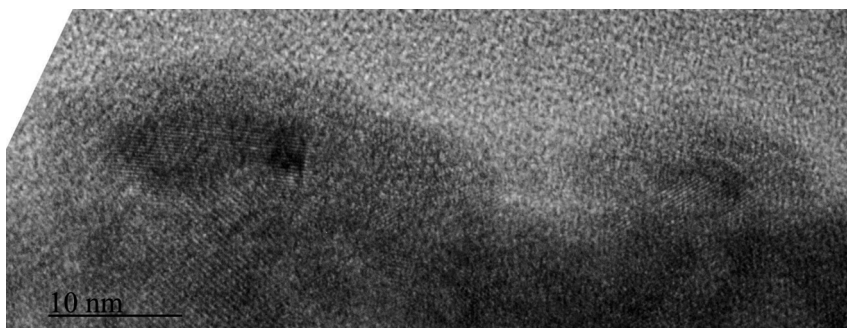


Figure 4.3: HRTEM image of SnS/In₂S₃ core-shell nanoparticles

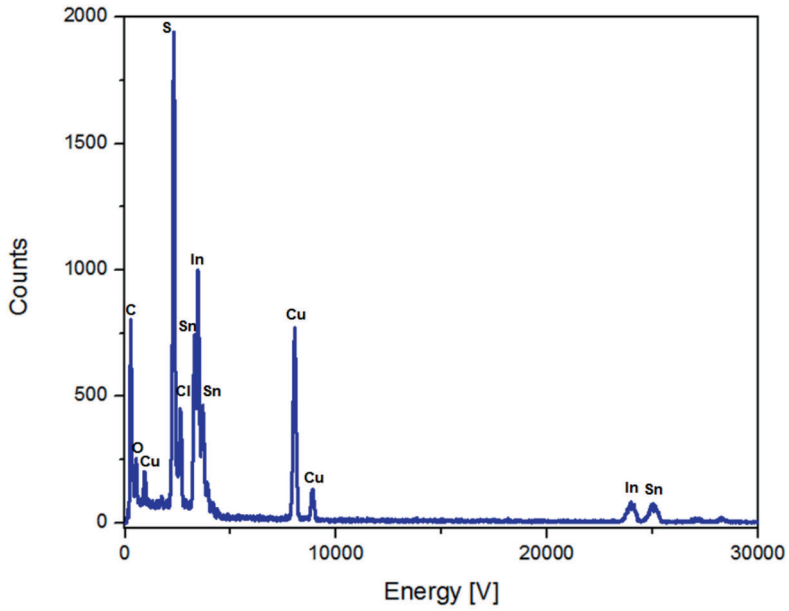


Figure 4.4: EDX spectrum acquired on $\text{SnS}/\text{In}_2\text{S}_3$ core-shell NPs deposited on a lacey carbon grid.

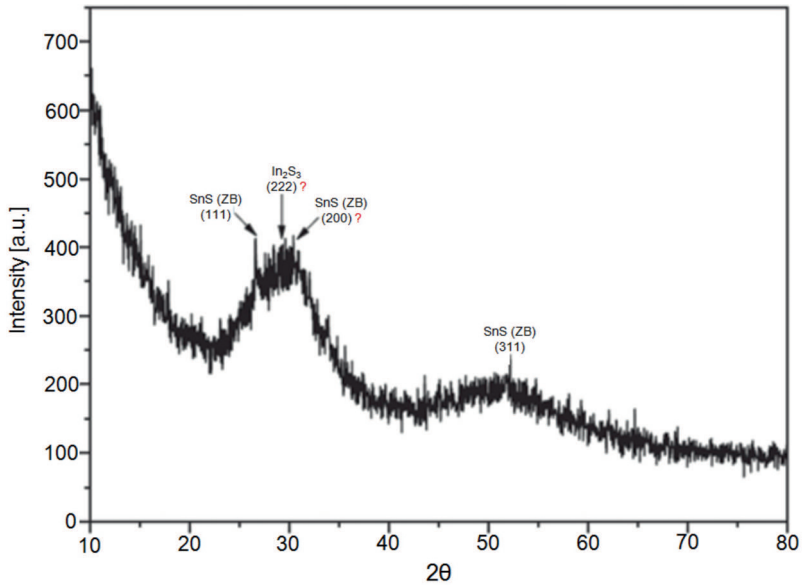


Figure 4.5: XRD spectrum of $\text{SnS}/\text{In}_2\text{S}_3$ core-shell particles.

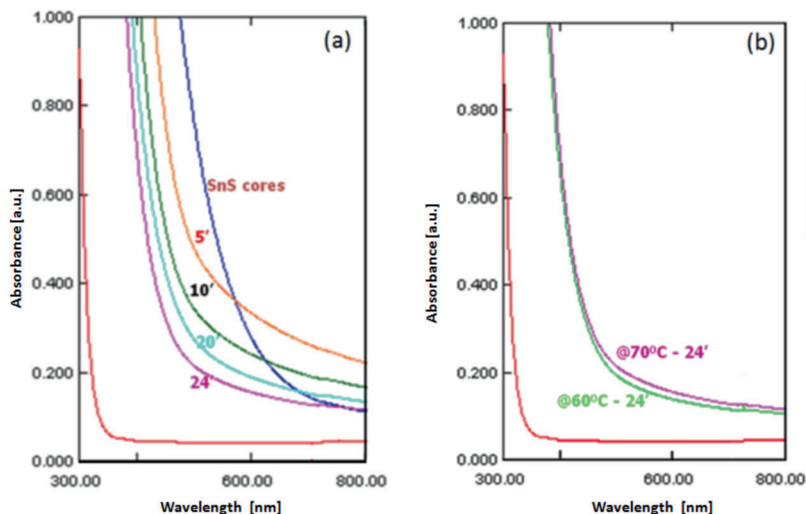


Figure 4.6: absorption spectrum of SnS and SnS/In₂S₃ core-shell NPs (a) at different deposition times and (b) at two different deposition temperatures. The red line corresponds to the background spectrum, the absorption spectrum of ethanol.

showed drift. The samples were investigated by other techniques, such as TEM, to verify their stability. Taking the information about the stability and the physical properties of the solvent into consideration, acetone-ethanol mixtures were used for spray deposition mainly due to its high volatility. First, the stability of the nanoparticles in the acetone during the spray process was observed. For the spray deposition of SnS and SnS/In₂S₃, the core-shell nanoparticles are dispersed in acetone-ethanol mixture and the solution is kept in a bottle with a spraying nozzle, which is connected to nitrogen. Once the nitrogen is turned on, the solution is sprayed on the substrate placed on a hotplate at a temperature of 80 °C.

Multiple numbers of spray depositions (2, 3, 5 and 8) of films of SnS/In₂S₃ core-shell were investigated while In₂S₃ and SnS thin films were used as reference, deposited also using the spray technique. One single spray can have a duration of few seconds, depending on the area of the substrate. During one spray and the following one there are 20 seconds of waiting time. During these 20 seconds the solvent evaporates and the film is formed. By increasing the number of sprays, the thickness of the layer increases.

Many different techniques were used to study the thin films. The morphology of the films was analyzed using two techniques, Atomic Force Microscopy (AFM) and Scanning Electron Microscope (SEM). AFM topography images are reported on the right side of each image in Fig. 4.7 with the correspondent roughness analysis shown on the left side. It is disappointing that even

the In₂S₃ and SnS thin films, which were expected to be smooth, showed high roughness with average feature heights of ~300 nm and ~500 nm respectively. The SnS QD films and the SnS/In₂S₃ core/shell sprayed layers were very rough. The roughness measured, however, is much higher than that expected for typical quantum dot sizes. A possible cause is that the nanoparticles stick together as the solvent evaporates. SEM measurements have been carried out on the same samples, and they confirmed the very rough features, as shown in Fig. 4.8. The In₂S₃ film and the SnS/In₂S₃ core/shell layer made with two sprays, however, showed smoother surfaces in SEM than in AFM.

The optical band gaps of the layers were obtained from the optical absorption plot obtained from reflection/transmission measurements. The absorption coefficient (α) was calculated using the relation

$$\alpha = -\frac{1}{d} \ln \frac{T}{(1-R)^2} \quad (4.1)$$

where T and R are the reflectance and transmittance values and d is the thickness. Fig. 4.9 shows the absorption coefficient versus energy plots of the samples. None of the samples showed fringes in the optical absorption, confirming the rough surface nature of the films. Because of the roughness of the surfaces of these samples it was very difficult to measure the thickness. The thickness used in the previous formula was obtained by means of the average of different values of measured thickness acquired using the Dektak thickness profiler setup. Because of the roughness of the films, it is hard to get the accurate absorption coefficient value. Nevertheless, Figure 4.9 is useful for having qualitative information about the behavior of the changes in the accumulated layer with the number of sprays. In Figure 4.9 one can distinguish two groups. The layers made with 2 and 3 sprays have a behavior similar to a In₂S₃ thin film, whereas the layers with 5 or 8 sprays are closer to the SnS thin film and SnS QD thin film. The change from the first group to the second group is not continuous: there seems to be a kind of gap between the two groups. It is also important to note that despite the systematic error in optical absorption due to the roughness, the SnS QD thin film shows a higher band gap than the SnS bulk film, confirming that there is quantum confinement which is also valid after the deposition.

For solar cell applications it is extremely important to study the dark conductivity and photoconductivity in order to understand the charge transport and the photosensitivity (photo conductivity/dark conductivity) of the materials. The dark conductivity was measured using a planar configuration of coplanar silver contacts on the films. From the temperature dependence of the dark conductivity, the activation energy is obtained from the slope of an Arrhenius plot. The photoconductivity of the samples was obtained under AM1.5

Solvents	Temperature [°C]			
	25	40	60	80
Ethanol	yes	no	no	no
Isopropyl alcohol	yes	no	no	no
Acetone	yes	yes	yes	yes
Ethylene glycol	yes	yes	yes	yes
N-Hexane	yes	yes		

Table 4.1: Stability of SnS nanoparticles in different solvents. The nanoparticles are stable when they are well dispersed in the solvent.

100 mW/cm² illumination of a solar simulator. Table 4.2 lists the activation energy, dark conductivity, and photoconductivity of the samples. The absolute values of dark and photoconductivity values carry error due to the error in the estimated thickness, as mentioned above, the activation energy and photosensitivity are reliable quantities. These SnS QD and SnS/In₂S₃ core/shell coated layers on glass showed excellent photosensitivities; the value around 10⁵ for the core-shell film made with 8 sprays suggests low defective material, which may be speculated to be due to excellent surface passivation of SnS cores by the shell. This photoconductive property indicates that these materials will deliver extra photocurrent when added to a standard CIS solar cell. The activation energies of all the samples, around 0.5 eV, indicate doped behavior also for SnS QD film, confirming the result that was already discussed in Chapter 3 about the doping of these nanoparticles.

4.4 SnS QDs embedded in In₂S₃ thin film

Before characterizing the SnS QDs embedded semiconductor (In₂S₃) matrix, it was important to optimize the In₂S₃ layer. For this, the process temperature dependence of the characteristics of the In₂S₃ semiconductor layers were evaluated. The In₂S₃ thin films were deposited at four different temperatures: 200°C, 250°C, 300°C, 350°C, and 400°C by spraying technique. The morphology of the layers has been characterized by SEM, as reported in Fig. 4.10. It was found that the samples made at temperatures lower than 300°C were tissue-like, whereas at process temperatures above 350°C, the samples showed a rough character. The In₂S₃ layers made 300°C and 350°C are smooth and compact.

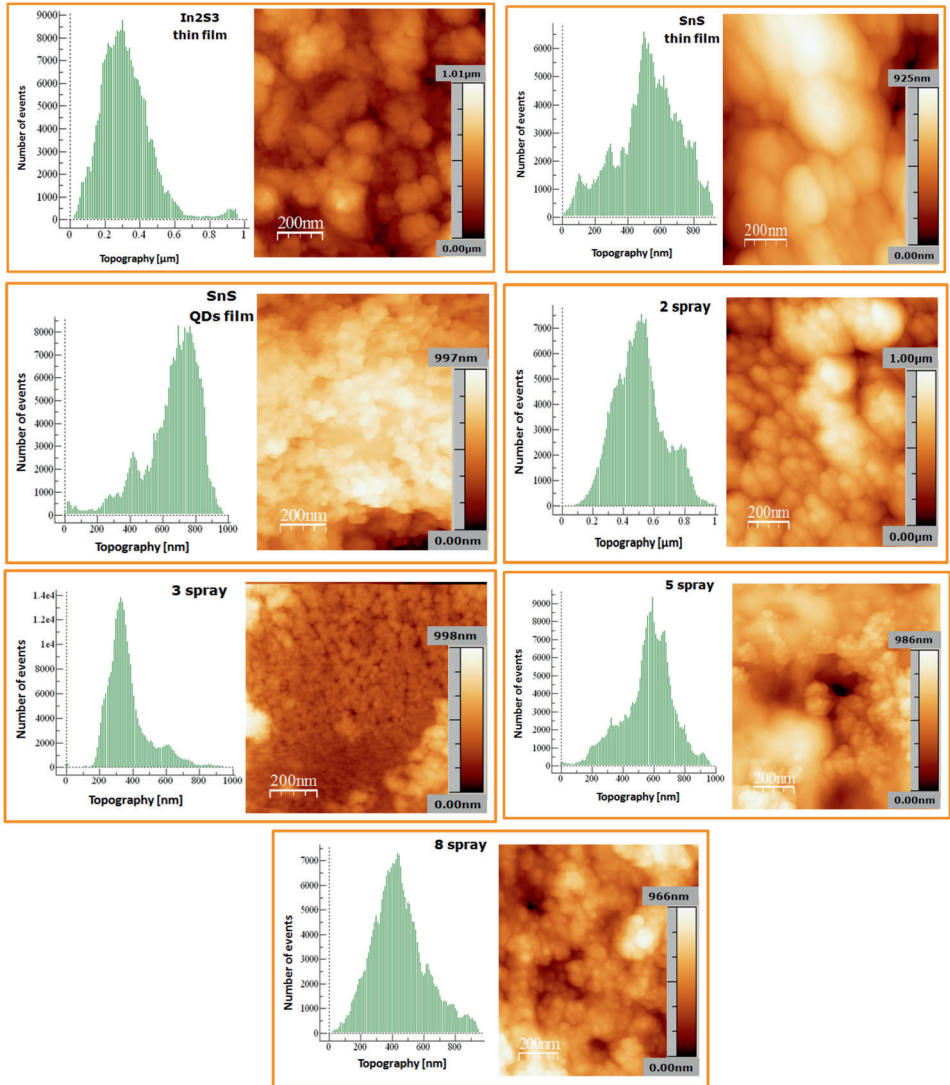


Figure 4.7: AFM images of In_2S_3 and SnS thin films used as reference and SnS/ In_2S_3 core-shell nanoparticles films made with different numbers of spray applications (2,3,5 and 8) on glass.

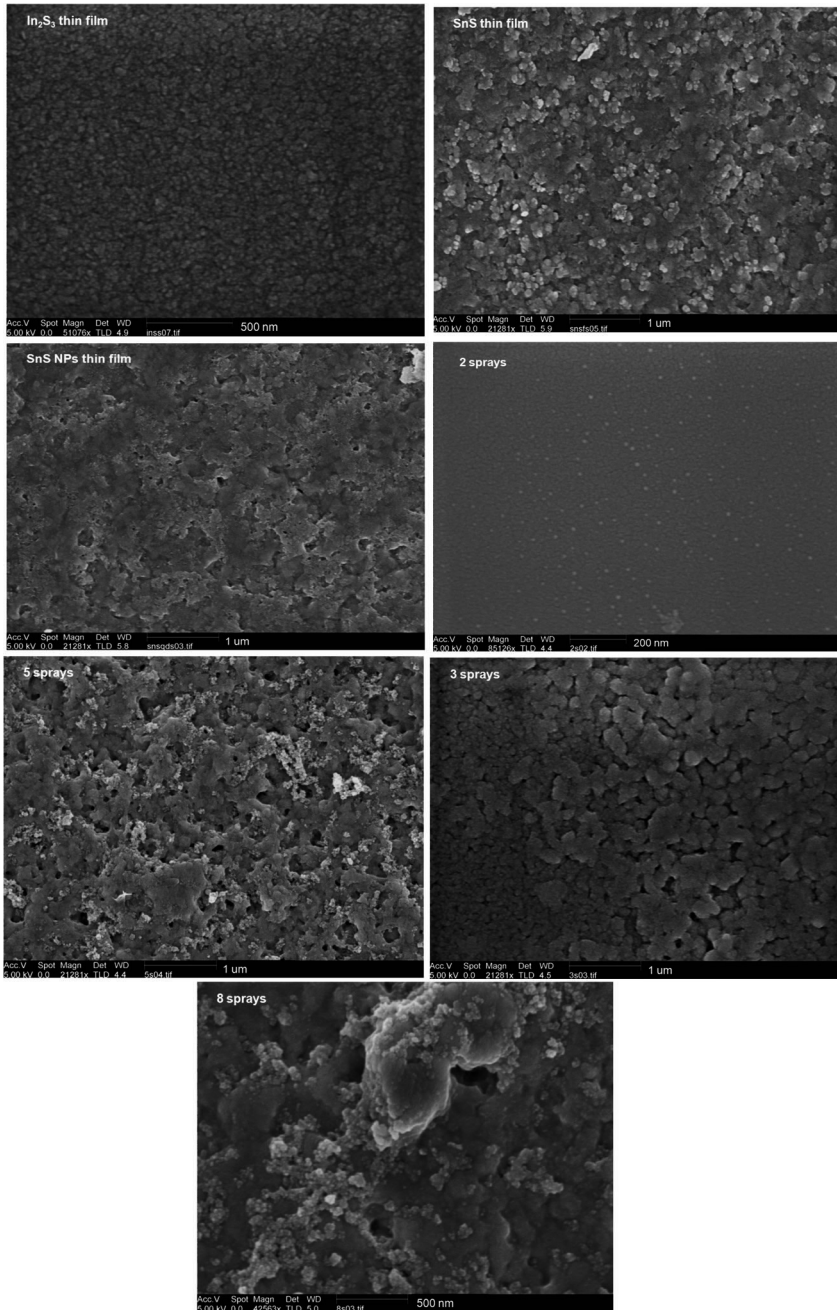


Figure 4.8: SEM images of In₂S₃ and SnS thin films used as a reference and SnS/In₂S₃ core-shell nanoparticles films deposited with different number of sprays (2, 3, 5 and 8) on glass.

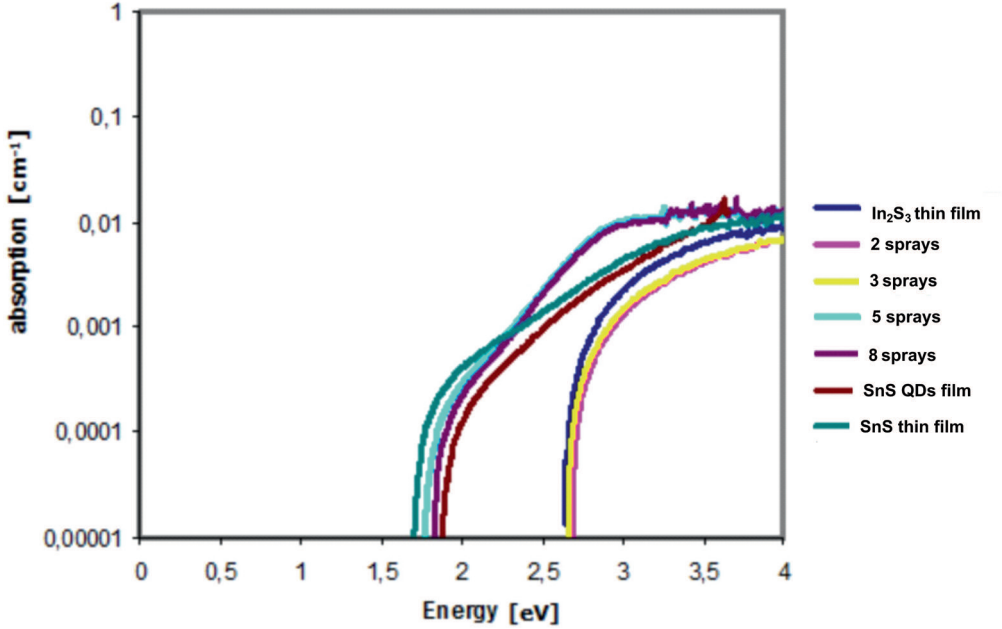


Figure 4.9: Absorption spectra of In₂S₃ and SnS thin films and SnS/In₂S₃ core-shell nanoparticles films made with a different number of sprays (2, 3, 5 and 8) on glass.

Samples	Dark conductivity [$\Omega^{-1}\text{cm}^{-1}$]	Photo-conductivity [$\Omega^{-1}\text{cm}^{-1}$]	Photo-sensitivity	Activation energy [eV]
SnS/In ₂ S ₃ 3 spray	$4.1 \cdot 10^{-12}$	$2.0 \cdot 10^{-4}$	$0.5 \cdot 10^8$	0.61
SnS/In ₂ S ₃ 5 spray	$1.9 \cdot 10^{-5}$	$1.0 \cdot 10^{-2}$	$0.5 \cdot 10^3$	0.24
SnS/In ₂ S ₃ 8 spray	$2.3 \cdot 10^{-7}$	$1.3 \cdot 10^{-2}$	$0.5 \cdot 10^5$	0.24
In ₂ S ₃ thin film	$1.8 \cdot 10^{-14}$	$3.0 \cdot 10^{-4}$	$1.6 \cdot 10^{10}$	0.50
SnS QD thin film	$1.0 \cdot 10^{-7}$	$1.0 \cdot 10^{-3}$	$1.0 \cdot 10^{-4}$	0.44
SnS thin film	$1.0 \cdot 10^{-3}$	$1.0 \cdot 10^{-2}$	$1.0 \cdot 10$	0.19

Table 4.2: Dark- and photo-conductivity, activation energy of In₂S₃ and SnS thin films and SnS/In₂S₃ core-shell films deposited with different number of sprays (2, 3, 5 and 8) on glass.

SnS NPs embedded in In_2S_3 matrix by the spray technique were evaluated with a view to using such a structure as emitter for a CIS cell. The SEM images showed clearly that the NP layer was indeed sandwiched between In_2S_3 layers (see Fig. 4.11). Another observation is that the structure of the In_2S_3 layer above the NP layer looks different from the In_2S_3 layer on which the NP layer was spray deposited. This may be due to the different characteristics of the layers, such as crystalline structure and wetting.

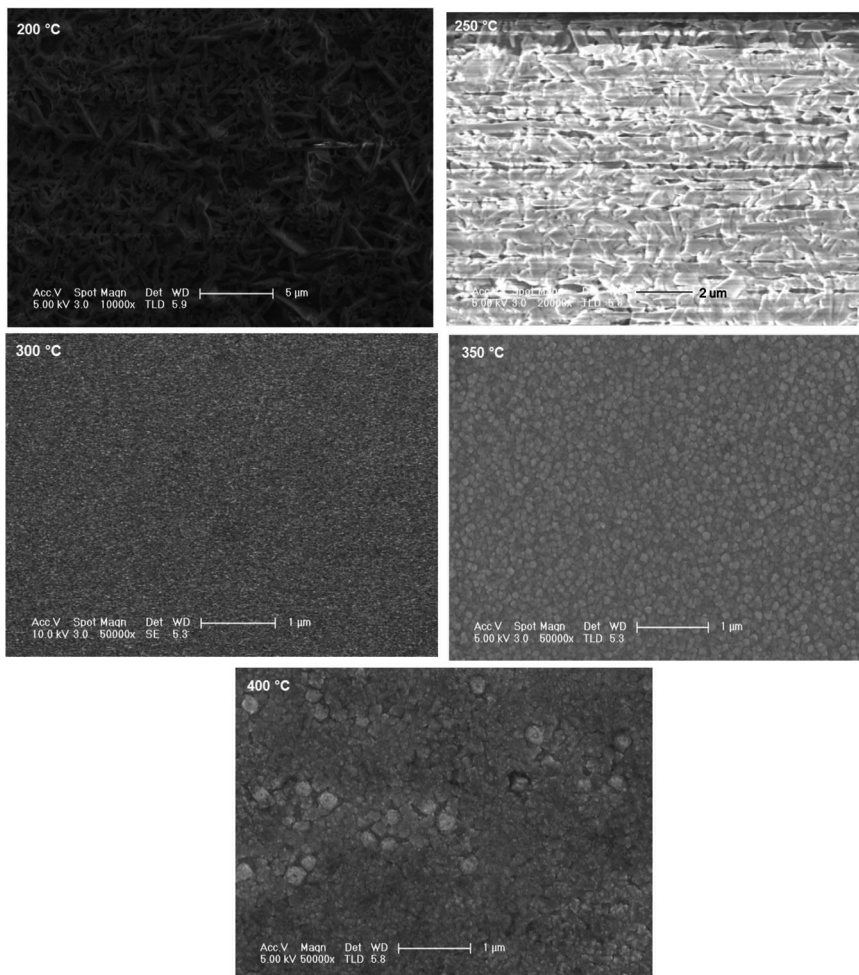


Figure 4.10: SEM images of In_2S_3 thin films deposited at different temperatures.

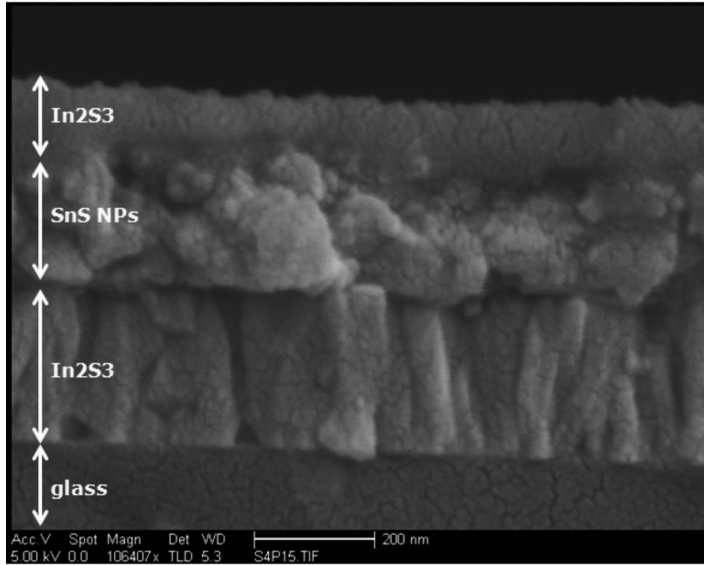


Figure 4.11: Cross section TEM of SnS QDs deposited between two In₂S₃ layers.

4.5 Conclusion

In this chapter a process for coating SnS nanoparticles with a semiconductor shell instead of TOPO ligands has been described. This was done to passivate the surface better and to improve the electrical properties of the nanoparticles. The shell was deposited by the CBD technique. A temperature of 60-70°C during CBD was found to be appropriate since this ensured the formation of a dense coating without damaging the particles, whereas the thickness of the coated shell is fine-tuned by the CBD time. The surface morphology studied using AFM and SEM shows that these films are quite rough. The optical absorption shows the effect of the shell and how the band gap of the SnS/In₂S₃ core shell particles can be varied by increasing shell thickness. The dark- and photo-conductivity measurements confirm that these nanoparticles can be used for solar cell applications. The activation energy values suggested that the nanoparticles films, mainly the SnS QD thin film, can in fact be doped.

SnS QDs embedded between two In₂S₃ layers were investigated. First, In₂S₃ thin films have been deposited at 200, 250, 300, 350 and 400°C to find the optimal deposition temperature. The morphology of these films, studied using SEM, and the structure, studied using XRD, confirm that the best deposition temperature is between 300 and 350°C. With this information In₂S₃/SnS QD/In₂S₃ sandwich structures were created with the aim to implement in a solar cell.

From the cross section of this structure, analyzed by TEM, three layers are easily distinguishable.

Chapter 5

Electrical characterization of nanoparticles by means of Atomic Force Microscope

In this chapter the electrical characterization of SnS and SnS/In₂S₃ core-shell nanoparticles is presented. For this study two different AFM modes are used.

First, the conductivity of the SnS nanoparticles capped with trioctylphosphine oxide (TOPO) and with In₂S₃ shell are analyzed by torsional resonance tunneling AFM. This contactless technique allows carrying out measurements on nanoparticles without destroying them. Using this technique we are able to demonstrate that the particles have conductive properties. Nevertheless, these measurements also showed that the TOPO capping layer may hinder tunneling currents.

For these reasons the same SnS nanoparticles capped with TOPO are also investigated by means of PeakForce AFM. This technique operates similar to the tapping mode but at a frequency below the resonant frequency of the cantilever. This characteristic feature allows the tunnel current to be detected even when ligands are present. The topography map shows single nanoparticles with a size less than 5 nm. In the conductivity map it is possible to discern the same nanoparticles, a clear correlation can be seen with the topography map.

Both techniques allow one to obtain simultaneously topography and conductivity maps. This makes it possible to achieve a complete characterization of individual particles in a single measurement.

5.1 A brief introduction to AFM

In 1982 Binning, Gerber, Rohrer and Wiebel developed an instrument, called scanning tunneling microscope (STM), able to image conducting materials with atomic resolution [70]. The imaging was done by applying a potential V_t between the sample and the tip, while measuring the tunnel current flowing between the tip and the sample. The tunnel current is:

$$I_t(z) = I_0 e^{(-2k_t z)} \quad (5.1)$$

where z is the gap between the tip and the sample, $k_t = \sqrt{(2mf)/\hbar^2}$ where m is the mass of electron, f is the potential barrier, \hbar is the Planks constant, and I_0 is a function of the applied voltage, the density of states in the tip and in the sample. This expression of the tunnel current is valid only when the absolute value of V_t is small compared with the work function.

The tunnel current depends strongly on the distance between the tip and the sample surface and, for this reason, it is very sensitive to the surface topography. In STM the tunnel current is used as feedback, meaning that the tunnel current is kept constant during the measurement, while scanning the tip over the sample surface. It is clear that the STM technique is not suitable for studying non-conducting materials. For this reason, it was necessary to develop a new technique. In 1986 Gerd Binning, Calvin Quate and Christoph Gerber succeeded in this with Atomic Force Microscopy [134]. They used a cantilever made of a gold foil with a fragment of diamond glued on it. The gold foil was thin enough to behave as a spring that could push the diamond onto the sample. The original images are reported in Fig. 5.1, where one can see the working principle of the AFM (a), the diamond functioning as the tip glued onto the cantilever (b) and the first recorded AFM image traces (c).

AFM provides a 2D or 3D profile of the surface at nanoscale by measuring the forces between the tip, which has a dimension of less than 10 nm, and the surface at very short distances, around 0.2 - 10 nm. The AFM tip approaches the sample and records the force between the tip and the surface. The force involved in the measurements depends on the spring constant of the cantilever and on the distance between the tip and the sample. This force can be described simply by Hooke's law: $F = -kx$, where k is the spring constant. When the force generated by the tip-sample interaction force is not balanced by the restoring force of the cantilever, the cantilever bends and the deflection is monitored. The common force range is from nN to μ N in the open air. To control the motion of the probe across the surface a feedback loop and piezoelectronic scanners are used. Another difference with the STM is how the forces are monitored. In AFM the deflection is measured by means of a laser spot reflected from the

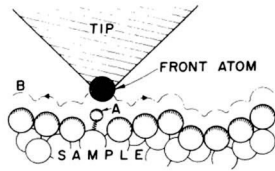


FIG. 1. Description of the principle operation of an STM as well as that of an AFM. The tip follows contour *B*, in one case to keep the tunneling current constant (STM) and in the other to maintain constant force between tip and sample (AFM, sample, and tip either insulating or conducting). The STM itself may probe forces when a periodic force on the adatom *A* varies its position in the gap and modulates the tunneling current in the STM. The force can come from an ac voltage on the tip, or from an externally applied magnetic field for adatoms with a magnetic moment.

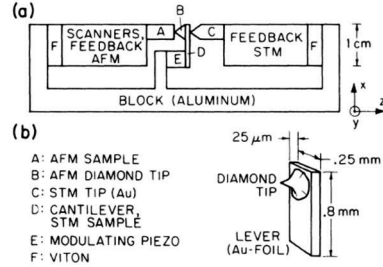


FIG. 2. Experimental setup. The lever is not to scale in (a). Its dimensions are given in (b). The STM and AFM piezoelectric drives are facing each other, sandwiching the diamond tip that is glued to the lever.

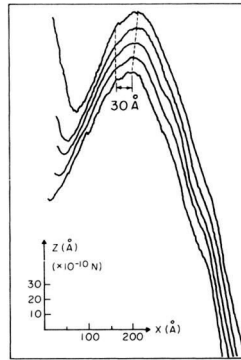


FIG. 3. The AFM traces on a ceramic (Al_2O_3) sample. The vertical scale translates to a force between sample and tip of 10^{-10} N/Å. For the lower traces the force is near 3×10^{-8} N. The stability of the regulated force is better than 10^{-10} N. The successive traces are displaced by a small drift along the *y* axis.

Figure 5.1: Images from the first AFM paper [134]. Reprinted figures with permission from G.Binnig, and C.F. Quate and C.Gerber, Physical Review Letters, Vol.56, N. 9, pp. 930-933 (1986) Copyright (1986) by the American Physical Society.

cantilever onto a photo-diode. The measured cantilever deflections are used to generate a map of the surface morphology.

5.2 AFM operation mode

The dominant forces at short distance in the AFM are the Van der Waals (VdW) interactions. However, the long-range interactions are important. During the measurements, when the probe comes in proximity of the sample, the tip predominantly experiences repulsive forces. Then, the cantilever bends and it is deflected. As the tip moves further away from the sample the attractive force becomes dominant [135]. In Fig. 5.2 the graph of force as a function of the tip-sample distance is reported [136]. In Fig. 5.2 three regions can be distinguished.

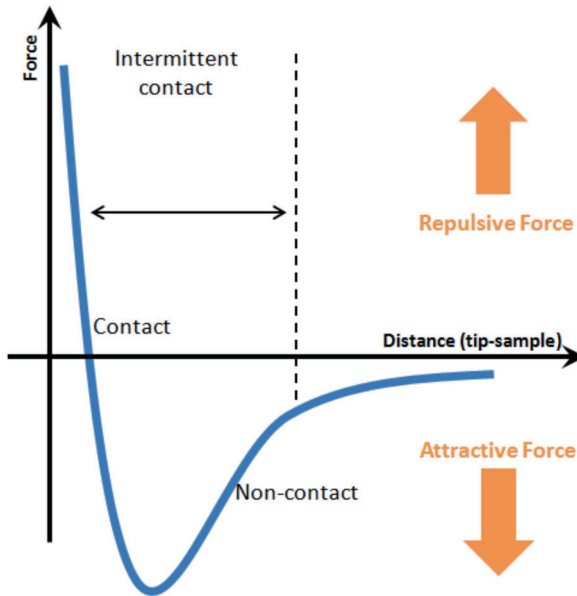


Figure 5.2: Plot of the force between sample and probe as a function of probe-sample separation.

When the tip-sample distance is less than 0.5 nm, the AFM works in “contact mode”. The tip feels the repulsive force. By means of the feedback loops the cantilever deflection is kept constant and therefore the force between the tip and the sample remains constant. The contact mode has some advantages. The measurements are fast, and it is possible to get good quality images of rough samples. However, this mode can damage soft samples.

When the distance is in the range of 0.5 - 2 nm the cantilever oscillates up and down at its resonance frequency, momentarily touching (tapping) the sample. This mode of operation is called tapping mode. An electronic feedback loop controls the oscillation amplitude, keeping it constant, such that the tip-sample interaction (force) is kept constant during the measurement. The main advantage of the tapping mode is that it allows for high resolution of even a soft sample without damaging it. The last mode of operation, called non-contact mode, is when the separation between the tip and the sample is in the range of 0.2 - 10 nm. In this case the forces playing a role are the attractive forces. In this mode the tip does not touch the sample but oscillates above a fluid layer on the surface of the sample that is always present and the tip-surface distance is kept constant because these measurements are performed at room atmosphere. A feedback loop is used to control the changes in the vibrational amplitude due to the attractive forces, and in this way the topography is measured. In

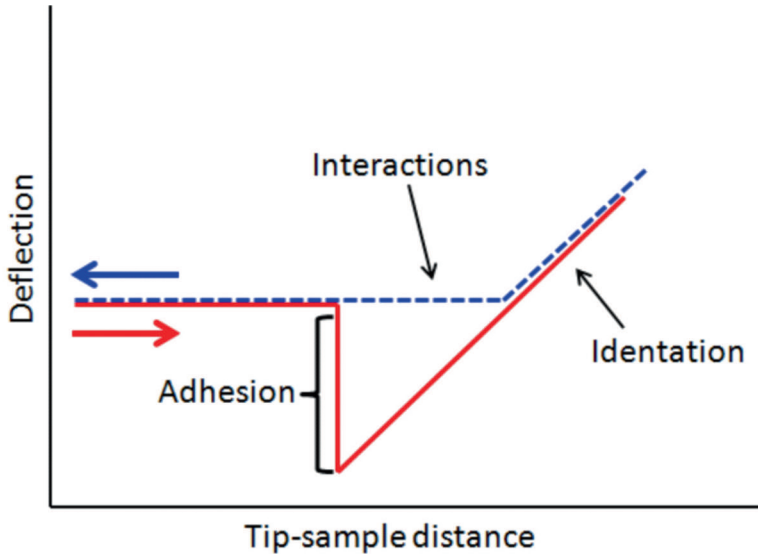


Figure 5.3: Plot of the deflection in function of the tip-sample separation.

this mode the force is very low, but unfortunately the resolution is also low. Moreover, some contaminant layer can disturb the measurements by interfering with the oscillation. Hence, it is better to carry out this type of measurement under ultra-high vacuum conditions in order to improve the performance and the imaging. From the analysis of the force curve it is possible to study the chemical and mechanical properties such as adhesion, elasticity, hardness and ruptured bond lengths. In Fig. 5.3 the deflection as a function of the distance is reported. The slope of the deflection gives information on the hardness of the sample. The adhesion is useful for understanding the interaction between the tip and the sample.

As mentioned above the main advantage of the AFM compared with STM is that it is possible to measure non-conductive samples, allowing a large variety of samples to be investigated, such as plastic, glasses, and biological samples. However, there is one major disadvantage: it is difficult to achieve atomic resolution. This is due to the characteristics of the AFM tip: it is not ideally sharp, and as a result the AFM image does not correspond exactly to the real sample topography. This is called tip convolution and is illustrated in Fig. 5.4. Usually the tip convolution does not influence the height but the lateral resolution [135]. Considering all the pros and cons of the various techniques, AFM was employed to study our samples of unknown conductivity spread on glass or wafer substrates.

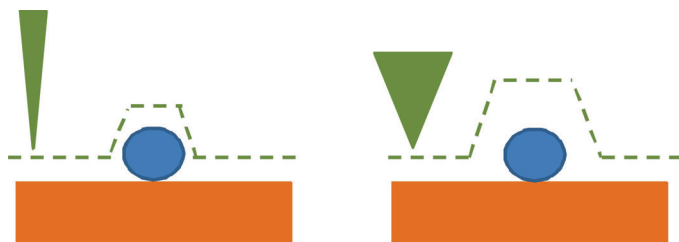


Figure 5.4: Difference between the STM (left) and AFM (right) tips. The sharpness of the tip determines the tip convolution.

5.3 AFM of Semiconductor Quantum Dots

For applying nanoparticles in devices such as solar cells [137] or transistors [138], it is not sufficient to know only the optical properties; it is indispensable to study their electrical properties. For this type of measurement at microscopic scale (local), usually, two different techniques are used: conductive atomic force microscopy (C-AFM) [139–141] and tunneling AFM (TUNA) [142], depending on the range of currents involved. The first is used to measure current in the range of sub-nA to μA , whereas the latter is used for the range between sub-pA and nA [143]. However, both techniques are performed in contact mode or near field interaction. This makes it hard to investigate materials that need low lateral or vertical forces because the standard forces of the AFM tip easily damage or deform the sample during the measurements. For this reason, contact mode is not appropriate for studying the topography and the conductivity of soft materials. Tapping mode can be a solution for studying the surface morphology of soft samples without destroying them, because during these measurements the cantilever oscillates at its fundamental flexural resonance, and the tip touches the sample only for a very brief period during oscillation. Indeed, under these conditions, the lateral forces, which are the causes of the damage to the samples, are eliminated and the vertical forces are reduced. Nevertheless, tapping mode is not compatible with conductivity measurements, which need near-field interactions, such as TUNA [144]. A possible solution for overcoming these issues is to use a type of AFM that works in non-contact mode and still able to detect tunnel current. Torsional Resonance Tunneling (TR-TUNA) AFM has these characteristics.

5.3.1 TR-TUNA AFM

5.3.1.1 Working principles

It is known that AFM cantilevers can oscillate in different modes, including the torsional resonance (TR) mode. In 2003, Huang and Su [145, 146] introduced

an AFM mode to overcome the limitations in conductivity mapping described in the last section. They used the TR amplitude (or phase) to control the feedback. The main advantage of this mode for TUNA is that low-force scanning can be performed while the tip is kept in the near-field, which allows tunneling currents to be obtained. Moreover, compared to scanning tunnel microscope (STM), TR-TUNA AFM has important benefits.

Since the lateral forces are used as feedback signal, instead of the tunnel current as in case of STM, it is possible to study non-conductive samples. Moreover, this technique also permits one to simultaneously obtain topography and current maps. Finally, the preparation of the samples for TR-TUNA measurements goes much faster than for STM measurements. In Fig. 5.5, a schematic illustration of the working principle of TR-TUNA is shown. Two piezo plates (blue color in Fig. 5.5) are incorporated into the tip holder and are used only for the excitation of torsional oscillations and do not interfere with the scanner piezo [147]. They extend and retract in the Z-direction. The interface between the AFM-tip and a sample during the AFM measurement is not well defined. Although in an ideal system there are only the tip, air and the sample, in ambient conditions there are contaminants at the interface due to the air humidity. A lock-in amplifier is used to measure the amplitude and the phase of the cantilever. The feedback maintains a constant lateral tip-surface interaction by constant torsional amplitude and phase, the output signal adjusts the Z position. Finally, a DC voltage is applied between the tip and the sample to measure the TUNA current. TR-TUNA has been applied to study the surface of liquids [148] and the conductivity in carbon nanotubes [149]. Furthermore, since in a common tip, the height is 10 - 20 times shorter than the cantilever length, the torsional detection is 10 or even 20 times more sensitive than the flexural detection.

5.3.1.2 Results

In this work the SnS and SnS/In₂S₃ core-shell nanoparticles were measured using a Veeco Dimension 3100 AFM equipped with an extended TUNA module for the current detection in the pA range. The tip has a conductive coating of Cr/Pt on both sides. For TR-TUNA mode, we used BudgetSensors ElectriMulti75-G cantilevers with the force constant of about 3N/m, a resonant frequency of about 75 kHz, and the torsional resonance frequency of about 400 kHz. In this chapter, it will be shown that by means of this technique, it is possible to study the size and shape of the nanoparticles and simultaneously obtain a map of the electrical current. The samples for these measurements were prepared by depositing the nanoparticles by drop casting on a chemically polished heavily doped n-type silicon wafer. It is important that the substrate

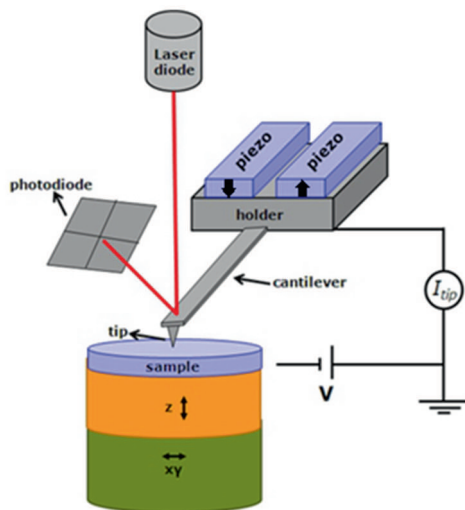


Figure 5.5: Illustration of the working principle of TR TUNA mode.

is as smooth as possible because it is impossible to detect the nanoparticles if the roughness is not negligible compared to their dimensions. A bias of -1V was applied between the sample and the tip, and it was kept constant during the measurements. The voltage is negative to prevent local anodic oxidation [150, 151]. Moreover, during the measurements, there is always an interface layer on top of the sample; sometimes it can be even a layer of moisture from humid air. A negative voltage allows the tip to get through this layer making sure that the sample and not just surface adsorbates are measured. In Fig. 5.6, two images are shown, corresponding to the topography (a) and the current (b) of SnS nanoparticles capped with TOPO, detected by TR-TUNA. The images have been analyzed using WSXM software [152]. Despite the fact that the measurements are noisy, in the topography image, it is still possible to identify agglomeration of nanoparticles though it is hard to distinguish single particles. It is possible to recognize a region of the sample with a high density of particles (Fig. 5.6a black circle). Comparing the topography image with the current map, it is possible to see a correlation, especially in the region with a higher density of nanoparticles, because their contribution to the current is higher and thus easier to detect. Overall, the current measured is rather low, resulting a noisy image. Even with more negative voltage of -10V , the image did not improve.

As mentioned earlier, the TR-mode is a non-contact mode, therefore, it is unlikely that the tip coating was somehow damaged. However, tip contamination is probable and can be a reason for the visible noise in AFM images. The

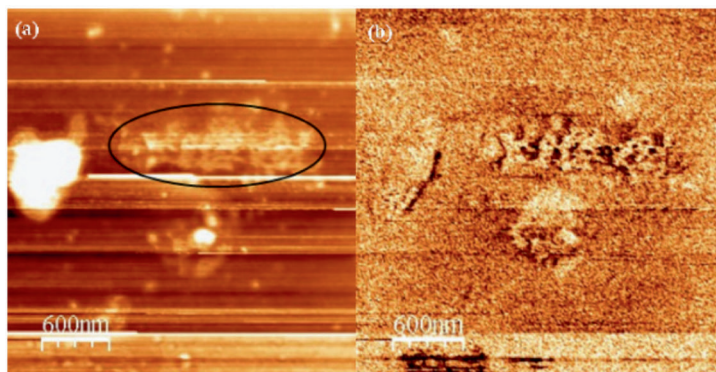


Figure 5.6: Topography (a) and current map (b) of SnS nanoparticles capped with TOPO acquired by TR-TUNA.

high noise level and low current might also be due to the presence of TOPO. Indeed, TOPO does not allow the tip to approach the particles properly, disturbing the measurement and making the images unclear. To overcome this issue and to verify our assumption, the nanoparticles were kept in solution, removing the TOPO from the SnS nanoparticles by acid treatment, using HCl. The particles were capped with an In_2S_3 shell by means of chemical bath deposition. Afterward, the same TR-TUNA measurements were carried out. This time a bias of -10 V was applied between the sample and the tip. Figures 5.7a and 5.7b show the topography image and the current map, respectively, of the SnS/ In_2S_3 core-shell nanoparticles. Now it is possible to distinguish the particles, and moreover, the correspondence between the topography image and the current map is evident. Quantitative information has been obtained studying the profile of one nanoparticle, marked with a white line, as shown in Figs. 5.7a and 5.7b. Furthermore, Fig. 5.7c shows a plot of the size (black curve) and current (red curve) of the nanoparticle along the white marked line. The size of the feature is 15 nm. The two curves have the same profile except for the center; the black curve indeed shows a peak that fits the shape of the nanoparticle perfectly while the red curve shows a dip. This can be explained if we consider the movement of the tip: when the tip is on the side of the particle, the surface of the tip near the particle is larger, hence, the detected tunnel current is also higher than when the tip is on top of the particles, where the surface is only a few nanometers and the current is lower. The evidence of the current proves that these nanoparticles are conductive and hence, they can be used in electronic devices. From a quantitative analysis, the maximum current value in Fig. 5.7(c) is 400 fA. The more conductive region are given by negative currents due to the negative voltage.

Despite the above shortcomings in current mapping TR-TUNA gives the

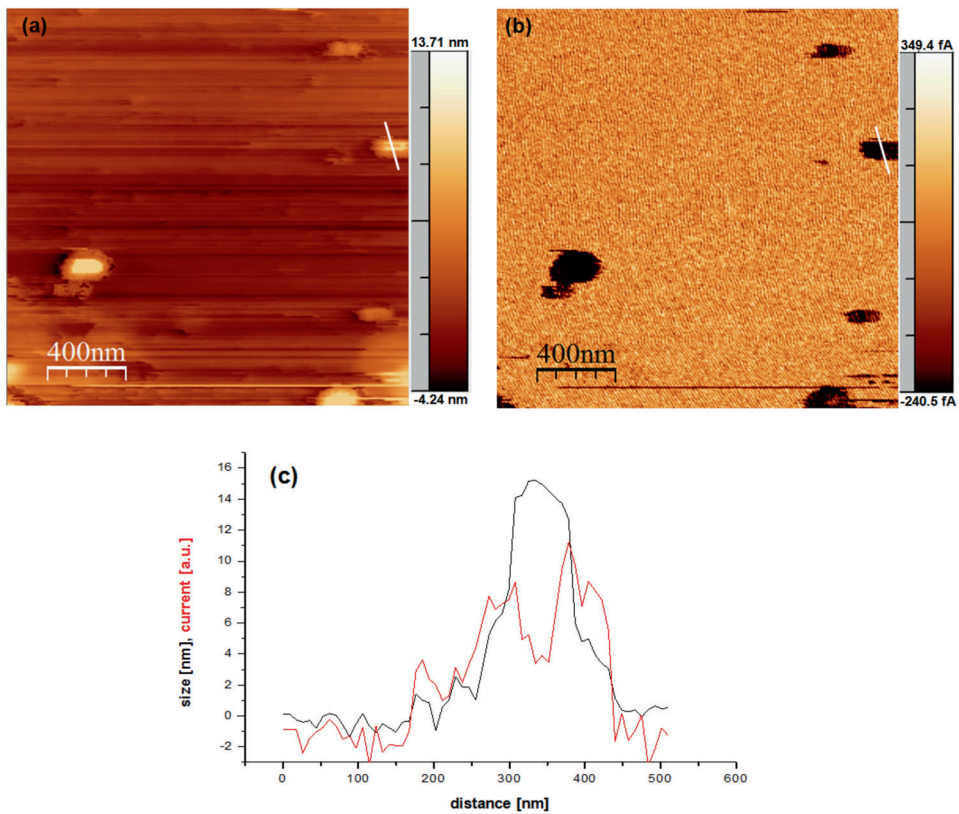


Figure 5.7: Topography (a) and current map (b) of SnS/In₂S₃ core-shell nanoparticles obtained by TR-TUNA; (c) profile of the size and the current on a single nanoparticle.

opportunity to obtain a complete characterization of a single nanoparticle. However, it has been shown above that when performing this type of measurements on particles capped by TOPO, the quality of the images is very low. In order to overcome this problem, it would be necessary to use another type of AFM which works in a mode similar to tapping mode but is able to detect the tunnel current. Peak Force AFM has been developed to address these problems.

5.3.2 Peak Force AFM

5.3.2.1 Working principles

Peak Force AFM works similarly to tapping mode. Indeed, the probe is brought intermittently onto the sample to avoid lateral forces and hence damage to the samples. The difference between the two methods is that for tapping mode the cantilever vibration amplitude is used as feedback and kept constant, while in Peak Force AFM the maximum force on the tip is controlled [153] and can be as low as 100 pN. Operating at such low forces, Peak Force AFM can give high resolution even on soft samples. Furthermore, the oscillation frequency, which is between the tapping and the contact modes frequencies, is also appropriate for working in TUNA mode because it allows the TUNA module to reside for a period long enough to detect the current signal. This is another advantage compared to tapping mode where the frequencies (too fast) make it impossible to operate in TUNA mode. Hence, Peak Force makes it possible to study the morphology and the current in order to get a complete characterization by means of one single measurement. Peak Force AFM has been used for imaging graphene, and DNA in solution and to simultaneously record topography and current maps of carbon nanotubes [153]. It also permits one to quantify the local elastic modulus [154].

5.3.2.2 Results

In this thesis Peak Force AFM has been applied to study the size, the shape and the current map of SnS nanoparticles. The SnS nanoparticles were synthesized via the colloidal route and capped with TOPO in order to avoid clustering, as shown in chapter 3. Afterward, the nanoparticles were deposited by drop casting on a Platypus gold substrate. This substrate was chosen because of its smoothness, which allowed us to detect small nanoparticles. The samples were measured by Bruker Icon AFM equipped with a PF-TUNA module for the current detection in the pA range. For PF-TUNA as well as for TR-TUNA modes, we used BudgetSensors ElectriMulti75-G cantilevers with a force constant of about 3 N/m, resonant frequency of about 75 kHz and a torsional

resonance frequency of about 400 kHz. It has a conductive coating of Cr/Pt on both sides. The set point of the Peak Force applied during the measurement was about 1.5 nN and the frequency of tip oscillations was 1 kHz. To detect the current and avoid the oxidation [151,155] a negative bias of -0.5 V was applied between the tip and the sample and kept constant during all the measurements. The scanning speed was 400 nm/s in case of TR-mode and 800 nm/s during the PF-mode. All AFM measurements were performed at 25°C and approx. 30% humidity of the ambient air.

The topography and current maps, shown in Fig. 5.8 (a) and (c) respectively, for Peak Force TUNA have been acquired investigating an area of $2 \times 2 \mu\text{m}^2$. In the topography map one can distinguish different nanoparticles with spherical shape, in accordance with TEM images of these particles reported in chapter 3. Comparing the images of Fig. 5.8a and Fig. 5.8c, the correspondence between the current map and the topography is evident. Indeed, the current map shows a good correlation of the value of the current with that of the size of the nanoparticles. The same area has also been investigated by TR-TUNA, in order to compare both techniques. The topography and current maps, shown in Fig. 5.8 (b) and (d) respectively, are acquired by TR-TUNA. Nanoparticles are visible in the topography map. However, the image is noisier and the resolution is lower than that of the image acquired by PeakForce AFM (Fig. 5.8a).

In the previous section we investigated this phenomenon and argued that it is due to the presence of TOPO, which hinders the approach of the tip. However, a more plausible reason could be that in TR-mode the AFM-tip is about 1 nm above from the sample and has lateral oscillations with amplitude of several nm. Thus the tip-sample interaction is not limited to the area directly under the tip, as in case of PF-mode, but it is also influenced by the neighboring nanostructures, which leads to a low resolution. The comparison between the two topography images illustrates the better performance of Peak Force AFM. This consideration is confirmed by current measurements. Fig. 5.8d. shows that it is impossible to detect any current using TR-TUNA, speculated to be due to TOPO that hinders the tunnel current.

This problem can be overcome by using Peak Force TUNA because it works in contact mode. Two nanoparticles, marked with number 1 and 2 in Fig. 5.8c have been investigated in order to obtain quantitative information. The profiles of these nanoparticles are reported in Fig. 5.9. The black curve shows the topography profile of the marked nanoparticles. The size was investigated by studying the z-profile of the nanoparticles to get a more precise value. This analysis shows that the nanoparticles have a size of around 2 nm, thereby demonstrating the accuracy of this technique, which enables one to detect even small particles. The red line corresponds to the current. It is in the

range between 2-5 pA. The features in both profiles in Fig. 5.9 coincide at the same positions. The size of the nanoparticles is also confirmed by TR-TUNA (dashed line in Fig. 5.9) which shows the same behavior of the topography profile acquired by Peak Force TUNA. A significant observation is that there is no dip in the current mapping by PF-TUNA, unlike the one that was observed in TR-TUNA in Fig. 5.7c. This result confirmed our hypothesis that the dip observed in TR-TUNA current map is an artifact of the technique. The above result confirmed the conductive nature of SnS nanoparticles. It should be noted here that SnS/In₂S₃ particles can also be studied by PF-TUNA. However, that was not done, as this information was already available from TR-TUNA study.

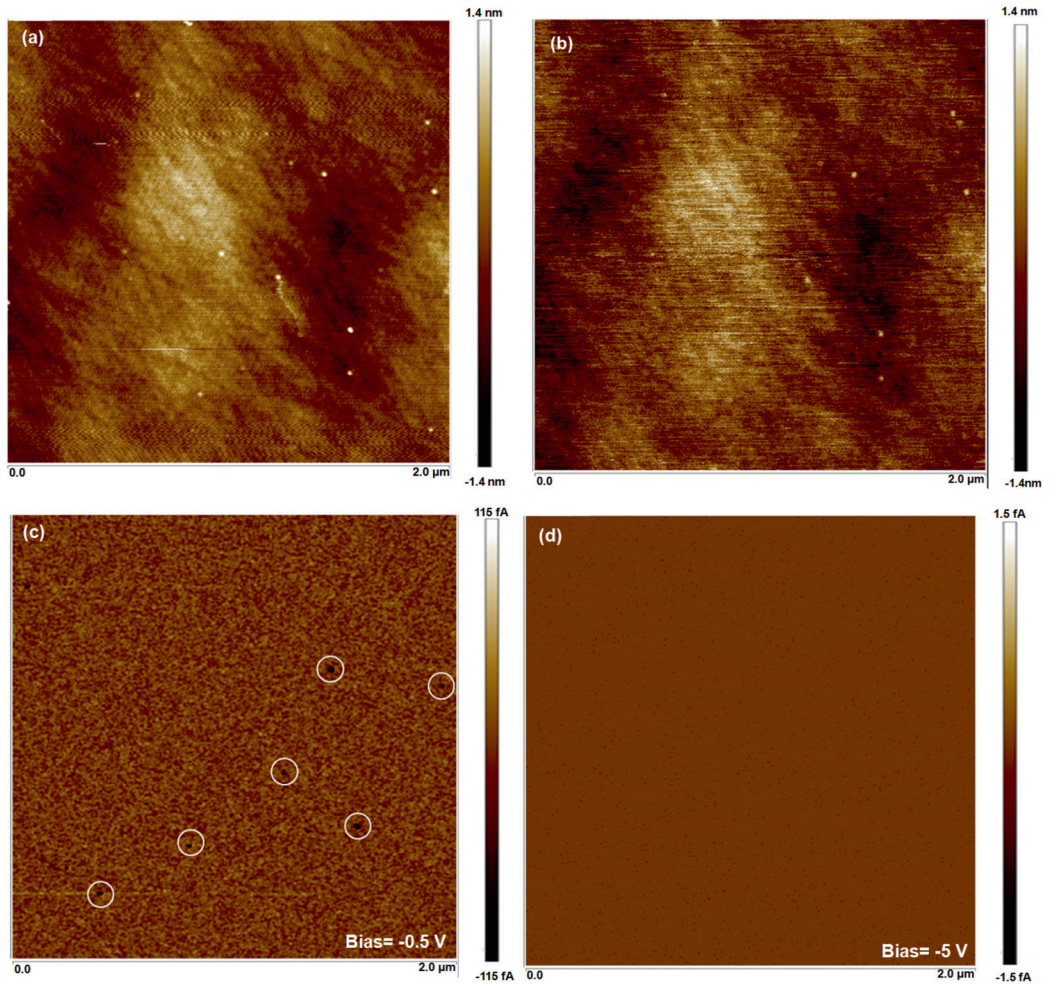


Figure 5.8: Topography maps acquired by PeakForce TUNA (a) and TR-TUNA (b) of SnS nanoparticles capped with TOPO deposited by drop casting on a Platypus gold substrate. Current maps acquired by PeakForce TUNA (c) and TR-TUNA (d) of SnS nanoparticles capped with TOPO.

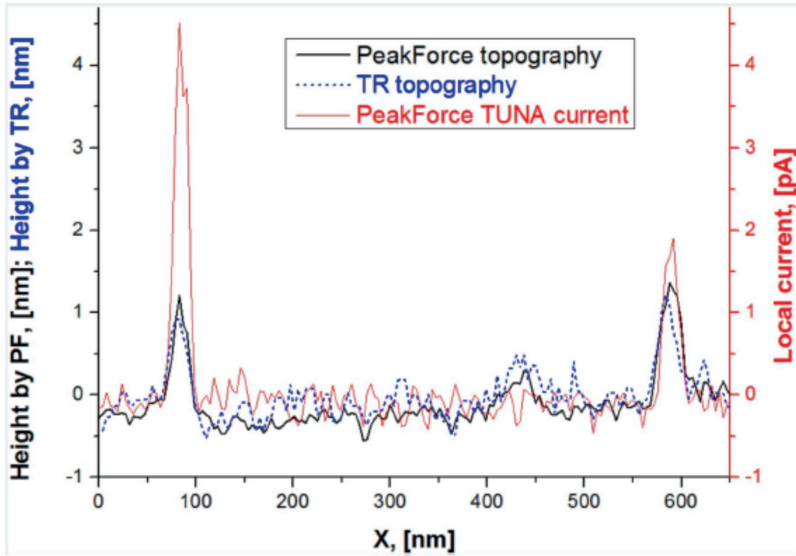


Figure 5.9: Profile of the size and the current on two single SnS nanoparticles capped with TOPO.

5.4 Conclusion

In this chapter the capability of TR-TUNA to study the electrical behavior of SnS nanoparticles coated with a semiconductor In_2S_3 shell has been demonstrated. The main advantage of this technique, compared with other AFM-based techniques, is the possibility of simultaneously studying the morphology and conductivity of soft materials. This gives the opportunity to obtain a complete characterization on a single nanoparticle. Moreover, it has been also found that when performing this type of measurements, the TOPO type capping should be avoided because TOPO prevents the tip from approaching the particle in a controllable manner.

For the analysis of nanoparticles capped with TOPO another technique has been used: the Peak Force TUNA. This technique was used to investigate SnS nanoparticles, simultaneously studying the topography and the conductivity. It is shown that this technique is ideal for investigating such delicate materials as nanoparticles without destroying them. Furthermore, it has been demonstrated that Peak Force TUNA can be used also to study the local conductivity of particles capped by TOPO, which is very problematic using TR-TUNA. These studies confirmed that both SnS and SnS/ In_2S_3 nanoparticles are conductive in nature.

Chapter 6

CIS solar cell embedded nanoparticles

CIGS solar cells are highly attractive because they have achieved high efficiency, more than 20% in laboratory and 13.5% on large areas. The main challenge for this type of solar cell is the up-scaling to large areas and further reducing the costs.

In this chapter we develop a new configuration for a CIS solar cell. The main differences of this CIS solar cell compared with a standard CIS cell are the “superstrate” configuration, the In_2S_3 instead of CdS as emitter layer and the TiO_2 instead of i-ZnO as buffer layer. It is important to highlight the fact that this cell is made by spraying, a cheap and easy deposition technique. The solar cell is characterized by I-V measurement, using a solar simulator and a spectral response measurement. We also investigated the effect of the copper gradient in the CIS absorber layer.

Moreover, in order to increase the efficiency, two types of quantum dots are embedded into the cells: SnS nanoparticles and SnS/ In_2S_3 core-shell nanoparticles. The role of the quantum dots is to create an intermediate layer that permits the photons to be absorbed with energy less than the band gap. Different configurations are tested in order to understand the working principle of the devices and to optimize them.

Finally, a CIGS absorber is used. This CIGS was made by co-evaporation technique using best known practices. This study allows us to understand clearly the effect of the In_2S_3 buffer and the role of SnS QDs embedded in this type of solar cell.

6.1 Introduction

In chapter 1 it was mentioned that Copper Indium Gallium Selenide (CIGS) solar cells consist of a metallic back contact, usually molybdenum, deposited on a soda-lime glass substrate; a p-CIGS absorber layer; an n-type buffer layer, which is usually CdS; an intrinsic ZnO buffer layer and a doped ZnO layer, used as transparent front contact. The solar cells are completed with a metallic grid deposited by evaporation. The band diagram of the CIGS solar cell, shown in Fig. 6.1, is useful for getting a better understanding of this type of solar cell. The wide band gap of the ZnO and the buffer layer allow the majority of photons to be absorbed in the p-type CIGS absorber. Then, the electron diffuse and they are collected in the n-side through drift over the junction. The open-circuit voltage is determined by the built-in potential. Thus, absorbers with higher band gap provides higher open-circuit voltage and lower short circuit current. The interface between the CdS emitter and the absorber layer is important because it creates a discontinuity in the conduction band.

In Table 6.1 different configurations of CIGS solar cells developed by different companies are reported [156]. In the first column the role of the layers and their thickness are shown.

CIGS absorber layers are commonly deposited by means of two techniques: co-evaporation of all 4 elements simultaneously (for short, “co-evaporation”) and metallic precursor deposition followed by selenization or sulfurization (for short often merely indicated as “selenization”). The co-evaporation process is used by Wurth Solar and Global Solar (red color in Table 6.1). Avancis, Johanna Solar, Showa Shell, Sulfurcell and Honda Soltec use the selenization or sulfurization approach instead (blue color in Table 6.1) [156]. In the co-evaporation process the elements copper, indium, gallium and selenium are evaporated simultaneously in optimum proportion, in order to obtain an uniform CIGS layer. This technique can be applied as an in-line process. The glass substrate is introduced in the setup and transported under the evaporation sources; there the substrate is heated up. The rates are controlled by means of atomic absorption spectroscopy. This process has been optimized using a “three-stage” approach. There is an initial Cu-poor phase which improves the current collection, followed by a Cu-rich phase and again another Cu-poor phase. It has been shown that using the “three-stage” process the efficiency of solar cells improves [157, 158]. The selenization/sulfurization process consists of two stages: the first stage is the deposition of precursors containing Cu, In and Ga and sometimes Se at low temperatures; the second stage is the recrystallization, sometimes with additional Se or S, at high temperature [159].

The quantum efficiency (QE) for a real CIGS solar cell is different from the QE simulated for an ideal solar cell. The real efficiency is much lower and these

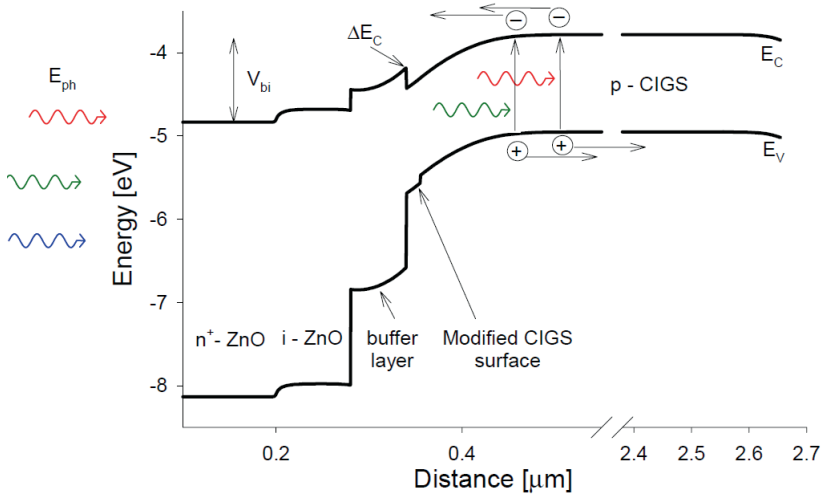


Figure 6.1: Band diagram for CIGS thin-film solar cell [160].

ρ

n-type window (1 μm)	ZnO:Al	ZnO:Al	ZnO:B	ZnO:Al	ZnO:Al	ZnO:Al
buffer (50-100nm)	CdS	CdS	Zn(S,OH) _x	CdS	CdS	Ins
p-type absorber (2-3 μm)	Cu(In,Ga)Se ₂	Cu(In,Ga)(Se,S) ₂	Cu(In,Ga)(Se,S) ₂	Cu(In,Ga)Se ₂	CuInS ₂	Cu(In,Ga)Se ₂
		Cu(In,Ga)Se ₂	Cu(In,Ga)Se ₂			
Metal back contact (0.5-1 μm)	Mo	Mo	Mo	Mo	Mo	Mo
		barrier	barrier	barrier		
Substrate	SLS glass	SLS glass	SLS glass	SLS foil	SLS glass	SLS glass
	Würth Solar Solibro	AVANCIS Johanna Solar	Showa Shell Sekiyu	Global Solar	Sulfurcell	Honda Soltec

Table 6.1: Layer stacks as applied by a selection of manufacturers of CIGS thin-film solar cells.

losses are due to the following reasons:

- *Reflection*: these losses are caused by partial coverage of the front surface with metal grids and the reflection at the front surface. To minimize the latter usually an anti-reflective coating is used.

- *Buffer*: Currently, this accounts for a major loss mechanism in CIGS solar cells. A possible method to overcome this issue would be reducing the thickness of the buffer layer or using another material with a higher band gap.

- *Recombination*: these losses have already been explained in the first chapter. They are due to the fact that not all the electron-hole pairs can be collected because they can recombine within the depletion zone.

- *Spectral mismatch*: these losses are due to the fact that photons with energy less than the band gap cannot be absorbed, and to the fact that the excess energy of high energetic photons is dissipated as heat.

6.2 Alternative buffer layers

Cadmium sulfide is the most common material used as a buffer layer in CI(G)S solar cells. One advantage of this material is that it can be deposited by means of chemical bath deposition, a cheap technique that allows the cost to be kept low. However, the toxicity of cadmium leads to opposition to use of this element due to its potential environmental impact and the serious risks it poses for human health. For this reason, alternative materials have been developed as buffer layers instead of cadmium. An advantage of these alternative materials is that their wider band gap allows short-wavelength photocurrent to be recovered, resulting in lower parasitic absorption. Some of these materials are ZnSe, ZnIn₂Se₄, In₂Se₃, In(OH)_xS_y and In₂S₃ [161]. In this work we focus on In₂S₃ as the buffer material [162, 163]. β -In₂S₃ has a band gap around 2 eV; it is an n-type semiconductor and all its optical, electrical and structural properties are suitable for application in CI(G)S solar cells. However, CdS is preferred as an emitter because it has a cubic structure which is much easier to grow compared with the orthorhombic structure of In₂S₃.

6.3 New configuration of CIS solar cells

The solar cells investigated in this chapter are different from standard CI(G)S cells described in the introduction of this chapter. In Fig. 6.2 two schematic drawings of a standard CIS cell (Fig. 6.2a) and the CIS cell developed in this work (Fig. 6.2b) are reported. The difference in configuration is clearly visible. For the standard CIS solar cell the glass is used as the substrate and the light comes from the side of the metal grids. This is called “substrate” configuration.

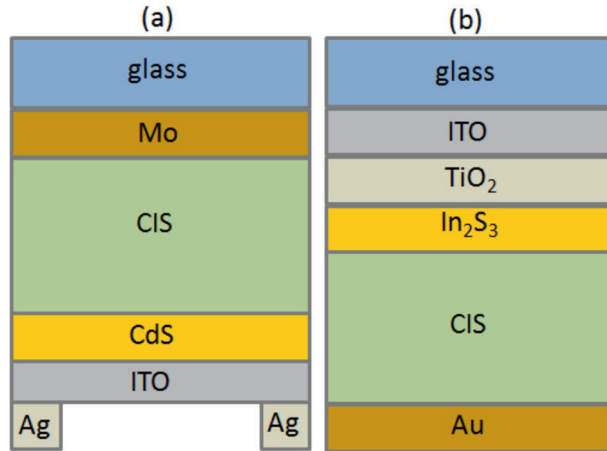


Figure 6.2: Schematic drawings of (a) common CIS solar cells and (b) configuration of the CIS solar cell developed in this thesis.

Instead, for the CIS cell developed in this work a “superstrate” configuration is used; the glass is used as the window for the illumination and it also serves as encapsulation. Moreover, the CdS was replaced with In₂S₃ and TiO₂ is used instead of intrinsic ZnO, due to its better coverage of the surface, as well as the fact that it is known to have lower conductivity. The i-ZnO layer, in the standard cells, is used as buffer to avoid metal diffusion, the same role can be played by TiO₂. Moreover, all the layers were deposited by spraying, from alcoholic precursors solution, on an ITO-glass substrate [164, 165]. This technique does not allow one to achieve the same degree of uniformity and homogeneity as co-evaporation or selenization techniques. However, this low temperature, non vacuum technique keeps production costs low; the performance of the solar cells is also lower.

Prior to producing the cells, studies have been carried out to optimize the quality of the layers. It has been found that a good quality of TiO₂ is obtained by the deposition of two successive thin layers followed by annealing at 400°C, as shown from XRD measurements reported in Fig. 6.3, where the peaks of the 2-step TiO₂ are sharper, meaning that the crystallinity is better. Moreover, both samples have been studied by means of impedance spectroscopy. This technique studies the impedance of a circuit in function of frequencies. In the Nyquist plot the real part of impedance (Z') in function of the imaginary part of the impedance (Z'') in a range of frequencies is reported and, for a simple RC circuit, it should be a semicircle where the diameter corresponds to the resistance of the circuit. Thus, observing Fig. 6.4 it is possible to see that the 2-step TiO₂ has higher resistance. However, only contribution of TiO₂ has been

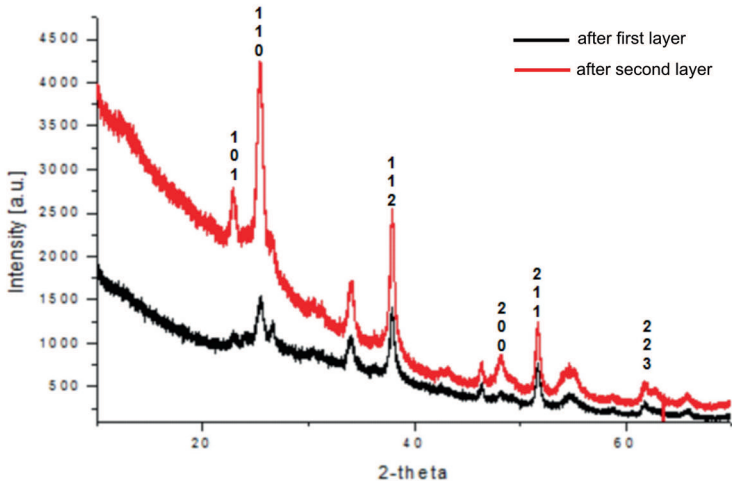


Figure 6.3: XRD measurements on single and double layers of TiO_2 .

observed and no contribution of the ITO, otherwise the Nyquist plot should have shown two semicircles. This means that the TiO_2 is a thick and dense layer and therefore less shunted.

The cell is completed by depositing first an In_2S_3 thin film and then a CIS layer. Both layers were deposited by the spraying technique. Afterwards, the cell was tested using a solar simulator to verify the photoresponse. The IV measurements were performed under AM1.5 light with an intensity of $100 \text{ mW}/\text{cm}^2$ and in the dark in a voltage range between -1 and 1 Volt. The results are shown in Fig. 6.5.

The CIS solar cell has also been investigated using spectral response measurements. The measurements were performed at $V=0$ and under reverse bias at -1 V, both voltages were used with and without bias light. These measurements permit one to study the performance of the device and to get information about the quality of the materials. The response of the cells can be used to determine the External Quantum Efficiency (EQE) measurement, i.e., how many electron-hole pairs are generated and collected, per photon at each wavelength. The effect of the bias light on the device gives information about the recombination in the solar cell. When the bias light is on, there is a split in the quasi-Fermi levels, which is much larger than to the spectral response measurement in dark conditions, where the splitting is negligible due to low intensity of the probe beam. The zone between the two quasi-Fermi levels contributes to the recombination. If the device is made with good semiconductor material the recombination is low because there are fewer defects and thus few recombination centers. For this reason the spectral response for good devices do not

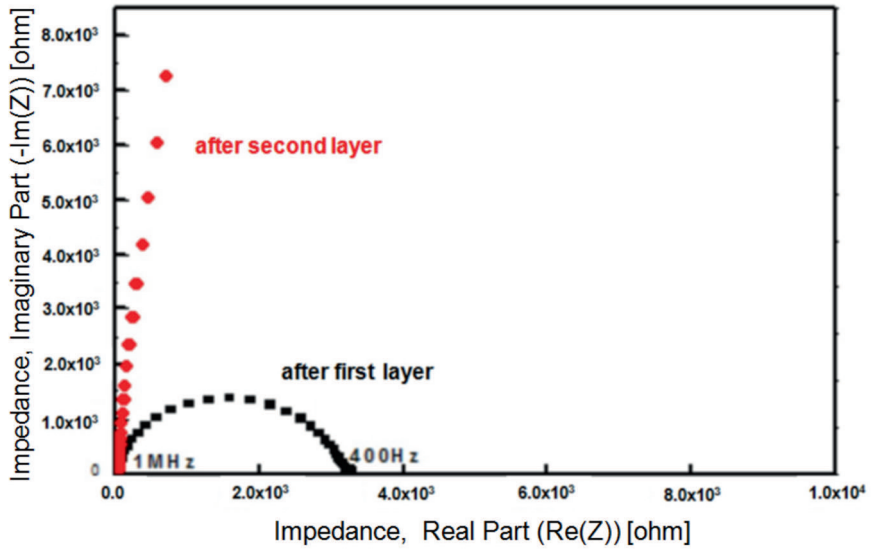


Figure 6.4: Nyquist plots of single and double layers with different thickness of TiO_2 .

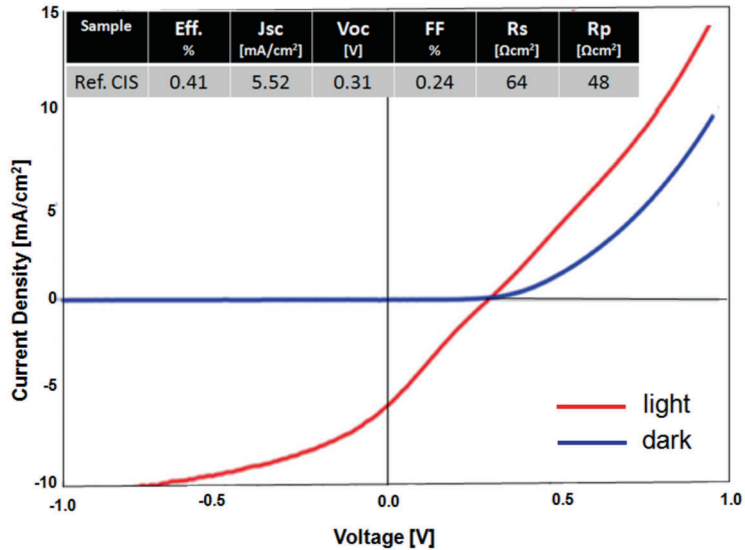


Figure 6.5: IV measurements performed on reference CIS solar cells.

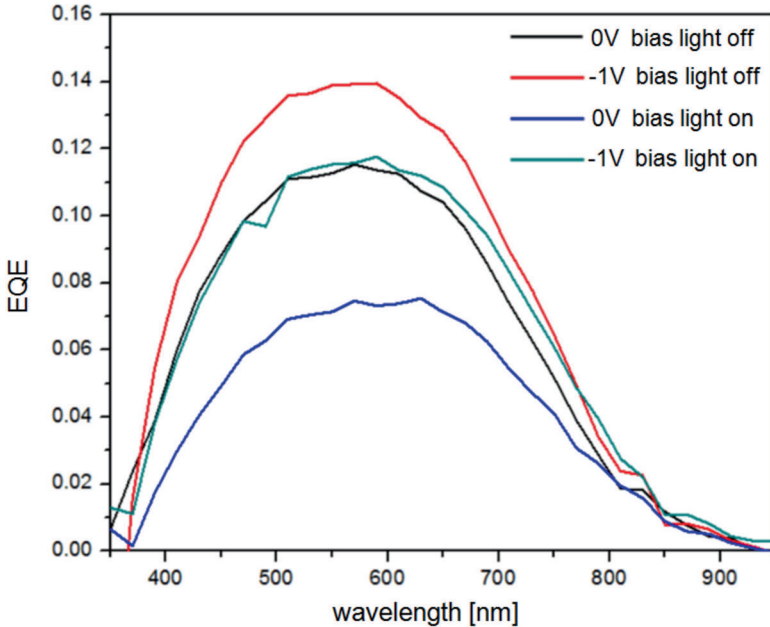


Figure 6.6: Spectral Response of a reference CIS solar cell.

show drastic changes between the curves with and without bias light. Observing the two curves at zero voltage for the CIS solar cell, reported in Fig. 6.6, it can be seen that when the light bias is on, the EQE drops. The same trend is observable at -1 V. Analyzing this performance it is inferred that this CIS solar cell shows a strong recombination.

The same conclusion can be drawn looking at the shape of the spectral response curves. Indeed, for optimum devices, the typical spectral response curves show a plateau followed by a step drop close to the band gap. Instead, in these spectra the EQE begins to decrease at 700 nm, well before reaching the wavelength corresponding to the band gap.

Nevertheless, the IV and the spectral response measurements prove that these CIS solar cells do work, showing a diode characteristic, though the efficiency ($\eta = 0.41\%$) is quite low.

6.3.1 The effect of copper gradient

In order to optimize this type of solar cell, different configurations of CIS layers were made and, at the same time, the effect of the 2-step TiO_2 was investigated. Four types of CIS cells were compared: a simple CIS solar cell with one single CIS layer with and without 2-step process of TiO_2 ; a solar cell made by stacking

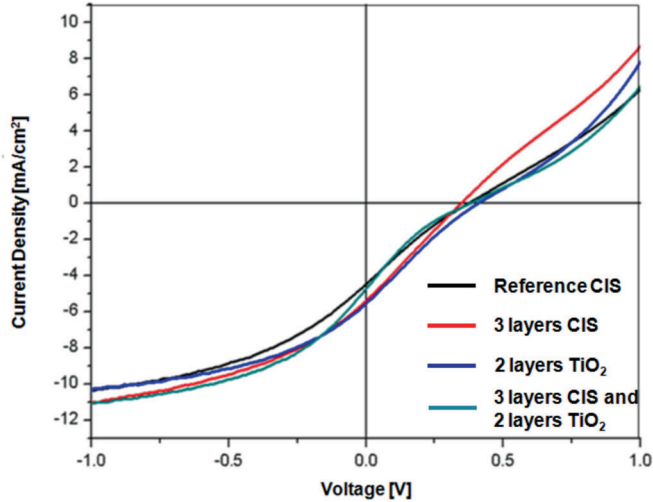


Figure 6.7: IV comparison for four different configurations of entirely sprayed CIS solar cells: a reference CIS solar cell, a CIS solar cell with copper gradient, both with and without 2-step process TiO_2 .

three thinner CIS layers with different copper concentrations, with and without 2-step process of TiO_2 . All four of these cells were completed deposited by spraying, except for the metal contacts. The IV curves were investigated using the solar simulator (Fig. 6.7), and the electrical parameters among the four solar cells were compared. There are no drastic changes in the values of the solar cells parameters, as shown in Table 6.2. The cells made with single layer of TiO_2 along with CIS and the cell with a double layer of TiO_2 along with a three-step deposited layer of CIS show the lowest performance in terms of efficiency, current and fill factor. This could be due to the fact that simple CIS structure is not well optimized. On the other hand, adding two layers of TiO_2 and three layers of CIS creates more interfaces which act as recombination centers. However, comparison of cells with the same CIS single layers shows that from these measurements, the application of two layers of TiO_2 improves the performance of the cell, confirming the results shown in section 1.3. It would be interesting to investigate whether some other treatments, such as annealing or different deposition temperature, of the three layers of CIS can reduce the recombination and further improve performance. This becomes a challenge if nanostructures are embedded into the cell, because it is necessary to find the right compromise, mainly in terms of temperature, so as not to destroy the nanoparticles.

In the next section the contribution of quantum dots embedded in these structure will be investigated.

Samples	Eff. [%]	Jsc [mA/cm ²]	Voc [V]	FF [%]	Rs [Ωcm ²]	Rp [Ωcm ²]
Reference CIS	0.3	4.47	0.37	0.21	112.3	73.14
CIS 3 layers	0.4	5.40	0.34	0.25	66.67	70.56
2x TiO ₂	0.5	5.54	0.40	0.22	105.3	73.57
2x TiO ₂ + CIS 3 layers	0.3	4.73	0.38	0.17	139.1	55.92

Table 6.2: Parameters of different configurations of entirely sprayed CIS solar cells: a reference CIS solar cell, a CIS solar cell with copper gradient, both with and without 2-step process TiO₂.

6.3.2 SnS QDs embedded in CIS solar cells

Two configurations of quantum dot CIS solar cells were evaluated and compared with the reference CIS (Fig.6.2b) cell with two layers of TiO₂. The schematic drawings of SnS QDs embedded in CIS solar cells are reported in Fig. 6.8. In the first configuration the SnS quantum dots are embedded between the In₂S₃ and the CIS layer, i.e., between the p- and the n- layers (Fig. 6.8a). In the other configuration SnS quantum dots are sandwiched between two layers of In₂S₃ (Fig. 6.8b).

First, the absorption (Fig. 6.9a) was investigated by means of reflection/transmission measurements to study the contribution of the single layer to the photocurrent [Fig. 6.9b and c], and calculated using the formula below:

$$\alpha = -\frac{1}{d} \ln \frac{T}{(1-R)^2} \quad (6.1)$$

where T and R are the transmittance and reflectance respectively, d the thickness of the layers measured by DekTak. Due to poor uniformity of the layers, the thickness has been measured at five points and the values have been averaged. From Fig. 6.9 it is clear how the layers affect the absorption.

IV curves, acquired using a solar simulator setup, were performed on these three configurations of CIS solar cells, with and without quantum dots, and their parameters were compared (Fig. 6.10). It can be seen that the solar cell with embedded nanoparticles between two layers of In₂S₃ shows an improvement compared with the reference CIS solar cell; while, the lowest performance corresponds to the cell where the nanoparticles are deposited between the absorber and the buffer layer. This could be due to the fact that the SnS

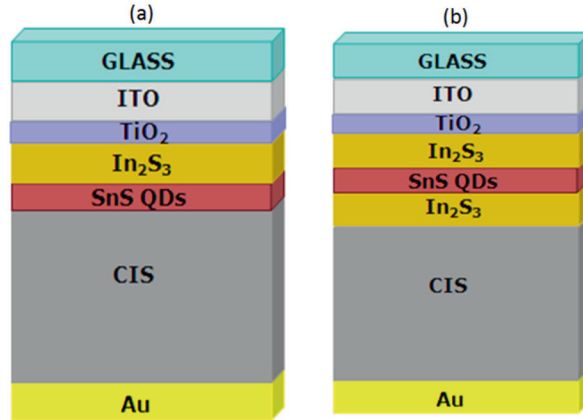


Figure 6.8: Schematic drawings of (a) SnS nanoparticles embedded between n- and p- region and (b) SnS nanoparticles sandwiched between two In₂S₃ layers.

nanoparticles are doped, as already mentioned in chapter three. The nanoparticles deposited on top of CIS layer create a hetero-junction with characteristics not suitable for CIS solar cells. Indeed, when the particles are embedded into the n-region this problem is avoided and the performance is enhanced.

6.3.3 Light and temperature dependencies

In this section we study how the parameters change with the light intensity and the temperature [166,167] to find out the charge transport mechanisms in the cells and to better understand the IV characteristics.

For the investigation of the light intensity dependent IV six gray filters were used with different transmission percentages. The IV curves acquired with different light intensities are reported in Fig. 6.11. It can be seen that the current changes drastically with the light intensity. However, no big changes in the open circuit voltage are detected.

To study the temperature dependence of IV, the cells were kept inside a box under nitrogen flow, the temperature was continuously checked by means of a thermocouple placed in the box in contact with the solar cell, and the IV curves were acquired by the solar simulator setup. The temperature was varied in the range between 30°C and 150°C. The curves were acquired at increasing temperatures and at the same temperatures during the cooling cycle, to verify if there is some permanent change due, perhaps, to an annealing effect.

The IV curves at different temperatures are reported in Fig. 6.12. The continuous lines correspond to the rising temperature, and the dashed lines

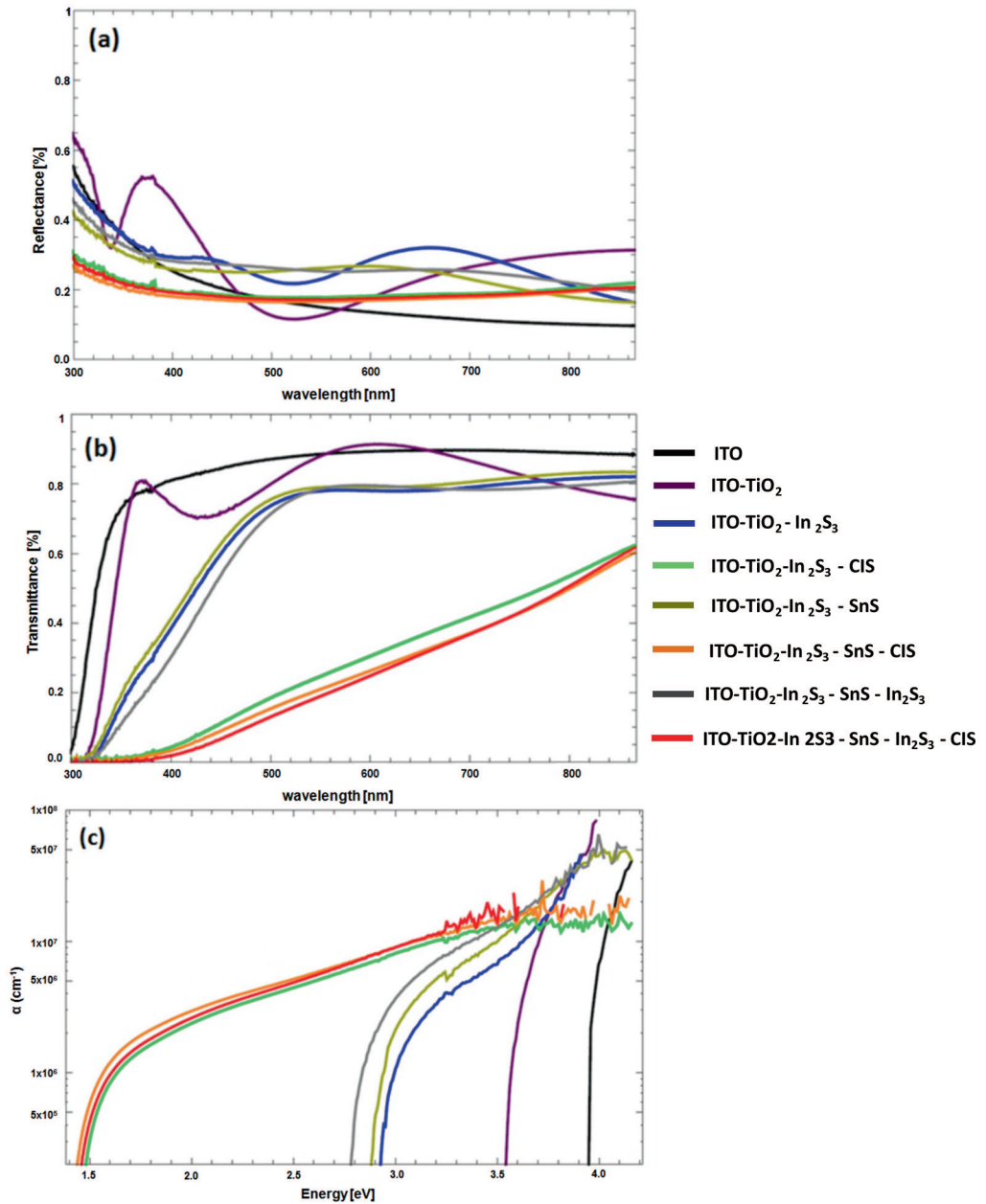


Figure 6.9: (a) reflection and (b) transmission measurements of the all layers which form the solar cells. (c) absorption obtained from reflection and transmission measurements, at various stages of cell preparation.

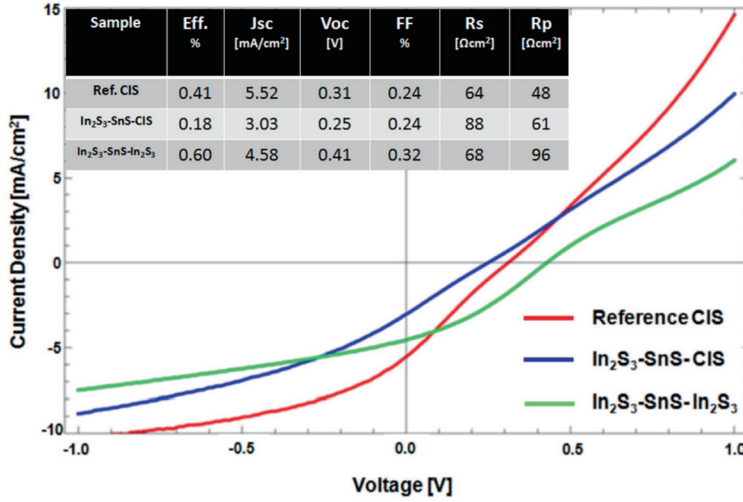


Figure 6.10: IV measurements done in the dark and under light on a reference CIS solar cell and boosted CIS solar cell with SnS nanoparticles embedded between n- and p-layer and sandwiched between two layers of In₂S₃.

to the cooling down period. The solar cell parameters have been analyzed. It has been found that, in contrast with the IV measurements as a function of light intensity, both the current and the open circuit voltage change. The current increases with increasing temperature, while the open circuit voltage decreases. This could be due to a decrease in the bandgap at higher temperature because of electron-phonon interaction. Moreover, it was found that the fill factor increases steadily with increasing temperature. Furthermore, the series resistance decreases for all samples and the shunt resistance increases, which has a positive effect on performance. A possible explanation can be that the minority carrier density increases because of the high temperature. The reference CIS sample has the highest increase in FF and the lowest loss in V_{OC} , but because of a larger decrease in J_{SC} than the other samples, the efficiency is not much higher. The IV curves acquired at the same temperatures during the cooling down, dashed lines in Fig. 6.12, show no big changes compared with the IV curves acquired at the same temperatures during the warming up. This indicates that restructuring of the lattices, due to some annealing, is probably not occurring.

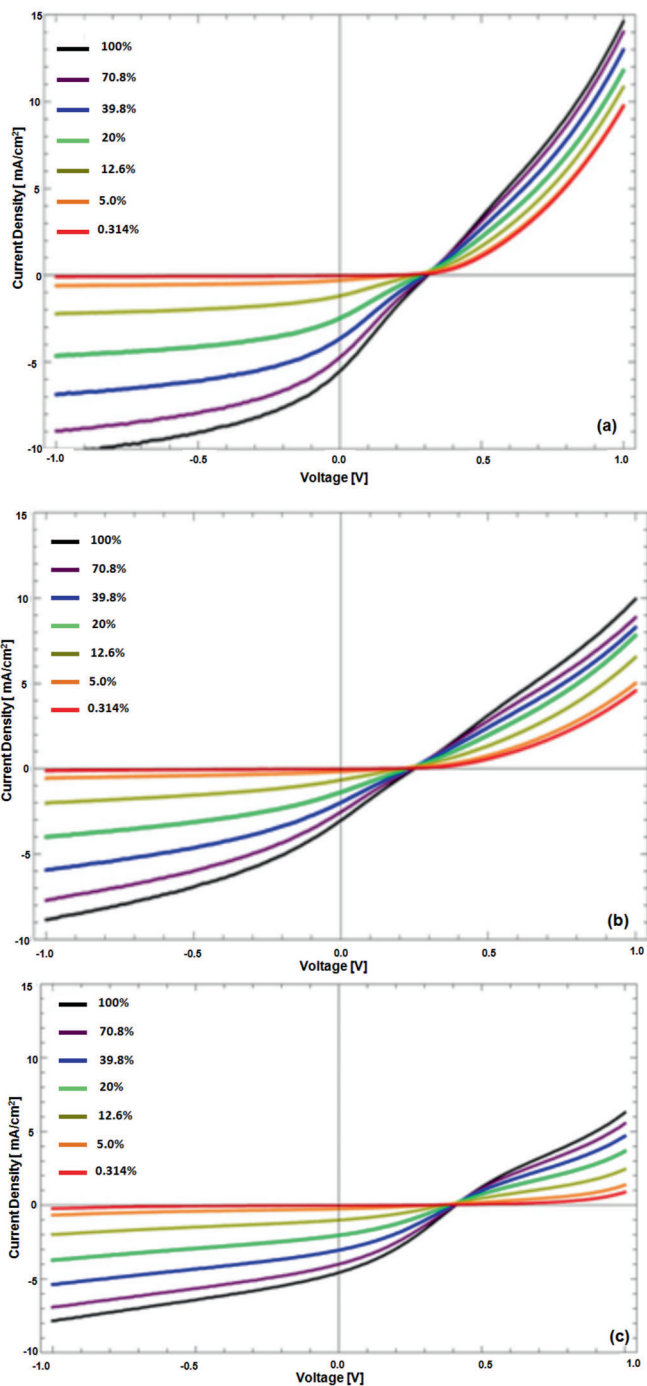


Figure 6.11: Light intensity dependence measurements on (a) reference CIS solar cell and boosted CIS solar cell by (b) SnS nanoparticles embedded between n- and p-layer and (c) sandwiched between two layers of In₂S₃.

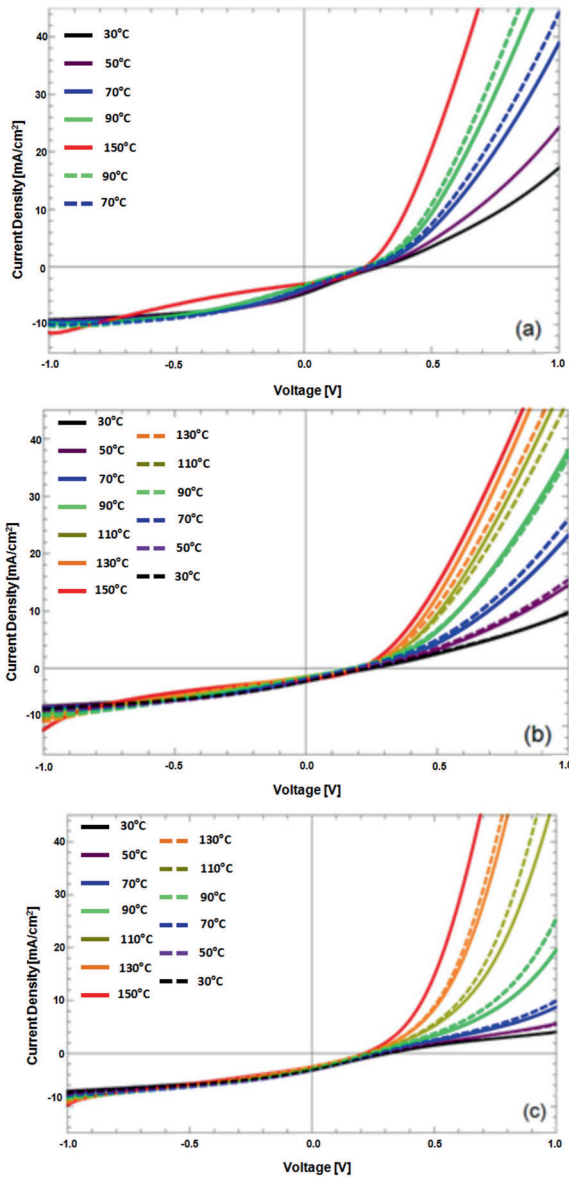


Figure 6.12: Temperature dependence measurements on (a) reference CIS solar cell and boosted CIS solar cell by (b) SnS nanoparticles embedded between n- and p-layer and (c) sandwiched between two layers of In₂S₃.

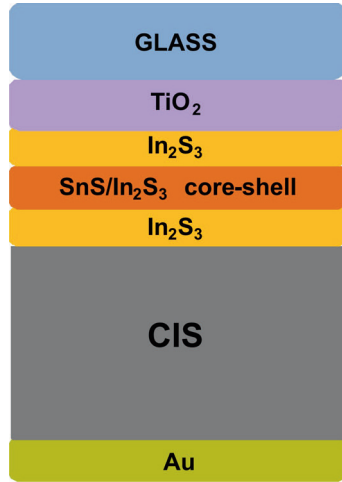


Figure 6.13: Schematic drawing of SnS/In₂S₃ core-shell nanoparticles embedded between two In₂S₃ layers in a CIS solar cell.

6.3.4 SnS/In₂S₃ core-shell nanoparticles embedded in CIS solar cells

SnS/In₂S₃ core-shell nanoparticles were embedded into CIS solar cells, as shown in Fig.6.13. This solar cell is compared with reference CIS and CIS with SnS nanoparticles. For all these solar cells the 2-step process TiO₂ configuration was used, as discussed in section 6.3. The IV curves of the solar cells were studied using the solar simulator under AM1.5 100 mW/cm² light and the results are shown in Fig. 6.14. In spite of the low efficiencies obtained for all these cells, these studies are important for acquiring valuable information to understand the loss mechanisms for future improvement. From Fig. 6.14, it is seen that the current and open circuit voltage for the reference CIS solar cell are higher than the same solar cell with nanoparticles. However, there is no difference in fill factor. All the curves show an S-shape, meaning that charge carriers experience a potential barrier or possibly a reverse diode is present in the layer stack. This is also confirmed by the series resistance values, reported in Table 6.3, determined from the light IV curve, using the software supplied with the solar simulator setup.

SnS nanoparticles and SnS/In₂S₃ core-shell nanoparticles were embedded into cells having CIS with the copper gradient, the three-layered configuration with different concentrations of copper. Once more, IV measurements were carried out on these three CIS solar cells with nanoparticles (Fig. 6.15). The

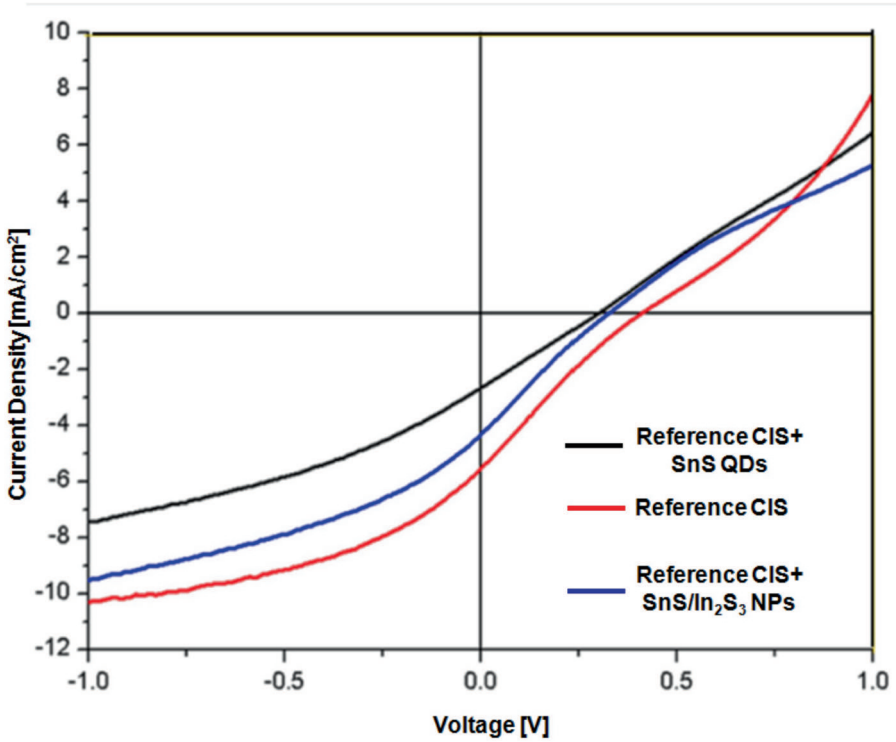


Figure 6.14: IV measurements performed on CIS, CIS with SnS QDs and SnS/In₂S₃ nanoparticles with 2-step process TiO₂.

Samples	Eff. [%]	Jsc [mA/cm ²]	Voc [V]	FF [%]	Rs [Ωcm ²]	Rp [Ωcm ²]
Reference CIS	0.5	5.54	0.40	0.22	105.3	73.57
Reference CIS+ SnS QDs	0.2	2.66	0.29	0.25	106.3	115.4
Reference CIS+ SnS/In ₂ S ₃ QDs	0.3	4.33	0.32	0.23	93.29	76.37

Table 6.3: Parameters of different configurations of solar cells: CIS, CIS with SnS QDs and SnS/In₂S₃ nanoparticles with 2-step process TiO₂

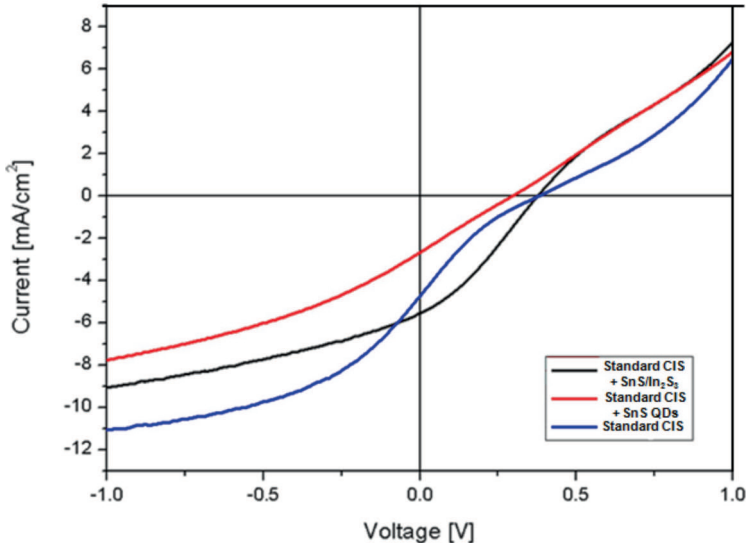


Figure 6.15: IV measurements performed on CIS, CIS with SnS QDs and SnS/In₂S₃ nanoparticles with 2-step process TiO₂ and three layers of CIS.

IV curve corresponding to the reference CIS solar cells with two layers of TiO₂ and three layers of CIS has an S-shape. As already mentioned in case of single CIS layer, this could be due to a potential barrier or the presence of a double diode. The results in Fig. 6.15 are a further confirmation that when SnS QDs are embedded between the n- and the p-layers, the performance is worse. As it was already explained, this happens because this type of particles are n-type and the layer made with these nanoparticles creates a junction. The IV curve of the cells with core-shell nanoparticles shows that the current is a bit higher compared with the other cells, but the voltage is similar to the cell without nanoparticles. Nevertheless, the fill factor and the efficiency are almost doubled with respect to the reference cell, as reported in Table 6.4.

6.4 SnS QDs embedded into CIGS solar cells

In this section SnS nanoparticles embedded in CIGS solar cells are investigated. Molybdenum sputtered on glass was used as substrate. The CIGS absorber layer was deposited by co-evaporation at TNO/Eindhoven laboratory. This absorber layer was chosen because it has already been studied and optimized. CIGS material, as already reported, has a band gap higher than that of CIS. Afterwards, the In₂S₃ layer was deposited on CIGS by spraying. The cell was completed by depositing i-ZnO and AZO thin films by sputtering, and

Samples	Eff. [%]	Jsc [mA/cm ²]	Voc [V]	FF [%]	Rs [Ωcm^2]	Rp [Ωcm^2]
Reference CIS	0.32	4.73	0.38	0.17	139.1	55.92
Reference CIS+ SnS QDs	0.19	2.67	0.29	0.24	116	108
Reference CIS+ SnS/In ₂ S ₃ QDs	0.64	5.54	0.37	0.30	57.76	138.4

Table 6.4: Parameters of different configurations of solar cells: CIS, CIS with SnS QDs and SnS/In₂S₃ nanoparticles with 2-step process TiO₂ and three layers of CIS.

metal grids on top were deposited by evaporation. To investigate the influence of quantum dots in this type of solar cell, an SnS QD thin film was spray-deposited between two In₂S₃ layer depositions. The schematic drawings of both structures are given in Fig. 6.16.

The IV characteristics for both configurations were studied with the solar simulator setup. The IV curves are reported in Fig. 6.17. The orange curve corresponds to the reference CIGS cell while the blue curve corresponds to the solar cell with embedded SnS QDs. Both curves show a diode behavior, but the reference CIGS solar cell has higher current. The QD solar cell has on the other hand, has much higher open circuit voltage. This can be seen more clearly in Table 6.5 where all the solar cell parameters are reported. As stated, the J_{SC} is slightly higher for the solar cell without QDs, whereas the V_{OC} is higher for the CIGS solar cell with SnS QDs, the same for the FF. Lastly, the efficiency of CIGS with QDs is higher than that of the reference CIGS solar cell.

Spectral response data were acquired to check the external quantum efficiency of both solar cells (Fig. 6.18). Both solar cells show a response in the range of wavelengths between 400 nm - 1100 nm. However, the response of the reference CIGS cell is higher than that of the CIGS with QDs, confirming the results obtained from the IV measurements. Nevertheless, the response of reference CIGS is very low compared with the commercial CIGS solar cells. Two are the main reason for this. First, the poor quality of sprayed In₂S₃ thin films. The second reason could be due to the thickness of the cells. Indeed, it has been proven that the efficiency of cells decreases as the emitter thickness increases. [168,169].

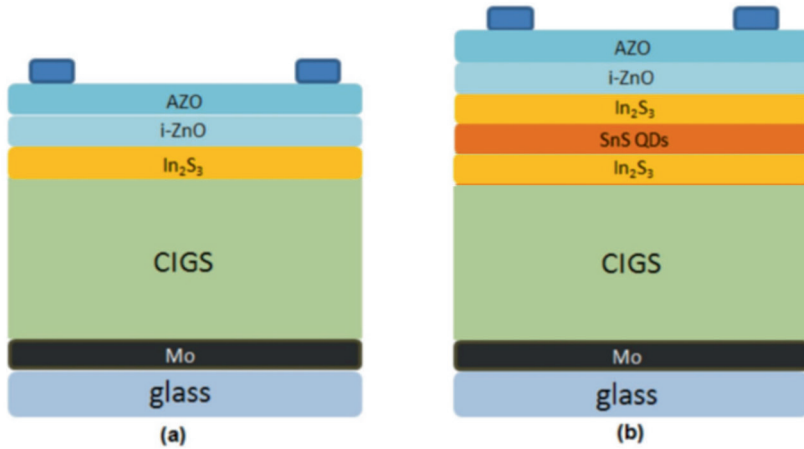


Figure 6.16: Drawing of (a) CIGS solar cells with In_2S_3 as buffer layer and (b) CIGS with In_2S_3 as buffer layer and SnS QD thin film embedded between the absorber and the buffer layer.

The same solar cells with and without quantum dots have been measured again two days later in order to check their aging effect. The IV curves are reported in Fig. 6.19, and the solar cells parameters in Table 6.6. From the IV curves it can be seen that the main change is the J_{SC} for both cells, with and without quantum dots. The other parameters do not show any change. Of course, due to the current increase the efficiency also increases, achieving 6.17% for the cell with quantum dots. This behavior could be due to the aging effect, which improves the performance of the cell [170]. Moreover, once again the performance for the cell with QDs is better than the reference cell without quantum dots.

These results prove that the quantum dots do not behave as an intermediate band because the current does not increase. Despite the fact that the SnS nanoparticles are monodisperse, the spray technique does not allow one to obtain uniform QD layers, and this prevents the creation of an energy band, which is a necessary condition to create an intermediate band. Nevertheless, SnS QD thin films act as a diffusion barrier improving the V_{OC} of the solar cells.

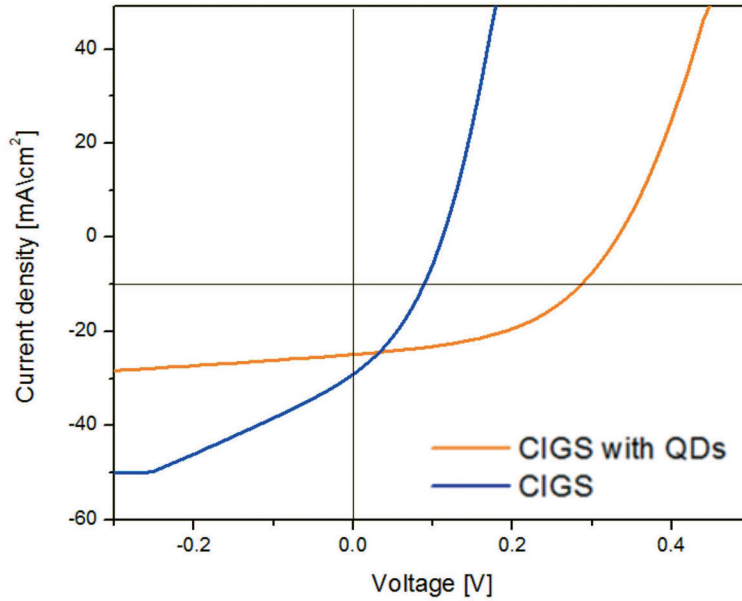


Figure 6.17: IV curves acquired by solar simulator on CIGS solar cell (orange curve) and the same type of cell with SnS QDs embedded (blue curve).

Samples	Eff. [%]	Jsc [mA/cm ²]	Voc [V]	FF [%]	Rs [Ωcm ²]	Rp [Ωcm ²]
Reference CIGS	1.13	29	0,11	0.34	20.13	81.12
Reference CIGS+ QDs	3.97	25	0.33	0.48	37.22	76.92

Table 6.5: Solar cell parameters for CIGS solar cell with and without SnS QDs (first measurement).

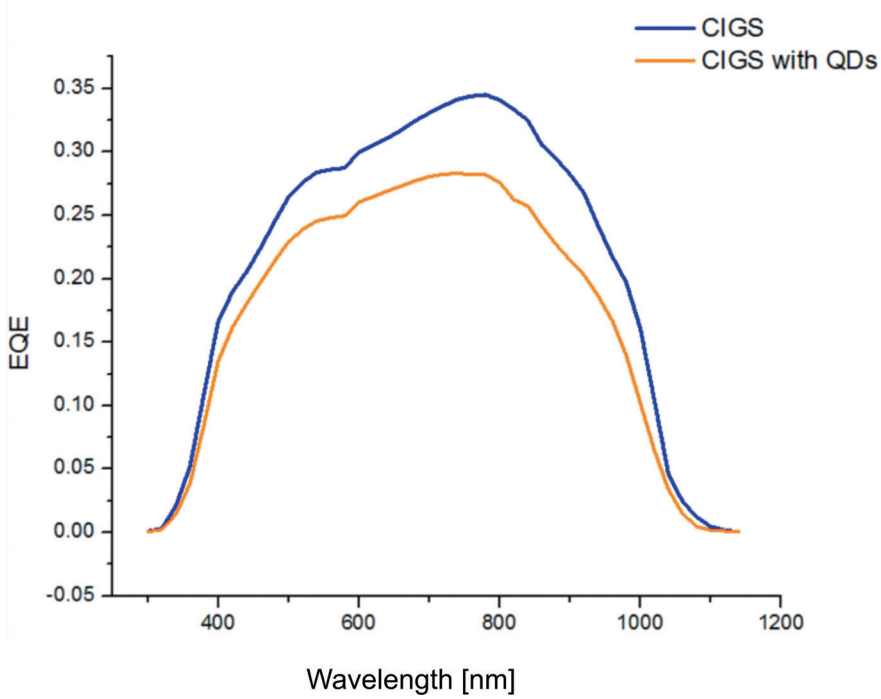


Figure 6.18: Spectral response curves for reference CIGS solar cell without (orange line) and with embedded SnS QDs (blue line).

Samples	Eff. [%]	Jsc [mA/cm ²]	Voc [V]	FF [%]	Rs [Ωcm ²]	Rp [Ωcm ²]
Reference CIGS	2.18	45.6	0.14	0.34	176.1	591.8
Reference CIGS+ QDs	6.17	38.8	0.34	0.46	28.51	739

Table 6.6: Solar cell parameters for CIGS solar cell with and without SnS QDs measured two days later.

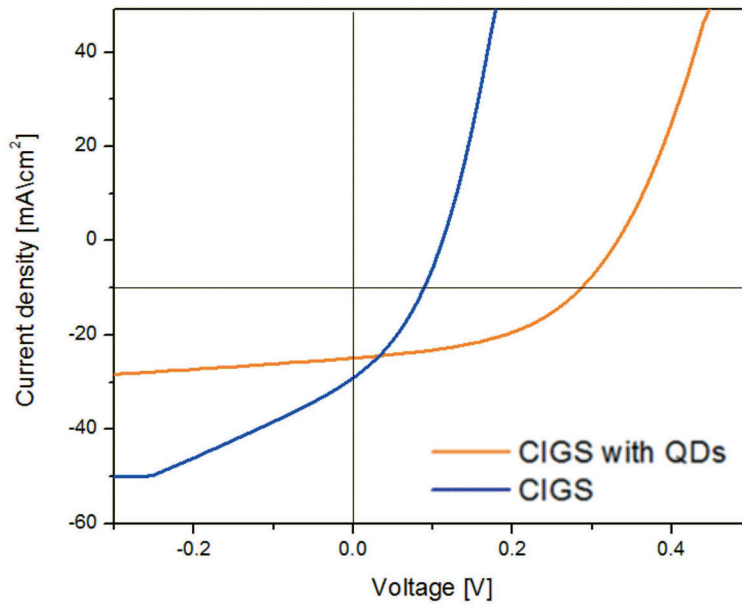


Figure 6.19: IV curves acquired using the solar simulator setup for a CIGS solar cells (blue curve) and the same type of cell with SnS QDs embedded in the In_2S_3 layer (orange curve) measured two days later.

6.5 Conclusion

In this chapter a preliminary study about quantum dots embedded into solar cells is presented. First, different configurations of CIS solar cells were developed, using a superstrate type structure instead of a substrate type of configuration which is the most common type configuration used for commercial CIS solar cells.

Then, SnS nanoparticles were embedded in spray deposited CIS solar cells at two different positions: between the n- and p-regions and sandwiched between two In_2S_3 layers. IV measurements were performed on these two CIS solar cells and a reference cell without SnS QDs, and the light and temperature dependencies were studied.

Thereafter, SnS were replaced by SnS/ In_2S_3 nanoparticles and compared the performance of the solar cell with core-shell NPs embedded with a reference CIS and with CIS cells with SnS NPs. Moreover, the effect of these two types of nanoparticles on CIS with two layers of TiO_2 and three layers of CIS were studied.

From the measurements carried out and reported in this chapter it is concluded that incorporation of quantum dots does not destroy the cell and that the process does not lead to the creation of any additional recombination centers. SnS embedded between CIS and In_2S_3 layers, however, drastically reduces the performance of the cell. This could be due to the formation of a new hetero-junction at the interface of the SnS quantum dot layer and the CIS layers because of the doped nature of the nanoparticles. The interface does not have suitable properties and reduces the efficiency of the cell. So far, it seems that SnS/ In_2S_3 core-shells lead to better performance. The main issue is, most probably, the quality of the CIS layer. Indeed, even the reference CIS solar cell does not have high efficiency. This is due to the deposition technique of spraying, which needs to be improved and optimized. From these results it is possible to infer that quantum dots can improve the efficiency of solar cells, but it is still important to first optimize the spray deposition technique and thus the quality of CIS layers.

Finally, co-evaporation deposited CIGS layers were used as absorber materials instead of sprayed CIS because this type of material is already optimized. In_2S_3 is used as a buffer and deposited by spraying. CIGS with and without QDs were compared to get a better understanding of the role and the influence of SnS QDs within the solar cell. These solar cells were characterized using IV measurements under AM1.5 light condition and spectral response measurements. The results show that SnS QDs help to increase the V_{OC} . This could be due to their role as diffusion barrier and thus improve the performance of the buffer layer the interface between CIGS, but decrease the current. The

same CIGS solar cells were measured two days after being stored in ambient conditions. The IV measurements showed an increase of J_{SC} and, accordingly, the efficiency. From these results it is concluded that the CIGS solar cells with quantum dots show a better performance. However, in the present cell design, the quantum dots do not play the expected role in forming intermediate band, but rather they act as a buffer layer that improves the V_{OC} .

Bibliography

- [1] BP energy outlook 2035. 2014.
- [2] BP statistical review of world energy. 2014.
- [3] www.our-energy.com.
- [4] World energy outlook 2013. 2013.
- [5] G.W. Crabtree and N.S. Lewis. Solar energy conversion. *Physics Today*, pages 37–42, 2007.
- [6] N.S.Lewis and D.G.Noceral. Powering the planet:chemical challenges in solar energy utilization. *PNAS*, 103(43):15729–15735, 2006.
- [7] A.E.Bacquerell. Recherches sur les effets de la radiation chimique de la lumiere solaire au moyen des courants electriques. *Comptes Rendus de l'Academie des Sciences*, 9(145), 1839.
- [8] C. Fritts. On a new form of selenium photocell. *Proc. Am. Assoc. Adv. Sci.*, 33(97), 1883.
- [9] A. Luque and S. Hegedus. Handbook of photovoltaic and engineering. 2011.
- [10] D. Reynolds, G. Leies, L. Antes, and R. Marburger. Photovoltaic effect in cadmium sulfide. *Physics Review*, 96(2):533–534, 1954.
- [11] W.Shockley and H.J. Queisser. Detailed balance limit of efficiency of p-n. junction solar cells. *J. Appl. Phys.*, 32:510, 1961.
- [12] B.S. Richards. Enhancing the performance of silicon solar cells via the application of passive luminescence conversion layers. *Solar Energy Materials and Solar Cells*, 90:2329–2337, 2006.
- [13] M.A Green. The path to 25% silicon solar cell efficiency: History of silicon cell evolution. *Prog.Photovolt: Res. App.*, 17:183–189, 2009.

- [14] http://www.epia.org/fileadmin/user_upload/publications/gmo_2013_-_final_pdf.pdf.
- [15] D.E. Carlson and C.R. Wronski. Amorphous silicon solar cell. *Appl. Phys. Lett.*, 28(11):671–673, 1976.
- [16] S.Benagli, D. Borrello, E. Vallat-Sauvain, J. Meier, U. Kroll, J. Hotzel, J. Spitznagel, J. Steinhauser, L. Castens, and Y. Djeridane. High-efficiency amorphous silicon devices on LPCVD-ZnOTCO prepared in industrial KAI-M R&D reactor. *Proceedings of 24th European Photovoltaic Solar Energy Conference*, pages 2293–2298, 2009.
- [17] <http://actu.epfl.ch/news/new-world-record-efficiency-for-thin-film-silicon/>.
- [18] B.Yan, G. Yue, L. Sivec, J. Yang, S. Guha, and C.S. Jiang. Innovative dual function nc-SiO_x:H layer leading to a >16% efficient multi-junction thin-film silicon solar cell. *Appl.Phys. Lett.*, 99:113512, 2011.
- [19] J.Loferski. Theoretical consideration governing the choice of the optimum semiconductor for photovoltaic solar energy conversion. *J. Appl. Phys.*, 27:777–784, 1956.
- [20] <http://www.empa.ch/plugin/template/empa/3/131438/—/1=2>.
- [21] P. Migliorato, J.L. Shay, H.M. Kasper, and S. Wagner. Analysis of the electrical and luminescent properties of CuInSe₂. *Jour. Appl. Phys.*, 46:1777–1782, 1975.
- [22] S. Wagner, J. Shay, P. Migliorato, and H. Kasper. CuInSe₂/CdS solar cells. *Appl. Phys. Lett.*, 25:434–435, 1974.
- [23] J.Shay, S. Wagner, and H. Kasper. Efficient CuInSe₂/CdS solar cells. *Appl. Phys. Lett.*, 27:89–90, 1975.
- [24] S. Wei and A. Zunger. Band offset and optical bowings of chalcopyrites and znbased II-VI alloys. *J. Appl.Phys.*, 78:3846, 1995.
- [25] <http://investor.firstsolar.com/releasedetail.cfm?releaseid=743398>.
- [26] G. Conibeerl. Third-generation photovoltaics. *Material Today*, 10(11):42–50, 2007.
- [27] G.F. Brown and J. Wu. Third generation photovoltaics. *Laser and Photon. Rev.*, 3(4):394–405, 2009.

-
- [28] A. Marti¹ and G.L. Araujo. Limiting efficiencies for photovoltaic energy conversion in multigap system. *Solar Energy Materials and Solar Cells*, 43:203–222, 1996.
- [29] M.A. Green, K. Emery, Y. Hishikawa, and W. Warta. Solar cell efficiency table (version 35). *Progr. Photovolt. Res. App.*, 18:144, 2010.
- [30] T. Trupke, M.A. Green, and P. Würfel. Improving solar cell efficiencies by up-conversion of sub-gap light. *Journal of Applied Physics*, 92(7):4117–4122, 2002.
- [31] T. Trupke, M.A. Green, and P. Würfel. Improving solar cell efficiencies by down-conversion of high-energy photons. *Journal of Applied Physics*, 92(3):1668–1674, 2002.
- [32] A. Marti and A. Luque. Next generation photovoltaics: High efficiency through full spectrum utilization. page 61, 2004.
- [33] B.K. Ridley. The electron-phonon interaction in quasi-two-dimensional semiconductor quantum-well structures. *J. Phys. C: Solid State Phys.*, 15:5899–5917, 1982.
- [34] R.T. Ross and A.J. Nozik. Efficiency of hotcarrier solar energy converters. *J. Appl. Phys.*, 53:3813–3818, 1982.
- [35] S.K. Stubbs, S.J.O. Hardman, D.M. Graham, B.F. Spencer, W.R. Flavell, O. Masala P. Glarvey, N.L. Pickett, and D.J. Binks. Efficient carrier multiplication in inorganic nanoparticles. *Physical Review B*, 81:081303–1–081303–4, 2010.
- [36] R.D. Schaller and V.I. Klimov. High efficiency carrier multiplication in PbSe nanocrystals: Implications for solar energy conversion. *Physical Review Letters*, 92(18):186601–1–186601–4, 2004.
- [37] R.D. Schaller, M.A. Petruska, and V.I. Klimov. Effect of electronic structure on carrier multiplication efficiency: Comparative study of PbSe and CdSe nanocrystals. *Applied Physics Letters*, 87:253102–1–253102–3, 2005.
- [38] M.C. Beard, K.P. Knutsen, P. Yu, and Q. Song J.M. Luther, W.K. Metzger, R.J. Ellingson, and A.J. Nozik. Multiple exciton generation in colloidal silicon nanocrystals. *Nano Letters*, 7(9):2506–2512, 2007.
- [39] A. Luque, A. Marti¹, and A.J. Nozik. Solar cells based on quantum dots: Multiple exciton generation and intermediate bands. *MRS bulletin*, 32:236–241, 2007.

- [40] M.C.Hanna and A.J. Nozik. Solar conversion efficiency of photovoltaic and photoelectrolysis cells with carrier multiplication absorbers. *J. Appl. Phys.*, 100:074510, 2006.
- [41] A. Luque and A. Martí. Increasing the efficiency of ideal solar cells by photon induced transitions at intermediate levels. *Physical Review Letters*, 78(26):5014–5017, 1997.
- [42] M.Wolf. Limitations and possibilities for improvement of photovoltaic solar energy converters: Part I: Considerations for earth’s surface operation. *Proceedings of the Institute of Radio Engineers*, 48:1246–1263, 1960.
- [43] A. Luque and A. Martí. A metallic intermediate band high efficiency solar cell. *Prog. in Photovolt. Res.Appl.*, 9:73–86, 2001.
- [44] A. Luque, A. Martí, E. Antolin, and C. Tablero. Intermediate bands versus levels in non-radiative recombination. *Physica B*, 382:320–327, 2006.
- [45] A. Martí, L. Cuadra, N. Lopez, and A. Luque. Intermediate band solar cells: Comparison with Shockley-Read-Hall recombination. *Semiconductor*, 38:946–949, 2004.
- [46] A. Luque, A. Martí, and C. Stanley. Understanding intermediate-band solar cells. *Nature Photonics*, 6:145–152, 2012.
- [47] N.F. Mott. Metal-insulator transition. *Rev.Mod. Phys.*, 40:677–683, 1968.
- [48] E. Antolin, A. Martí, J.Olea, D. Pastor, G. Gonzales-Diaz, I. Marti, and A. Luque. Lifetime recovery in ultrahighly titanium-doped silicon for the implementation of an intermediate band material. *Appl. Phys. Lett.*, 94:042115, 2009.
- [49] C.B. Murray, C.R. Kagan, and M.G. Bawendi. Synthesis and characterization of monodisperse nanocrystals and close-packed nanocrystal assemblies. *Annu. Rev. Mater. Sci.*, 30:545–610, 2000.
- [50] L.Cuadra, A. Martí, and A. Luque. Modeling of the absorption coefficient of the intermediate band solar cell. *Proceedings of the 16th European Photovoltaic Solar Energy Conference*, pages 15–21, 2000.
- [51] L.Cuadra, A. Martí, and A. Luque. *Proceedings of the Conferencia de Dispositivos Electronicos*, pages 193–196, 2001.

-
- [52] A. Martiⁱ, L. Cuadra, and A. Luque. Photovoltaics for the 21st century ii. *Proceedings of the International Symposium, The Electrochemical Society*, pages 46–90, 2001.
- [53] A. Luque, A. Marti, C. Stanley, N. Lopez, L. Cuadra, D. Zhou, J. L. Pearson, and A. McKee. General equivalent circuit for intermediate band devices: Potentials, current and electroluminescence. *J. Appl. Phys.*, 96:903, 2004.
- [54] D. Bimberg, M. Grudmann, and N.N. Ledentsov. Quantum dot heterostructures. 1999.
- [55] S.M. Hubbard, C.D. Cress, C.G. Bailey, R.P. Raffaele, S.G. Bailey, and D.M. Wilt. Effect of strain compensation on quantum dot enhanced gaas solar cells. *Appl. Phys. Lett.*, 92:123512, 2008.
- [56] R. Oshima, A. Takata, and Y. Okada. Strain-compensated InAs/GaNAs quantum dots for use in high-efficiency solar cells. *Appl. Phys. Lett.*, 93:083111, 2008.
- [57] Y. Okada, R. Oshima, and A. Takata. Characteristics of InAs/GaNAs strain-compensated quantum dot solar cell. *Jour. of Appl. Phys.*, 106:024306, 2009.
- [58] R. Krishnakumar, V. Subramanian, Y. Ramprakash, and A.S. Lakshmanan. thin film preparation by spray pyrolysis for solar cells. *Materials Chemistry and Physics*, 16:385–395, 2003.
- [59] P. Raja Ram, R. Thangaraj, and O.P. Agnihotri. Thin film CdZnSn/CuInSe₂ solar cells by spray pyrolysis. *Bull. Mater. Sci.*, 8(3):279–284, 1986.
- [60] J. Viguie and J. Spitz. Chemical vapor deposition at low temperatures. *Electrochem. Soc.*, 122(43):585–588, 1975.
- [61] D. Perednis and L. J. Gauckler. Thin film deposition using spray pyrolysis. *Journal of Electroceramics*, 14:103–111, 2005.
- [62] H.H. Afify, S.A. Nasser, and S.E. Demian. Influence of substrate temperature on the structural, optical and electrical properties of ZnO thin films prepared by spray pyrolysis. *J. Mater. Sci.: Materials in Electronics*, 2(3):152, 1991.
- [63] D.E. Bode and R.E. Thun G. Hass. Lead salt detectors. *Physics of Thin Films*, 3:275, 1966.

- [64] A.G. Stanley. Cadmium sulphide solar cells. *Applied Solid State Sciences*, 5:251, 1975.
- [65] G.B. Reddy, D.K. Pandya, and K. L Chopra. Solution grown (PbS)-(CdS) composite selective surfaces. *Sol. Energy Mater.*, 15:383, 1987.
- [66] C. Estrada-Gasca, G. Alvarez-Garcoa, R.E. Cabanillas, and P.K. Nair. Theoretical analysis of the thermal performance of all-glass evacuated tube solar collectors with absorber coating on the outside or inside of the inner tube. *Renewable Energy*, 2:477, 1992.
- [67] P.K. Nair, M.T.S. Nair, A. Fernandes, and M. Ocampo. Prospects of chemically deposited metal chalcogenide thin films for solar control applications. *J. Phys. D*, 22:829, 1989.
- [68]] C. Estrada-Gasca, G. Alvarez-Garcoa, and P.K. Nair. Theoretical analysis of the thermal performance of chemically deposited solar control coatings. *J. Phys. D*, 26:1304, 1993.
- [69] A.C. Boccara, D.Fournier, W. Jackson, and N.M. Amer. Sensitive in situ trace-gas detection by photothermal deflection spectroscopy. *Optics Letters*, 5:377–379, 1980.
- [70] G. Binning and H. Rohrer. The scanning tunneling microscope. *Sci.Am.*, 250:50, 1985.
- [71] D. Lincot, E.B. Yousfi, B. Canava, P. Cowache, and J.F. Guillemoles. Interfacial engineering of CuInGaSe₂ thin film solar cells based on atomic layer epitaxy. *Proc. 16th European Photovoltaic Sol. Energy Conf.*, 2000.
- [72] P.B. Garlick, M.J. Davies, D.J. Hearse, and T.F. Slater. Direct detection of free radicals in the reperfused rat heart using electron spin resonance spectroscopy. *Circulation Research*, 61:757–760, 1987.
- [73] A.H. Maki and B.R. McGarvey. Electron spin resonance in transition metal chelates. copper(II) bisacetylacetonate. *J. Chem. Phys.*, 29:31, 1958.
- [74] G.D. Watkins and J.W. Corbett. Defects in irradiated silicon. electron spin resonance of the si-a center. *Phys. Rev.*, 121:1001, 1961.
- [75] Bruker information note. what is epr? 2008.
- [76] Al.L. Efros and A.L. Efros. Interband absorption of light in a semiconductor sphere. *Sov. Phys. Semicond.*, 16(7):772–775, 1982.

-
- [77] A.I.Ekimov and A.A. Onushchenko. Quantum size effect in the optical spectra of semiconductor microcrystals. *Sov. Phys. Semicond.*, 16(7):775–778, 1982.
- [78] A.Henglein. Photochemistry of colloidal cadmium sulfide. *J. Phys. Chem.*, 86(13):2291–2293, 1982.
- [79] R.Rossetti, S. Nakahara, and L.E. Brus. Quantum size effects in the redox potentials, resonance raman spectra, and electronic spectra of CdS crystallites in aqueous solution. *J. Chem. Phys.*, 79(2):1086–1088, 1983.
- [80] C.B Murray, D.J. Norris, and M.G. Bawendi. Synthesis and characterization of nearly monodisperse CdE (E=S, Se, Te) semiconductor nanocrystallites. *J. Am. Chem. Soc.*, 115(19):8706, 1993.
- [81] S. Kudera, L. Carbone, L. Manna, and W.J. Parak. Growth mechanism, shape and composition control of semiconductor nanocrystals. *Semiconductor Nanocrystals Quantum Dots*, pages 1–34, 2008.
- [82] Y. Li, E. Chun, Y. Liu, N. Pickett, P.J. Skabara, S.S. Cummins, S. Ryley, A.J. Sutherland, and P. O’Brien. Synthesis and characterization of CdS quantum dots in polystyrene microbeads. *Journal of Materials Chemistry*, 15(12):1238–1243, 2005.
- [83] T. Tsuzuki and P.G. McCormick. Synthesis of CdS quantum dots by mechanochemical reaction. *Applied Physics A*, 65(6):607–609, 1997.
- [84] Z.A. Peng and X. Peng. Mechanisms of the shape evolution of CdSe nanocrystals. *Journal of the American Chemical Society*, 123(7):183–184, 2001.
- [85] X. Peng, L. Manna, W. Yang, J. Wickham, E. Scher, A. Kadavanich, and A.P. Alivisatos. Shape control of CdSe nanocrystals. *Nature*, 404:59–61, 2000.
- [86] A. Lipovskii, E. Kolobkova, V. Petrikov, I. Kang, A. Olkhovets, T. Krauss, M.Thomas, J. Silcox, F. Wise, Q. Shen, and S. Kycia. Synthesis and characterization of PbSe quantum dots in phosphate glass. *Applied Physics Letters*, 71:3406, 1997.
- [87] M.A. Hines and G.D. Scholes. Colloidal PbS nanocrystals with size-tunable near-infrared emission: Observation of post-synthesis self-narrowing of the particle size distribution. *Advanced Materials*, 15(21):1844, 2003.

- [88] C.B. Murray, S. Sun, W. Gaschler, H. Doyle, T.A. Betley, and C.R. Kagan. Colloidal synthesis of nanocrystals and nanocrystal superlattices. *IBM Journal of Research and Development*, 45(1):47–56, 2001.
- [89] S. Musikhin X.S. Zhao E.H. Sargent L. Bakueva, I. Gorelikov and E. Kumacheva. PbS quantum dots with stable efficient luminescence in the near-IR spectral range. *Advanced Materials*, 16(11):926–929, 2004.
- [90] M.V. Kovalenko, W. Heiss, E.V. Shevchenko, J.S. Lee, H. Schwinghammer, A.P. Alivisatos, and D.V. Talapin. SnTe nanocrystals: a new example of narrow-gap semiconductor quantum dots. *Journal of the American Chemical Society*, 129(37):11354–11355, 2007.
- [91] J. Ning, K. Men, G. Xiao, L. Wang, Q. Dai, B. Zou, B. Liu, and G. Zou. Facile synthesis of IV-VI SnS nanocrystals with shape and size control: nanoparticles, nanoflowers and amorphous nanosheets. *Nanoscale*, 2(9):1699–1703, 2010.
- [92] A.R.H.F. Ettema, R.A. de Groot, C. Haas, and T.S. Turner. Electronic structure of SnS deduced from photoelectron spectra and band-structure calculations. *Physical Review B*, 46(12):7363–7373, 1992.
- [93] M. El-Nahass, H.M. Zeyada, M.S. Aziz, and N.A. El-Ghamaz. Optical properties of thermally evaporated SnS thin films. *Optical Materials*, 20:159, 2002.
- [94] J.B. Johnson, H. Jones, B.S. Latham, J.D. Parker, R.D. Engelken, and C. Barbe. Optimization of photoconductivity in vacuum-evaporated tin sulphide thin films. *Semiconductor Science and Technology*, 14(6):501, 1999.
- [95] D.S. Koktysh, J.R. McBride, and S.J. Rosenthal. Synthesis of SnS nanocrystals by the solvothermal decomposition of a single source precursor. *Nanoscale Research Letters*, 2(3):144, 2007.
- [96] Y. Xu, N. Al-salim, C.W. Bumby, and R.D. Tilley. Synthesis of SnS quantum dots. *Journal of the American Chemical Society*, 131(44):15990, 2009.
- [97] X.L. Gou, J. Chen, and P.W. Shen. Synthesis, characterization and application of SnS_x (x=1,2) nanoparticles. *Mater.Chem. Phys.*, 93:557–556, 2005.
- [98] Y. Zhao, Z. Zhang, H. Dang, and W. Liu. Synthesis of tin sulfide nanoparticles by a modified solution dispersion method. *Materials science and engineering B*, 113:175–178, 2004.

-
- [99] G.H. Yue, L.S. Wang, X. Wang, Y.Z. Chen, and D.L. Peng. Characterization and optical properties of the single crystalline SnS nanowire arrays. *Nanoscale Research Letters*, 4(4):359, 2009.
- [100] A.M. Tripathi and S. Mitra. Tin sulfide (sns) nanorods: structural, optical and lithium storage property study. *RSC Adv.*, 4:10358–10366, 2014.
- [101] H. Liu, Y. Liu, Z. Wang, and P. He. Facile synthesis of monodisperse, size-tunable sns nanoparticles potentially for solar cell energy conversion. *Nanotechnology*, 21:105707, 2010.
- [102] Y. Nu, A. Al-Salim, and R.D. Tilley. Synthesis and size dependent reflectance study of water soluble sns nanoparticles. *Nanomaterials*, 28:54–64, 2012.
- [103] M. Shim, C. Wang, D.J. Norris, and P. Guyot-Sionnest. Doping and charging in colloidal semiconductor nanocrystals. *MRS Bulletin*, 26(12):1005–1008, 2001.
- [104] Y.C. Cao. Impurities enhance semiconductor nanocrystal performance. *Science*, 332:48–49, 2011.
- [105] D.J. Norris, A.L. Efros, and S.C. Erwin. Doped nanocrystals. *Science*, 319:1776–1779, 2008.
- [106] M. Shim and P. Guyot-Sionnest. n-type colloidal semiconductor nanocrystals. *Nature*, 407:981–983, 2000.
- [107] R.J. Clark and D.G. Cobbold. characterization of sulfur radical anions in solutions of alkali polysulfides in dimethylformamide and hexamethylphosphoramide and in solid state in ultramarine blue, green, and red. *Inorganic Chemistry*, 17:0020–1669, 1978.
- [108] H. Alexander. Hybrid passivated colloidal quantum dot solids. *Nature Nanotechnology*, 7:577, 2012.
- [109] M.A. Hines and P. Guyot-Sionnest. Synthesis and characterization of strongly luminescing ZnS-capped CdSe nanocrystals. *Journal of Physical Chemistry*, 100:468–471, 1996.
- [110] B. O. Dabbousi, J. RodriguezViejo, F. V. Mikulec, J. R. Heine, H. Matoussi, R. Ober, K. F. Jensen, and M. G. Bawendi. (CdSe)ZnS core-shell quantum dots: synthesis and characterization of a size series of highly luminescent nanocrystallites. *J. Phys. Chem. B*, 101(46):9463–9475, 1997.

- [111] X. G. Peng, M. C. Schlamp, A. V. Kadavanich, and A. P. Alivisatos. Epitaxial growth of highly luminescent CdSe/CdS core/shell nanocrystals with photostability and electronic accessibility. *J. Am. Chem. Soc.*, 119(30):7019–7029, 1997.
- [112] A. M. Abdel Haleem and M. Ichimura. Experimental determination of band offsets at the SnS/CdS and SnS /InS_xO_y heterojunctions. *J. Appl. Phys.*, 107:034507, 2010.
- [113] A. Mews, A. Eychmuller, M. Giersig, D. Schooss, and H. Weller. Preparation, characterization, and photophysics of the quantum dot quantum well system CdS/HgS/CdS. *J. Phys.Chem.*, 98(3):934–941, 1994.
- [114] D. Battaglia, J. J. Li, Y. J. Wang, and X. G. Peng. Colloidal two-dimensional systems: CdSe quantum shells and wells. *Angew. Chem. Int.*, 42(41):5035–5039, 2003.
- [115] X. H. Zhong, R. G. Xie, Y. Zhang, T. Basche, and W. Knoll. High-quality violet- to- red emitting ZnSe/CdSe core/shell nanocrystals. *Chem. Mater.*, 17(16):4038–4032, 2005.
- [116] P.Reiss, M. Protiere, and L.Li. Core-shell semiconductor nanocrystal. *Small*, 5(2):154–168, 2009.
- [117] M.A.M. Seyam. Optical and electrical properties of indium monosulfide (InS) thin films. *Vacuum*, 63:441–447, 2001.
- [118] K. Hara, K. Sayama, and H. Arakawa. Semiconductor sensitized solar cells based on nanocrystalline In₂S₃/In₂O₃ thin film electrodes. *Sol. Energy Mater. Sol. Cells*, 62(4):441–447, 2000.
- [119] J.L. Shay and B. Tell. Energy band structure of I-III-VI₂ semiconductors. *Surf. Sci.*, 37:748–762, 1973.
- [120] R.H. Bube and W.H. McCaroll. Photoconductivity in indium sulfide powders and crystals. *J. Phys. Chem. Solids*, 10:333, 1959.
- [121] S. Spiering, D. Hariskos, M., N. Naghavi, and D. Lincot. Cd free Cu(In,Ga)Se₂ thin film solar modules with indium sulfide buffer deposited by ALCVD. *Materials Research Society Spring Meeting*, B/PIII.01, 2002.
- [122] N. Barreau, J.C. Bernede, S. Marsillac, C. Amory, and W.N. Shafarman. New Cd free buffer layer deposited by PVD: In₂S₃ containing Na compounds. *Thin Solid Films*, 431–432:326–329, 2003.

-
- [123] S. Belgacem, M. Amlouk, and R. Bennaceur. Effet du rapport Cu/In sur la structure des couches minces de CuInS_2 airless spray. Application : conversion photovoltaïque. *Rev. Phys. Appl.*, 25:1213, 1990.
- [124] M.G. Sandoval-Paz, M. Sotelo-Lerma, J.J. Valenzuela-Jauregui, M. Flores-Acosta, and R. Ramirez-bon. Structural and optical studies on thermal-annealed In_2S_3 films prepared by the chemical bath deposition technique. *Thin Solid Films*, 472:5–10, 2005.
- [125] N. Kamoun, R. Bennaceur, and M. Amlouk. Optical properties of InS layers deposited using an airless spray technique. *Phys. Status solidi A*, 169:97–104, 1998.
- [126] A.N. MacInnes, W.M. Cleaver, A.R. Barron, M.B. Power, and A.F. Hepp. Metal-organic chemical vapor deposition of polycrystalline tetragonal indium sulphide (InS) thin films. *Adv. Mater. Opt. Electronic*, 1:229, 1992.
- [127] N. Bouguila, H. Bouzouita, E. Lacaze, A. BelHadj Amara, H. Bouchriha, and A. Dhouib. Effet de la temperature de fabrication sur les proprietes structurales et morphologiques des couches epaisses de In_2S_3 "spray". *J. Physocque III*, 7:1647, 1997.
- [128] T. Asikainen, M. Ritila, and M. Leskela. Growth of In_2S_3 thin films by atomic layer epitaxy. *Appl. Surf. Sci.*, 82/83:122, 1994.
- [129] N. Naghavi, R. Henriquez, V. Laptev, and D. Lincot. Growth studies and characterization of In_2S_3 thin films deposited by atomic layer deposition. *Appl. Surf. Sci.*, 222:65, 2004.
- [130] J. George, K.S. Joseph, B. Prodeep, and T.I. Palson. Reactively evaporated films of indium sulphide. *Phys. Status Solidi, A Appl. Res.*, 106(1):123, 1988.
- [131] A. Timoumi, H. Bouzouita, M. Kanzari, and B. Rezig. Fabrication and characterization of In_2S_3 thin films deposited by thermal evaporation technique. *Thin Solid Films*, 480–481:124–128, 2005.
- [132] C. Guillen, T. Garico, J. Herrero, M.T. Gutierrez, and F. Briones. Tailoring growth conditions for modulated flux deposition of In_2S_3 thin films. *Thin Solid Films*, 451–452:112–115, 2004.
- [133] R. Diehl and R. Nitsche. Vapour growth of three In_2S_3 modifications by iodine transport. *J. Cryst. Growth*, 28:306, 1975.
- [134] G.Binnig, C.F. Quate, and C.Gerber. Atomic force microscope. *Physical Review Letters*, 56(9):930–933, 1986.

- [135] R.A. Wilson and H. Bullen. Introduction to scanning probe microscope. <http://asdlab.org/onlineArticles/ecourseware/Bullen/SPMModuleBasicTheoryAFM.pdf>.
- [136] N.Jalili and K.Laxminarayana. A review of atomic force microscopy imaging systems: application to molecular metrology and biological sciences. *Mechatronics*, 14:907–945, 2004.
- [137] A. Luque, A. Marti, and A.J. Nozik. Solar cells based on quantum dots: Multiple exciton generation and intermediate bands. *MRS bull.*, 32:236, 2007.
- [138] L. Zhuang, L. Guo, and S.Y. Chou. Silicon single-electron quantum-dot transistor switch operation at room temperature. *Appl. Phys. Lett.*, 72:1205, 1998.
- [139] B.Rezek, J. Stuchlik, A. Fejfar, and J. Kocka. Microcrystalline silicon thin films studied by atomic force microscopy with electrical current detection. *J.Appl.Phys.*, 92:587–593, 2002.
- [140] S. Richter, M. Geva, J. P. Garno, and R. N. Kleiman. Metal-insulator-semiconductor tunneling microscope:two-dimensional dopant profiling of semiconductors with conduction atomic-force microscopy. *Appl. Phys. Lett.*, 77:456, 2000.
- [141] D. Xu, G. D. Watt, J. N. Harb, and R. C. Davis. Electrical conductivity of ferritin proteins by conductive afm. *Nano Lett.*, 5:571, 2005.
- [142] P. De Wolf, E. Brazel, and A. Erickson. Electrical characterization of semiconductor materials and devices using scanning probe microscopy. *Mater. Sci. Semicond. Process.*, 4:71, 2001.
- [143] C. Li, S. Minne, B. Pittenger, A. Mednick, M. Guide, and T.Q. Nguyen. *Bruker Application Note AN132*, 2011.
- [144] V. Yanev, and A. J. Bauer T. Erlbacher, and M. Rommel, and L. Frey. Comparative study between conventional macroscopic iv techniques and advanced afm based methods for electrical characterization of dielectrics at the nanoscale. *Microelectron. Eng.*, 86:1911, 2009.
- [145] L. Huang and C. Su. A torsional resonance mode afm for in-plane tip surface interactions. *Ultramicroscopy*, 100:277, 2003.
- [146] L. Huang and C. Su. Torsional resonance mode imaging for high-speed atomic force microscopy. *AIP Conf. Proc.*, 696:357–364, 2003.

-
- [147] C. Su, L. Huang, P. Neilson, and V. Kelley. In-situ measurements of in-plane and out-of-plane force gradient with a torsional resonance mode afm. *Proc. 12th Int. Conf. on Scanning Tunneling Microscopy/Spectroscopy and Related Techniques*, page 349, 2003.
- [148] C. Yang and I. Hwang. Soft-contact imaging in liquid with frequency-modulation torsion resonance mode atomic force microscopy. *Nanotechnology*, 21:065710, 2010.
- [149] P. Harris, L. Huang, and C. Su. *Bruker application note AN107*, 2007.
- [150] D. Stievenard and B. Legrand. Silicon surface nano-oxidation using scanning probe microscopy. *Prog.Surf.Sci.*, 82:112–140, 2006.
- [151] A.Vetushka, A. Fejfar, M. Ledinski, B. Rezek, J. Stuchlik, and J. Kocka. Comment on current routes in hydrogenated microcrystalline silicon. *Physical Review B*, 81:237301, 2010.
- [152] I. Horcas, R. Fernandez, M. Gomez Rodriguez, J. Colchero, J. Gomez Herrero, and A. M. Baroa. WPSXM: A software for scanning probe microscopy and a tool for nanotechnology. *Rev. Sci. Instrum.*, 78:013705, 2007.
- [153] S.B. Kaemmer. *Bruker Application Note 133*, 2011.
- [154] P. Trtik, J. Kaufmann, and U. Volz. On the use of peak-force tapping atomic force microscopy for quantification of the local elastic modulus in hardened cement paste. *Cement and Concrete Research*, 42:215–221, 2012.
- [155] D. Stiervenard and B. Legrand. Silicon surface nano oxidation using scanning probe microscopy. *Prog. Surf. Sci.*, 81:112, 2006.
- [156] S. Niki, M. Contreras, I. Repins, M. Powalla, K. Kushiya, S. Ishizuka, and K. Matsubara. CIGS absorbers processes. *Prog. Photovolt: Res. Appl.*, 18(6):453–466, 2010.
- [157] I. Repins, M.A. Contreras, B. Egaas, C. DeHart, J. Scharf, and B.To C.L. Perkins, and R. Noufi. 19.9% efficient ZnO/CdS/CuInGaSe₂ solar cell with 81-2% fill factor. *Progress in Photovoltaics: Research and Applications*, 11(4):225–230, 2003.
- [158] K. Ramanathan, M.A. Contreras, C.L. Perkins, S. Asher, F.S. Haseen, and M. Romero and W. Metzger J. Keane, and D. Young, R. Noufi, J. Ward, and A. Dudai. Properties of 19.2% efficiency

- ZnO/CdS/CuInGaSe₂ thin film solar cells. *Progress in Photovoltaics: Research and Applications*, 16(3):235–239, 2008.
- [159] W. Li, Y. Sun, W. Liu, and L. Zhou. Fabrication of Cu(In,Ga)Se₂ thin films solar cell by selenization process with Se vapor. *Solar cells and solar energy materials*, 80(2):191–195, 2004.
- [160] A.O. Pudov. Impact of secondary barriers on CuIn_{1-x}Ga_xSe₂ solar cell operation. *PhD thesis-Colorado State University*, 2005.
- [161] W. Witte, S. Spiering, and D. Hariskos. Substitution of the cds buffer layer in cigs thin-film solar cells. *Dunne Schichten*, 26:23–27, 2014.
- [162] D. Hariskos, S. Spiering, and M. Powalla. Buffer layers in Cu(In,Ga)Se₂ solar cells and modules. *Thin Solid Films*, 480–481:99–109, 2004.
- [163] N. Naghavi, S. Spiering, M. Pwalla, B. Cavana, and D. Lincota. High-efficiency copper indium gallium diselenide (CIGS) solar cells with indium sulfide buffer layers deposited by atomic layer chemical vapor deposition (ALCVD). *Progress in Photovoltaics*, 11(7):437–443, 2003.
- [164] I.Oja, M.Nanu, A. Katerski, M. Krunks, A.Mere, J.Raudoja, and A. Goossens. Crystal quality studies of CuInS₂ films prepared by spray pyrolysis. *Thin Solid Film*, 480:82–86, 2005.
- [165] A. Goossens and J. Hofuis. Spray-deposited CuInS₂ solar cells. *Nanotechnology*, 19:424018, 2008.
- [166] J.C.C.Fan. Theoretical temperature dependence of solar cell parameters. *Solar Cells*, 17:309–315, 1986.
- [167] M.A. Green. General temperature dependence of solar cell performance and implications for device modelling. *Progress in Photovoltaics: Research and applications*, 11:333–340, 2003.
- [168] M.I. Hossain, P.A. Chelvanathan, M. Zaman, M.R. Karim, M.A. Alghoul, and N. Amin. Prospects of indium sulphide as an alternative to cadmium sulphide buffer layer in CIS base solar cells from numerical analysis. *halcogenide Letters*, 8:315–324, 2011.
- [169] C. Xue, S. Varlamov, J. Huang, and Kunz O. Influence of emitter doping and thickness on the performance of n-type evaporated poly-si-thin film solar cells on glass. *Proceedings of the 50th Annual Conference, Australian Solar energy Society*, 2012.

- [170] F. Daume, S. Puttnins, C. Scheit, H. Zachmann, A. Rahm, A. Braun, and M. Grundmann. Damp heat treatment of Cu(In,Ga)Se₂ solar cells with different sodium content. *Materials*, 6:5478–5489, 2013.

Summary

To make photovoltaics (PV) a competitive energy source it is essential to reduce the production cost and increase the efficiency, overcoming the Shockley–Queisser limit. To reduce the price of PV modules, thin film technology (2nd-generation PV) has been developed. By means of this technology a smaller quantity of active material is used, thus reducing the material costs. One of the proposed approaches for going beyond the Shockley–Queisser energy conversion limit is the intermediate band (IB) solar cell, in which the presence of an intermediate band within the p-n junction photons to be absorbed with energy less than the band gap. It has been calculated that this could theoretically allow one to achieve an efficiency of 63.2% at maximum light concentration. This thesis is focused on the concept of the intermediate band solar cell to boost the efficiency of copper indium gallium diselenide/disulphide (CI(G)S) solar cells. There are two important requirements to the IB; (1) the IB does not behave as a recombination band, with the consequence that the wave-function of electrons must be delocalized, and (2) it has to be half-filled with electrons. Quantum Dots (QD) are the best candidates for creating an IB because they can fulfill the abovementioned criteria. Indeed, by controlling the dot size and the dot spacing it is possible to create a delocalized energy band with the desired fine-tuned band energy. Moreover, appropriate doping of QDs guarantees that the IB is half-filled with electrons. Tin sulfide (SnS) semiconductor material, studied in this thesis, is a perfect material for creating an intermediate band semiconductor. The advantage of using this material is that both tin and sulfur are non-toxic and earth-abundant, in addition to their advantageous optical properties.

In this thesis, SnS quantum dots are first synthesized and analyzed, then SnS/In₂S₃ core shell nanodots are investigated and, finally, these particles are embedded in a CIS solar cell. The feasibility of an IB solar cell with such QD boosters is then determined. A spray synthesis process to produce SnS QDs was developed using a colloidal route. SnCl₂ mixed with triethanolamine (TEA) and sodium sulphide were used as precursors; both precursors were

dissolved in ethylene glycol. To avoid clustering of the QDs, trioctylphosphine oxide (TOPO) was added to the first precursor. Characterization of these nanoparticles was carried out by means of various techniques for studying their optical and structural properties. High resolution transmission electron microscopy (HRTEM) measurements showed that these SnS nanoparticles are crystalline spherical dots with a diameter of 4 ± 2 nm, less than the Bohr radius, which should lead to quantum behavior. X-ray spectroscopy confirmed that the material is indeed the SnS alloy, since the ratio between S and Sn is 1:1. The optical absorption was investigated by means of two different techniques: UV/VIS spectroscopy and photothermal deflection spectroscopy (PDS), both techniques showed that band gap is around 1.6 eV, confirming the QD dimension of the particles. Moreover, the presence of two absorption peaks in the infrared region led us to suspect that during the synthesis an electron was transferred into the SnS QD, thereby showing its doping nature. Electron spin resonance spectroscopy of this material also revealed the presence of a free electron, confirming our hypothesis of electron transfer.

A possible doping mechanism involves the sodium present in the precursor. A Na^+ ion can attach to the QD and induce a free electron at the Lowest Unoccupied Quantum-Confined Orbital (LUQCO). In this process the sulfur is thought to act as an anion or radical anion and delivers the electron. However, direct experimental identification of the dopant species or their location has been very hard. Nanoparticles of two different sizes were investigated. It was found that nanoparticles with a size of 2 nm behave as perfect semiconductor quantum dots, showing a clear band gap. In contrast, the nanoparticles with a size of 4 nm show no band gap, a behavior similar to metals.

Afterwards, the SnS nanoparticles were spray-deposited as thin film and tested in order to verify whether they maintain their properties.

The next step was to cap the SnS QDs to improve their electronic properties. Ligands play a crucial role in controlling the size of nanoparticles and passivating their surfaces. However, incomplete passivation by ligands leads to trap states at the surface that act as recombination centers. A better approach is to replace the ligands with a shell made of another semiconductor material, creating a core-shell structure. To that end, In_2S_3 was chosen as a capping material because of its appropriate band gap and semiconducting properties, with respect to the core SnS material. In this work, the synthesis of SnS/ In_2S_3 core-shell nanoparticles by chemical bath deposition (CBD) process was developed. An ethanol dispersion of previously synthesized TOPO capped SnS NPs was immersed in the CBD for the deposition of In_2S_3 shell. Then, the coated nanoparticles were separated and washed in ethanol. Characterization of the structure and the optical properties of these core-shell nanoparticles was carried out by means of different techniques. The TEM and HRTEM images

showed spherical nanoparticles with a size of around 10 nm with a crystalline core surrounded by an amorphous shell. The band gap of these nanoparticles is higher than that of SnS NPs, and it is shown that the band gap can be tailored by changing the thickness of the shell. Core-shell NPs were deposited on glass substrates as thin film, using the spraying techniques, with different number of sprays and thus, different thicknesses. The morphology of these films was analyzed using atomic force microscopy (AFM) and scanning electron microscopy (SEM). Both methods showed these thin films to be very rough. The optical properties of the films with different thicknesses were analyzed, from which information on the band gap was obtained. The films made using a small number of sprays have band gaps similar to In_2S_3 thin film; the layers made with a higher number of sprays are closer to the SnS thin film. For solar cell applications it is extremely important to study the dark and photoconductivity in order to determine the charge transport in the material, the photosensitivity (photoconductivity/dark conductivity) and the activation energy of the materials. All samples in this study showed adequate photosensitivities in excess of 10^5 . Subsequently, SnS NPs were embedded between two In_2S_3 layers.

In order to assess the feasibility of utilizing nanoparticles in electronic devices such as solar cells, it is important to study electrical properties of individual particles. For this purpose two different types of AFM techniques, torsional resonance tunneling AFM (TR-TUNA) and peak force AFM (PF-AFM), were used to investigate the topography and local conductivity of SnS and SnS/ In_2S_3 core-shell nanoparticles. By means of TR-TUNA it was possible to obtain the topography and conductivity maps of the core-shell nanoparticles, but it was not possible to study SnS nanoparticles. This is due to the presence of TOPO, which does not allow the tip to approach the particles properly, disturbing the measurements. To overcome this problem PF-AFM was used. As expected, this mode also allows one to map SnS capped with TOPO, detecting the size and the current of single SnS nanoparticles with a single measurement. These two studies confirmed that both the core and the shell are conductive and that the charge transport across the core/shell interface can in principle take place without hindrance.

After optimizing the synthesis and having studied the properties of SnS and SnS/ In_2S_3 core-shell NPs, both types of nanoparticles were embedded in CIS and CIGS solar cells. The CIS cells used in this work have a different configuration than the standard CIS cells. They are made using the “superstrate” configuration: with In_2S_3 instead of CdS as buffer layer, TiO_2 instead of an i-ZnO buffer layer, and the cells are made mainly by the spraying technique. First, this superstrate type of CIS cells were optimized, during which the advantage of depositing two layers of TiO_2 and three thin layers of CIS with copper gradient was established. Afterwards, SnS nanoparticles and SnS/ In_2S_3 core-shell

nanoparticles were embedded in CIS cells, testing two configurations: (i) SnS nanoparticles embedded between the n- and the p-layer of the cell structure and (ii) sandwiched between two In_2S_3 layers. Similarly, cells with In_2S_3 /SnS core-shell nanoparticles embedded between two In_2S_3 layers were produced. All solar cells were investigated using current-voltage (I-V) measurement using the AM1.5 spectrum from a solar simulator. The solar cell with embedded core-shell nanoparticles showed the best performance, with an efficiency of 0.6%. In order to understand the charge transport mechanism in the cells, the light intensity dependent I-V characteristics were investigated. These measurements showed that the photocurrent changes with light intensity, while no evident changes occur in open circuit voltage. Moreover, the temperature dependence of the I-V characteristics was studied to check whether any permanent structural change is taking place due to annealing. From these measurements, no noticeable change was found. From this it is inferred that no reconstruction of the structure is taking place. In the end, SnS nanoparticles were embedded in CIGS solar cells. The CIGS absorber layer was deposited using the co-evaporation technique at the TNO/Eindhoven laboratory. The cells were completed using In_2S_3 as a buffer layer. Two different types of cells were compared for I-V characteristics and spectral response measurements: (1) a CIGS cell used as reference and (2) the same type of cell with SnS nanoparticles embedded between two In_2S_3 layers. From these measurements it is evident that SnS nanoparticles embedded in the cell do not improve the current, but the open circuit voltage was comparable to that of the reference CIGS cell. This result implies that, in the present configuration, electronic states of these nanoparticles do not act as an intermediate band. They act as a diffusion barrier, improving the V_{oc} . These cells showed positive aging effect. The I-V curves, after storing the cells for two days, showed an increase in current and hence, efficiency.

The results presented in this thesis contribute to a better understanding of SnS nanoparticles and to the development of a new core-shell structure: SnS/ In_2S_3 core-shell nanoparticles. In addition to the standard methods used to characterize nanoparticles, such as Transmission Electron Microscopy and UV/VIS absorption measurements, two new AFM techniques were used. TR-TUNA and PF-AFM measurements were conducted on both SnS and SnS/ In_2S_3 nanoparticles, allowing a complete investigation of the morphology and conductivity of a single nanoparticle with only one measurement. Finally, preliminary studies were carried out on SnS and SnS/ In_2S_3 core-shell nanoparticles embedded in CIS and CIGS solar cells. The results showed the limit and the potential of nanoparticles for solar cell applications. Using this cell design the quantum dots do not form an intermediate band but it seems that they act as a diffusion barrier, improving the V_{oc} of the solar cells.

Samenvatting

Om fotovoltaïsche (PV) toepassingen een concurrerende energiebron te laten zijn, is het essentieel dat de productiekosten worden verlaagd en het rendement wordt verhoogd door de Shockley-Queisser limiet te verbreken. Dunne film technologie (2e generatie PV) is ontwikkeld met als doel om de prijs van PV modules te verlagen. Met deze technologie wordt een kleinere hoeveelheid materiaal gebruikt waardoor de kosten worden verlaagd. Een van de mogelijkheden voor het verbreken van de Shockley-Queisser limiet voor energieomzetting is de tussen-bandkloof (TB) zonnecel waarbij er zich binnen de pn-overgang een tussenliggende energieband bevindt, die het mogelijk maakt om fotonen met een energie die kleiner is dan de bandkloof te absorberen. Berekeningen laten zien dat hiermee in theorie een rendement van 63,2% kan worden bereikt bij maximale lichtconcentratie. Dit proefschrift richt zich op het concept van de tussen-bandkloof zonnecel met als doel om het rendement van koper-indium-gallium-diselenide/difluorsulfide (CI(G)S) zonnecellen te verhogen. Er zijn twee vereisten voor de TB; (1) de TB gedraagt zich niet als recombinatiecentrum, wat inhoudt dat de golf functie van elektronen gedelokaliseerd moet zijn en (2) de TB moet voor de helft met elektronen zijn gevuld. Kwantumdots (KDs) zijn de beste kandidaat voor het creëren van een TB, omdat deze aan beide bovengenoemde criteria kunnen voldoen. Bovendien kan de juiste dotering ervoor zorgen dat de TB voor de helft met elektronen is gevuld.

De halfgeleider tinsulfide (SnS), die in dit proefschrift wordt beschouwd, is een uitstekend materiaal om een tussen-bandkloof halfgeleider te creëren. Naast de gunstige optische eigenschappen van deze halfgeleider, is zowel tin als zwavel niet giftig en komen ze in grote hoeveelheden op aarde voor. In dit proefschrift wordt eerst de synthese en vervolgens de analyse van SnS KDs beschreven. Vervolgens worden $\text{SnS}/\text{In}_2\text{S}_3$ kern-schil nanodots bestudeerd en uiteindelijk worden deze deeltjes bij een CIS zonnecel ingebouwd. Hierbij wordt ook de uitvoerbaarheid van een TB zonnecel met dergelijke prestatie verbeterende KDs beschouwd. Gebruik makend van colloïden, is een stuifsynthese ontwikkeld om SnS KDs te fabriceren. Als precursor is een mix van SnCl_2 en

tri-ethanolamine (TEA) en natriumsulfide gebruikt; beiden opgelost in ethyleenglycol. Om er voor te zorgen dat de KDs niet samenklonteren, is er trioctylfosfineoxide (TOPO) toegevoegd aan de eerstgenoemde precursor. De karakterisering van de nanodeeltjes is uitgevoerd met behulp van verschillende technieken waarmee de optische en materiaaleigenschappen kunnen worden bepaald. Hoge resolutie transmissie elektronenmicroscopie (HRTEM) metingen tonen aan dat de SnS nanodeeltjes kristallijn en bolvormig zijn en een diameter hebben van 4 ± 2 nm. De diameter is kleiner dan de Bohrstraal, wat leidt tot kwantumgedrag. Metingen met röntgenspectroscopie hebben bevestigd dat het hier inderdaad om de SnS legering gaat, aangezien de verhouding tussen S en Sn 1:1 is. De optische absorptie is gemeten met twee verschillende technieken: UV/VIS spectroscopie en fothermische deflectie spectroscopie (PDS). Beide technieken laten zien dat de bandkloof ongeveer 1.6 eV is, wat de dimensies van de KDs bevestigt. Bovendien doet de aanwezigheid van twee absorptiepieken het infraroodgebied ons vermoeden dat er gedurende de synthese een elektron in de SnS KDs is verplaatst, wat wijst op dotering van de KDs. Elektronspinresonantie van dit materiaal heeft ook de aanwezigheid van een vrij elektron aangetoond, wat onze hypothese van de verplaatsing van het elektron bevestigt.

Een mogelijk doping mechanisme heeft betrekking op de in de precursor aanwezige natrium. Een Na^+ ion kan een verbinding aangaan met de nanodeeltje met als gevolg een vrij elektron in de laagst beschikbare energietoestand. Tijdens dit proces gedraagt het zwavelatoom zich als reductor. Echter, een directe experimentele waarneming van de doping deeltjes en hun positie is een grote uitdaging. In dit proefschrift heb ik twee verschillende afmetingen van nanodeeltjes onderzocht. Een conclusie uit dit werk is dat nanodeeltjes van 2 nm zich gedragen als perfecte halfgeleider quantum dots, met een duidelijke bandgap. Echter, de nanodeeltjes van 4 nm vertonen geen bandgap en gedragen zich als metaal.

Naderhand zijn de SnS nanodeeltjes als dunne film gedeponeerd door middel van stuifsynthese en zijn deze getest om vast te stellen of de eigenschappen zijn behouden.

De volgende stap was het inkapselen van de SnS KDs om hun elektrische eigenschappen te verbeteren. Liganden spelen een cruciale rol bij het controleren van de grootte van de nanodeeltjes en bij de passivering van hun oppervlak. Echter, onvolledige inkapseling door liganden leidt tot elektronval toestanden aan het oppervlak waar recombinatie plaats kan vinden. Een betere benadering is het vervangen van de liganden door een schil die is gemaakt van een andere halfgeleider, om zo een kern-schil structuur te vormen. Om dat te bereiken is In_2S_3 gekozen als schilmateriaal, omdat dit materiaal in vergelijking met SnS zowel een geschikte bandkloof alsook geschikte andere eigenschappen bezit. In dit werk is de synthese van SnS/ In_2S_3 kern-schil nanodeeltjes via het

chemische bad-depositie proces (CBD) ontwikkeld. Een ethanoldispersie van eerder gefabriceerde door TOPO omringde SnS nanodeeltjes is ondergedompeld in de CBD opstelling voor de depositie van de In_2S_3 schil. Daarna zijn de bedekte nanodeeltjes gescheiden en gewassen in ethanol. De karakterisering van de structuur en de optische eigenschappen van de kern-schil nanodeeltjes is uitgevoerd met behulp van verschillende technieken. De TEM en HRTEM afbeeldingen laten zien dat de nanodeeltjes een grootte van 10 nm hebben met een kristallijne kern, omringd door een amorfe schil. De bandkloof van deze nanodeeltjes is groter dan die van SnS nanodeeltjes en we hebben laten zien dat de bandkloof kan worden aangepast door de dikte van de schil te veranderen. De Kern-schil nanodeeltjes zijn gedeponerd als een dunne film op substraten van glas door gebruik te maken van stuiftechnieken waarbij een verschillend aantal verstuivingen is gebruikt, wat resulteert in verschillende filmdikten. De morfologie van deze films is geanalyseerd door atoomkrachtmicroscopie (AFM) rasterelektronenmicroscopie (SEM). Beide metingen hebben aangetoond dat de films een grote ruwheid hebben. De optische eigenschappen van films met verschillende dikten is geanalyseerd, waarbij de informatie over de bandkloof is verkregen. De films die met een klein aantal verstuivingen zijn gemaakt, hebben een bandkloof die vergelijkbaar is met die van een In_2S_3 dunne film; de lagen die met een groter aantal verstuivingen zijn gemaakt lijken meer op een SnS film.

Voor zonneceltoepassingen is het erg belangrijk om de donker- en lichtgeleiding te bestuderen, om zo het landingstransport, de lichtgevoeligheid (geleiding onder belichting gedeeld door donkergeleiding) en de activeringsenergie van de materialen te bepalen. Alle materialen in deze studie vertonen een geschikte lichtgevoeligheid van boven de 10^5 . Vervolgens zijn de nanodeeltjes ingebouwd tussen twee In_2S_3 lagen. Om de geschiktheid van het gebruik van deze nanodeeltjes in elektronische toepassingen zoals zonnecellen te onderzoeken, is het belangrijk om de elektrische eigenschappen van individuele deeltjes te bestuderen. Met dit doel zijn er twee verschillende AFM technieken gebruikt: torsieresonantie-tunneling AFM (TR-TUNA) en piekkracht AFM (PF-AFM). Hiermee is de topografie en de lokale geleiding van SnS en SnSn/ In_2S_3 kern-schil nanodeeltjes bestudeerd. Door gebruik te maken van TR-TUNA was het mogelijk om een kaartafbeelding van de topografie en de geleiding van de nanodeeltjes te maken. Het was echter niet mogelijk om de SnS nanodeeltjes met deze methode te onderzoeken. Dit werd veroorzaakt door de aanwezigheid van TOPO wat ervoor zorgde dat de AFM-tip de deeltjes niet voldoende kon naderen. Om dit probleem te verhelpen is er PF-AFM gebruikt. Zoals verwacht, is het met deze meetmodus wél mogelijk om ook de door TOPO omringde SnS met een enkele meting in kaart te brengen en om zowel de afmetingen als de stroom van individuele SnS nanodeeltjes te detecteren. Deze twee studies be-

vestigen dat zowel de kern als de schil geleidend zijn en dat het ladingstransport door het kern/schil-oppervlak in principe zonder belemmering plaatsvindt.

Nadat de synthese is geoptimaliseerd en de eigenschappen van de SnS en SnS/In₂S₃ kern-schil nanodeeltjes zijn bestudeerd, zijn beide typen nanodeeltjes ingebracht in CIS en CIGS zonnecellen. De CIS cellen die zijn gebruikt in dit werk hebben een andere configuratie dan de standaard CIS cellen; ze zijn gemaakt door gebruik te maken van de “superstraat”-configuratie, door een In₂S₃ in plaats van CdS bufferlaag en een TiO₂ in plaats van een i-ZnO bufferlaag te gebruiken en de cellen zijn hoofdzakelijk door verstuuving gefabriceerd. Allereerst is dit type van superstraat CIS cellen geoptimaliseerd waarbij het voordeel van het deponeren van twee TiO₂ lagen en drie CIS lagen met een koper gradiënt naar voren komt. Daarna zijn de SnS nanodeeltjes en de SnS/In₂S₃ kern-schil nanodeeltjes ingebracht in CIS cellen, waarbij twee configuraties zijn getest: (i) SnS nanodeeltjes ingebracht tussen de n- en de p-laag van de celstructuur en (ii) ingeklemd tussen twee In₂S₃ lagen. Op vergelijkbare wijze zijn cellen met SnS/In₂S₃ kern-schil nanodeeltjes ingebouwd tussen twee In₂S₃ lagen gefabriceerd. Alle zonnecellen zijn bestudeerd met stroomspanning (I-V) metingen onder een AM1.5 spectrum uit een zonn simulator. De zonnecel met ingebouwde kern-schil nanodeeltjes met de ingeklemde kern-schil nanodeeltjes lieten met een rendement van 0.6% de beste prestaties zien. Om het mechanisme van het ladingstransport te begrijpen, zijn de lichtintensiteit afhankelijke I-V karakteristieken bestudeerd. Deze metingen laten zien dat de stroom onder belichting verandert met de lichtintensiteit, maar dat er geen duidelijke verandering is te zien in de open-klemspanning (V_{oc}). Ook is de temperatuursafhankelijkheid van de I-V karakteristiek gemeten om vast te stellen of er permanente verandering plaats heeft gevonden vanwege de verhitting. Deze metingen laten zien dat er geen significante verandering heeft plaatsgevonden. Hieruit maken we op dat er geen verandering van de structuur plaats heeft gevonden. Tenslotte zijn er SnS nanodeeltjes ingebouwd in CIGS zonnecellen. De absorberende laag van de CIGS cel is gedeponerd met behulp van de co-verdamping techniek op het TNO/Eindhoven laboratorium. De cellen zijn voltooid door gebruik te maken van een In₂S₃ bufferlaag. Van de twee verschillende typen cellen zijn de I-V karakteristieken en de spectrale respons metingen vergeleken: (1) een CIGS cel die gebruikt wordt als referentie en (2) een zelfde type cel met SnS nanodeeltjes ingebracht tussen twee In₂S₃ lagen. Uit deze metingen blijkt dat SnS nanodeeltjes in vergelijking met de referentie CIGS cel niet de stroom verbeteren maar juist de open-klemspanning verbeteren. Dit resultaat wijst erop dat de elektronentoestanden van de gebruikte nanodeeltjes in de huidige configuratie niet werken als een tussenband. In plaats daarvan vormen ze een diffusiebarrière die de V_{oc} verbetert. Deze cellen tonen een positief verouderingseffect. De I-V curves na het voor twee

dagen opbergen van de cellen tonen een verhoging van de stroom en daarmee een verhoging van het rendement.

De resultaten die in dit proefschrift zijn gepresenteerd dragen bij tot een verbeterd begrip van SnS nanodeeltjes en aan de ontwikkeling van een nieuwe kern-schilstructuur met SnS/In₂S₃ kern-schil nanodeeltjes. Ook zijn er als aanvulling op de standaard karakterisatietechnieken, zoals transmissie elektronenmicroscopy en UV/VIS absorptiemetingen, twee nieuwe AFM technieken gebruikt. TR-TUNA en PF-AFM metingen zijn uitgevoerd op zowel SnS als SnS/In₂S₃ nanodeeltjes, wat het mogelijk maakt om met een enkele meting een volledige studie uit te voeren naar de morfologie en de geleiding van een individueel nanodeeltje. Als laatst is er een begin gemaakt met onderzoek naar SnS en SnS/ In₂S₃ kern-schil nanodeeltjes, ingebouwd in CIS en CIGS zonnecellen. De resultaten hiervan tonen de beperkingen en de potentiële mogelijkheden van nanodeeltjes voor toepassingen in zonnecellen.

In het huidige celontwerp functioneren de kwantumdeeltjes niet als tussenliggende energieband, maar lijken een diffusiebarrière te vormen die de V_{oc} van de cellen verbetert.

List of Publications

Caterina Prastani, Marius Nanu, Diana E. Nanu, Ruud E.I. Schropp and Jatindra K. Rath. *Synthesis of SnS/In₂S₃ core-shell nanoparticles*. Chemical Physics Letters **612**, 306–308 (2014). [Editor Choice]

Jatindra K. Rath, **Caterina Prastani**, Diana E.Nanu, Marius Nanu, Ruud E.I.Schropp, Aliaksei Vetushka, Matěj Hývl and Antonin Fejfar. *Fabrication of SnS quantum dots for solar-cell applications: Issue of capping and doping*. Physica Status Solidi (b) **251**, 1309–1321 (2014). [Cover Publication]

Caterina Prastani, Marius Nanu, Diana E. Nanu, Ruud E.I. Schropp and Jatindra K. Rath. *Development of SnS/In₂S₃ core-shell nanoparticles for solar cell application*. Photovoltaic Specialists Conference (39th IEEE PVSC), 2452–2455 (2013).

Caterina Prastani, Aliaksei Vetushka, Matěj Hývl, Antonin Fejfar, Marius Nanu, Diana E.Nanu, Ruud E.I.Schropp and Jatindra K. Rath . *Conductivity measurement of individual SnS nanoparticles by Peak Force AFM*. Mater. Res. Soc. Symp. Proc. **1557** DOI: 10.1557/opl.2013.1108.

Caterina Prastani, Marius Nanu, Diana E. Nanu, Jatindra K. Rath and Ruud E.I. Schropp. *Synthesis and conductivity mapping of SnS quantum dots for photovoltaic applications*. Materials Science and Engineering B **178**, 656–659 (2013).

Caterina Prastani, Aliaksei Vetushka, Antonin Fejfar, Marius Nanu, Diana E.Nanu, Jatindra K. Rath and Ruud E.I.Schropp. *Conductivity mapping of nanoparticles by torsional resonance tunneling atomic force microscopy*. Appl. Phys. Lett. **101**, 083107 (2012).

Caterina Prastani, Cecile Saguy, Oleksandr Astakhov, Marius Nanu, Diana E.Nanu, Ruud E.I.Schropp and Jatindra K. Rath. *Doping of nanoparticles*. (to be submitted)

Acknowledgments

The last years have been very important for me from professional and personal point of view. My PhD journey was a stimulating experience and I got an opportunity to meet different people from whom I learnt a lot.

First, I want to thank Prof. Schropp who allowed me to be a part of the group and helped me to grow as a researcher.

I would like to express my special appreciation and deep gratitude to Jatin Rath for all the times I knocked at his office door to ask questions or to discuss about science.

I would also like to thank the committee members, Prof. Tom Gregorkiewicz, Prof. Daniel Vanmaekelberg, Prof. Alfons van Blaaderen, Prof. Jaap Dijkhuis and Dr. Marcel Di Vece for letting my defense be an enjoyable moment, and for their brilliant comments and suggestions.

I want to thank Diana and Marius Nanu from Thin Film Factory for facilitating the synthesis of the quantum dots and for their precious feedback and advices. It has been very inspiring working with them.

A big thanks to Antonin Feijfer and Aleks Vetushka from Institute of Physics, Academy of Sciences of The Czech Republic for the great time I had in Prague and mainly for having shared with me their knowledge and experience, and for having allowed me to use their lab.

I thank Cecile Saguy from Technion-Israel Institute of Technology for STM/STS measurements.

My PhD would have not been the same without my group. Thanks to Minne de Jong, Diederick Spee, Jan Willem Schuttauf, Kees Landheer, Lourens van Dijk, Karine van der Werf, Caspar van Bommel, Martin Huijzer, Bart Sasbrink, Peter-Jan Dingemans, Zachar Krumer, Ionnis Poullos, Silvester Houweling and Arjen de Waal.

A special thanks to Pim Veldhuizen for his help with the Dutch summary and to Yinghuan Kuang for his endless patience.

I would like to thank Riny de Haas because she was much more than a secretary, she took care of me as a second mum. For ever I will be grateful for

this.

This experience gave me five wonderful gifts: Marites, Isabel, Akshatha, Jessica and Henriette. Their friendship made me a richer person.

Thanks to Mamma Maria, Agata, Silvia and my sweet nephew Simone for their support. No matter how many kilometers divided us, love does not know distance. Of course, a special thought to you, daddy. I know that wherever you are, you are always on my side.

There are not enough words to thank my extraordinary husband, Stefano. Thanks for being my best friend, my great supporter and for having faith in me and my intellect even when I do not have it. The last months have been hard and stressful for me and his help was priceless.

Ed infine a te, meraviglia della mia essenza, che stai dando un significato nuovo al mio corpo ed al mio essere.

Curriculum Vitae

Caterina Prastani was born on 10th of March, 1982 in Catania, Italy. In 2010 she got her master degree in Physics at Catania University with specialization on Material Science. She finalized her master thesis with the title: “*Characterization electrically active defect in bulk silicon solar cells*” during an internship at IMEC (Belgium) in the Thin Film Technology group.

In 2010 she started her PhD project in the Nanophotonics-Physics of Devices group, at Debye Institute for Nanomaterials Science at Utrecht University (The Netherlands). The PhD research was focused on the characterization of physical and chemical processes to gain know-how on incorporation sulfide quantum dots in thin film CIS solar cells.

Moreover, during PhD she supervised two bachelor students and students from Utrecht University College.

In addition to science her other passion is music. She plays piano, guitar and she studied singing.